Univerzita Karlova v Praze

Matematicko - fyzikální fakulta

DIPLOMOVÁ PRÁCE

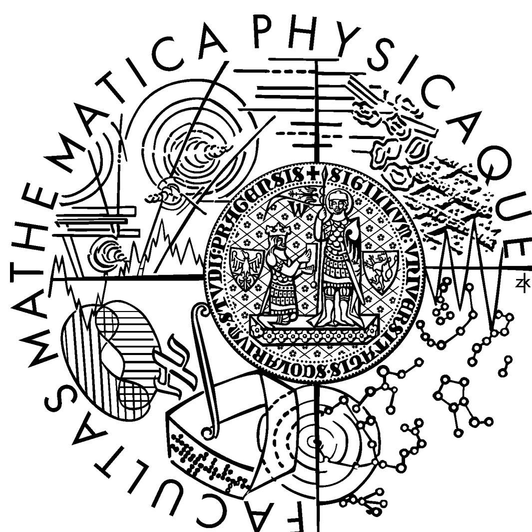

Bc. Peter Matvija

Studium interakce adsorbátu s pasivovanými povrchy Si pomocí STM

Katedra fyziky povrchů a plazmatu

Vedoucí diplomové práce: RNDr. Pavel Kocán, Ph.D.

Studijní program: Fyzika

Studijní obor: Fyzika povrchů a ionizovaných prostředí

Praha 2013

Charles University in Prague

Faculty of Mathematics and Physics

MASTER THESIS

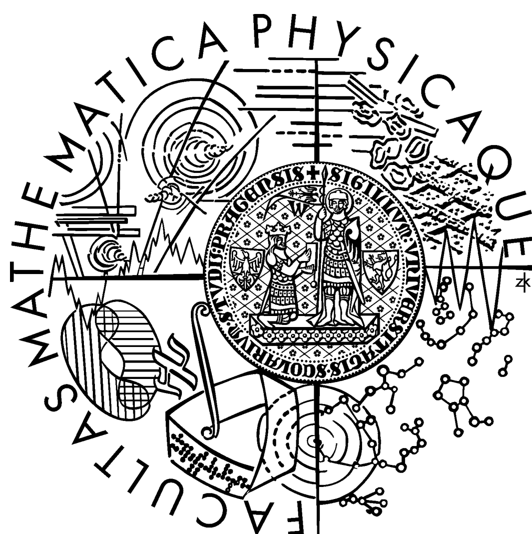

Bc. Peter Matvija

Interaction of adsorbates with passivated Si surfaces studied by STM

Department of Surface and Plasma Science

Supervisor of the master thesis: RNDr. Pavel Kocán, Ph.D.

Study programme: Physics

Specialization: Physics of Surfaces and Plasma

Prague 2013

Acknowledgements

Firstly, I would like to express my deepest gratitude to my master thesis supervisor, RNDr. Pavel Kocán, Ph.D., for his leadership, helpful advice and patience. Secondly, I would like to thank all my colleagues from the Department of Surface and Plasma Science of the Charles University in Prague and from the Institute of Physics of the Academy of Sciences of the Czech Republic for an amazing working atmosphere and many helpful insights into my work. Last but definitely not least, I would like to thank my family and friends for help and support during all my studies and work on this thesis. Special thanks go to Vladimír Macko for the help with the language correction of the thesis and to Tereza Perlácová for the moral support during the elaboration.

I declare that I carried out this master thesis independently and only with the cited sources, literature and other professional sources.

I understand that my work relates to the rights and obligations under the Act No. 121/2000 Coll., the Copyright act, as amended, in particular the fact that the Charles University in Prague has the right to conclude a license agreement on the use of this work as a school work pursuant to Section 60 paragraph 1 of the Copyright Act.

In PRAGUE; April 15, 2013 Signature of the author ________________

Název práce: Studium interakce adsorbátu s pasivovanými povrchy Si pomocí STM

Autor: Peter Matvija

Katedra / Ústav: Katedra fyziky povrchů a plazmatu

Vedoucí diplomové práce: RNDr. Pavel Kocán, Ph.D., Katedra fyziky povrchů a plazmatu

Abstrakt:
Skenovacia tunelová mikroskopia bola použitá na štúdium morfolgie táliovej vrstvy v rôznych štádiách desorbcie Tl z povrchu Si(111) a na štúdium správania sa rôznych adsorbátov na povrchu Si(111)/Tl-(1 × 1). Využitie táliovej vrstvy na pasivásiu povrchu Si(111) bolo bližšie skúmané pre rôzne druhy adsorbátov. Mangánové, hliníkové, indiové a cínové vrstvy, ktoré boli priamo deponované na Si(111)-(7 × 7), boli porovnané s vrstvami pripravenými depozíciou adsorbátu na pasivačnú vrstvu po následnej termálnej desorbcii tália z povrchu (po ohreve na teplote ≈ 400°C). Skúmané adsorbáty vykazovali známky extrémne vysokej difuzivity a slabej väzby k Si(111)/Tl-(1 × 1). Pasivačná vrstva bola voči adsorbátom stabilná. Aplikácia tália ako surfaktantu spôsobovala zníženie teploty a pokrytia potrebného na prípravu rekonštrukcií pozorovaných na povrchoch pripravených priamou depozíciou adsorbátu.

Klíčová slova: Si(111), tálium, pasivace

Title: Interaction of adsorbates with passivated Si surfaces studied by STM

Author: Peter Matvija

Department / Institute: Department of Surface and Plasma Science

Suprevisor of the master thesis: RNDr. Pavel Kocán, Ph.D., Katedra fyziky povrchů a plazmatu

Abstract:
The scanning tunneling microscopy is used to study the morphology of Tl adlayer in various stages of Tl desorption from the Si(111) surface and to study behaviour of various adsorbates on the Si(111)/Tl-(1 × 1). The utilization of thallium layer for passivation of the Si(111) was examined closely for various adsorbates. Manganese, aluminium, indium and tin layers which were directly deposited onto the Si(111)-(7 × 7) were compared with the layers prepared by deposition of adsorbate onto the passivating layer after the subsequent thermal desorption of Tl (after annealing at ≈ 400°C). Examined adsorbates exhibited signs of extremely high diffusivity and weak bond with the surface Si(111)/Tl-(1 × 1). The passivating layer was stable against the adsorbates.The application of thallium in the role of surfactant caused lowering of temperature and coverage needed for the preparation of reconstructions which were observed on the surfaces prepared by the direct deposition of adsorbate.

Keywords: Si(111), thallium, passivation

Contents

1 Scanning tunelling microscopy **8**

1.1 Scanning probe microscopy . . . 8

1.2 Principles of the STM . . . 8

1.2.1 Modes of operation of the STM . . . 11

1.3 STM limitations . . . 11

1.3.1 Thermal drift . . . 11

1.3.2 Piezo creep . . . 12

1.3.3 STM tip . . . 13

1.4 The used experimental apparatus . . . 14

1.4.1 The UHV(ultra-high vacuum) system . . . 14

1.4.2 The deposition system . . . 15

1.4.3 Measurement of temperature . . . 16

1.4.4 Automation of sample preparation . . . 17

2 Surface processes **19**

2.1 Surface morphology . . . 19

2.2 Modes of the thin films growth . . . 20

2.3 Surface kinetics . . . 22

2.3.1 Adsorption . . . 22

2.3.2 Diffusion . . . 23

3 Silicon **26**

3.1 Chemical properties and the bulk structure . . . 26

3.2 Selected surface reconstructions of silicon . . . 27

3.2.1 Si(111)-(1×1) . . . 27

3.2.2 Si(111)-$(\sqrt{3} \times \sqrt{3})$ . . . 28

3.2.3 Si(111)-(7×7) . . . 28

4 Surface passivation **31**

5 Surface Si(111) passivated by thallium **34**

6 Adsorbates on the passivated Si(111) **42**

6.1 Manganese . . . 42

6.1.1 Mn on Si(111)-(7×7) . . . 42

6.1.2 Mn on Si(111)/Tl-(1×1) . . . 45

6.1.3 Mn on Si(111) after desorption of Tl . . . 47

6.1.4 Manganese: summary . . . 50

6.2 Aluminium 52
6.2.1 Al on Si(111)-(7×7) 52
6.2.2 Al on Si(111)/Tl-(1×1) 54
6.2.3 Al on Si(111) after desorption of Tl 56
6.2.4 Aluminium: summary 57
6.3 Indium 58
6.3.1 In on Si(111)-(7×7) 58
6.3.2 In on Si(111)/Tl-(1×1) 61
6.3.3 In on Si(111) after the desorption of Tl 63
6.3.4 Indium: summary 64
6.4 Tin 65
6.4.1 Sn on Si(111)-(7×7) 65
6.4.2 Sn on Si(111)/ Tl-(1×1) 71
6.4.3 Sn on Si(111) after desorption of Tl 73
6.4.4 Tin: summary 76

7 Conclusions **77**

Introduction

Since the invention of the first transistor in the 1940's, an enormous effort has been devoted to the fabrication of new generations of semiconductor devices which are smaller, faster and cheaper than their predecessors. Soon after the invention, miniaturization came to the point when the macroscopic approach was not sufficient anymore. Production of smaller devices demanded completely new knowledge of the world, which works on a nano-scale, world completely governed by rules of quantum physics.

Device's minimization brought decrease of an overall gadget's volume and increase of its speed. On the other hand, the smaller the device, the bigger the part of volume made by the surface is. In fact, devices which structure is created in the nano-scale are created predominantly by surface atoms or layers of atoms which are affected by the surface. The surface science and new experimental approaches of the surface observation (such as STM) are therefore essential for the progress in this field of research.

Scanning probe microscopy techniques are ones of a few techniques which enable imaging of surfaces in real space. From the beginning of its usage in 1980's, they were used for imaging of semiconductor surfaces [1]. One of the first goals and successes of the STM was the resolution of the real space structure of Si(111)-(7×7). Till today, silicon surfaces are one of the most studied substrates in the surface science because they offer an exceptionally good template for 3D, 2D, 1D (Si(100)) and 0D (Si(111)) growth [2].

Epitaxial growth of flat thin films is technologically important for fabrication of many advanced materials and devices (electric micro-circuits, multi-layer devices etc.). While growth of 3D islands is common, especially in heteroepitaxy, achievement of 2D growth is, in some cases, hard to obtain [3]. A growth method called surfactant-mediated epitaxy (SME) was introduced in late 1980's to solve the problem.

In SME, layer-by-layer growth can be achieved by an application of the mediation layer. In other words, we can deposit the mediation layer of a material "A" before the deposition of material "B" on the substrate. Afterwards, the mediation layer can be removed from the surface and material "B" stay on the substrate alone. However, the surface arrangement of material "B" should be different thanks to the mediation. The exact way of the growth mediation is still not clear and therefore remains in the centre of attention.

Lately, a new possibility of mediation by the thallium passivation layer was introduced [4, 5]. An exceptional chemical inertness and a possibility of thermal removal of a thallium overlayer from the surface made it a good candidate for the usage as a surfactant. In addition to previously used surfactants, thallium in

the reconstruction (1×1) exhibits many phenomena which are extensively studied nowadays. For instance, Rashba spin splitting was reported to appear in the case of Si(111)/Tl-(1×1) [6]. After the successful managing of the surface doping, this can be a promising material for the future use in spintronic-based applications. Compatibility of these devices with the present devices based on silicon would be also of great value. The ongoing research in the field of the surfactant mediated growth and especially in the thallium mediated growth can therefore provide results in different fields of scientific interest.

Chapter 1

Scanning tunelling microscopy

1.1 Scanning probe microscopy

The scanning tunneling microscopy (STM) as a method of probing and resolving the spatial organization of electrically conductive surfaces belongs to the group of scanning probe microscopy (SPM). The atomic force microscopy (AFM), which could be used for probing nonconductive surfaces, also belongs to this group. From the historical point of view, SPM began to develop in 1982 by the invention of STM by Binning et al. [1, 7]. It makes SPM one of the youngest methods of the surface science. The idea of STM inspired development of AFM in 1986 also by Binning et al. [8]. Since then, a wide variety of SPM methods were introduced to enable probing of different kinds of surfaces, placed in different kinds of environments. Some examples are listed:

- AFM - Contact AFM, Non-contact AFM, Tapping AFM
- Magnetic force microscopy (MFM)
- Electrostatic force microscopy (EFM)

  Voltage on a cantiliever creates capacitance between the tip and single surface charges.
- STM - Scanning tunneling spectroscopy (STS), Electrochemical STM (EC-STM)
- Spin polarized scanning tunneling microscopy (SP-STM)

  If the tip is magnetized, electrons with spins matching the tip's magnetization will have the higher chance to tunnel. Essentially, it is the effect of the tunneling magnetoresistance and the tip/surface acts as a spin valve.

1.2 Principles of the STM

The STM is primarily used for an imaging of conductive surfaces in real space at an atomic scale. To do so, it uses well known quantum tunneling effect. The STM apparatus consists (as seen below on the figure 1.1) of a sharp conductive

tip, a sample, a piezomechanical system of 3D shifting and an amplifier. Depending on the type of the STM, it can also contain an ultra-high-vacuum (UHV) chamber or another type of a chamber, which maintain stable conditions during measurements. A mechanical system of damping is necessary for stabilization of the position of a sample and a sample-preparation chamber.

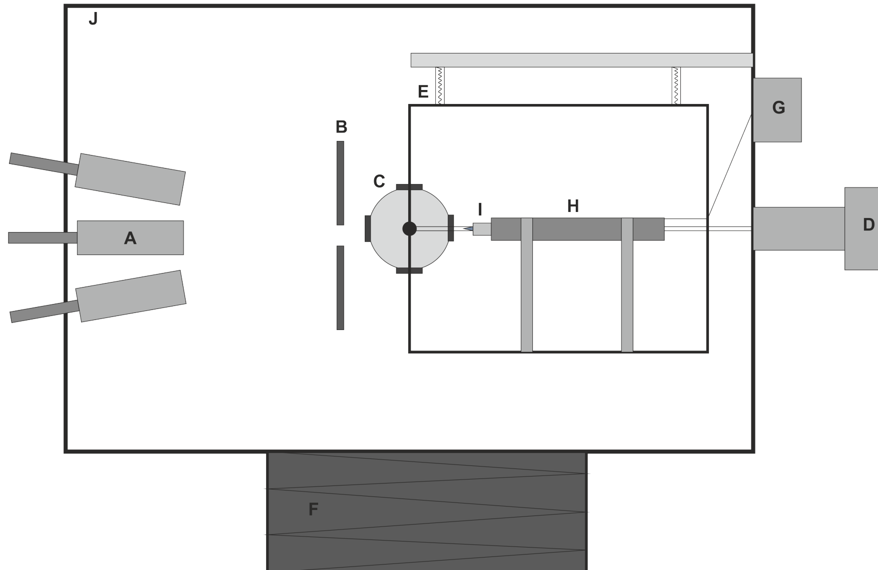

Figure 1.1: The scheme of arrangement of our STM: A) evaporation cells, B) shading plate, C) rotary carousel with samples, D) into-vacuum rotary movement transfer, E) internal cage with mechanical and magnetic dumping system, F) external system of mechanical dumping, G) electrical amplifier, H) inchworm motor, I) piezomechanical system with the STM tip, J) vacuum chamber.

In quantum mechanics, the tunneling effect is often demonstrated on the example of the quantum barrier which has rectangular shape. In our case, the barrier is the one between the sample and the sharp end of the tip (the usual distance between the sample and the tip is only a couple of angstroms). The tunneling is then enabled by an application of a bias voltage between the sample and the tip. A crucial point of the STM measurement is the exponential dependence of the tunneling current on the tip-sample distance. In the first-order perturbation theory, the current I between two electrodes can be expressed as [9]:

$$I = \frac{2\pi e}{\hbar} \sum_{\mu\nu} f(E_\mu) \left[1 - f\left(E_\nu\right)\right] \left|M_{\mu\nu}\right|^2 \delta\left(E_\mu - \left(E_\nu + eV\right)\right) \tag{1.1}$$

where $\delta(E)$ is the delta function, $f(E)$ is the Fermi function, e is the elementary charge, $\hbar$ is the reduced Planck constant, V is the applied voltage and $M_{\mu\nu}$ is the tunneling matrix element between tip states χ_μ and surface states ψ_ν. In the limit of a small voltage and temperature, 1.1 can be simplified to:

$$I = \frac{2\pi}{\hbar} e^2 V \sum_{\mu\nu} \left|M_{\mu\nu}\right|^2 \delta\left(E_\mu - E_F\right) \delta\left(E_\nu - E_F\right) \tag{1.2}$$

where E_F is the Fermi energy. The matrix element $M_{\mu\nu}$ is defined as:

$$M_{\mu\nu} = \frac{\hbar^2}{2m} \int \left(\chi_\mu^* \nabla \psi_\nu - \psi_\nu \nabla \chi_\mu^*\right) d\mathbf{S} \tag{1.3}$$

The integration is made over any surface lying entirely within the vacuum barrier region separating two systems. In the even more simplified situation, when the tip is modelled as a locally spherical potential centered at $\mathbf{r}_t$, it has been shown [10] that the current can be expressed as:

$$I \propto \sum_\nu |\psi(\mathbf{r}_t)|^2 \delta(E_\mu - E_\nu) = \rho(\mathbf{r}_t, E_F) \tag{1.4}$$

what essentially means that in this model, the tunneling current is proportional to the local density of states of the surface $\rho(\mathbf{r}_t, E_F)$ at the position of the tip.

The approximate quantum-mechanics formula for the tunneling current (1.1) shows that in real measurements, the final signal which is measured by the STM depends on both - densities of tip's and sample's states. The final image which the STM provides is therefore a convolution of the local tip's and sample's densities of states. Since the fact that states are also spatially placed, it is hard to distinguish which part of the STM signal corresponds to the spatial corrugations and which to the electronic corrugations of the surface. For this reason, DFT (density functional theory) simulations are widely incorporated as the crucial point in the process of an interpretation of imaged structures.

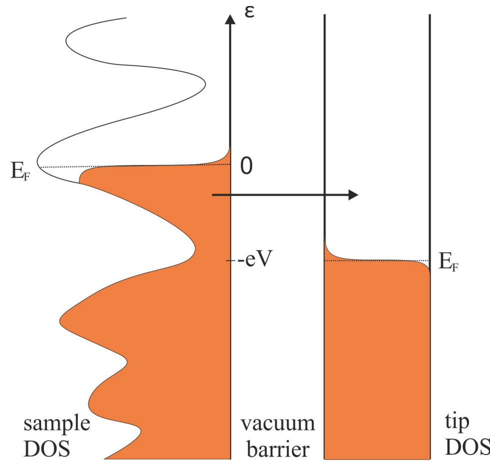

Figure 1.2: Explanatory image showing an influence of DOS at the given position of the tip on the tunneling current after applying the voltage V (after [11]).

Usually, the approximative approach based on the equation 1.4 is sufficient to explain the most important features of STM images. Real STM tips are usually made of metals (tungsten, platinum etc.). If they are not contamined, they have sufficient states with almost constant density in the proximity of the Fermi level. A constant density of the tip's states do not affect STM images as much as the non-constant and low density of states in the proximity of the Fermi level would do (e.g. for the semiconducting tip). Theoretically, the effect of the tip can be counted in also. The tip and the sample can be treated as isolated systems and their electronic structuce can be calculated separately [12]. The current for the

given tip-sample distance is determined by the matrix element (1.3) at a dividing surface S in an intermediate distance between the tip and the sample in a vacuum region [13]:

$$I = \frac{2\pi e}{\hbar} \sum_{\mu\nu} | \frac{\hbar^2}{2m} \int \left(\chi_\mu^* \nabla \psi_\nu - \psi_\nu \nabla \chi_\mu^* \right) d\mathbf{S} |^2 \delta \left(E_\mu - \left(E_\nu + eV \right) \right) \tag{1.5}$$

This equation shows that within the perturbation approach the tunneling current is basically proportional to the overlap of wave functions. Thus the tunneling current at the given tip-sample distance and the given position of the tip depends on the local densities of states (DOS) (figure 1.2).

1.2.1 Modes of operation of the STM

The tunelling current is measured and used in the feedback loop in order to adjust the position of the tip. If the feedback is set up to maintain constant tip-sample distance, we say that the STM works in the "constant height" mode. The tip is not in the constant distance to the surface in every point of measurement, but it is moving in the scanning plane that is planparallel to the sample. The topography of the surface is thus derived from the current signal. This mode enables scanning of the surface in a very high speed (couple of images in second) but it has considerable disadvantages as well. Thanks to the exponential decrease of the current, areas of the surface that are further away from the plane in which tip is moving are simply not resolved because the signal is too low in comparison with the background signal. On the other hand, if the scanning plane is too close to the surface, there is a big chance of crashing the tip.

The other mode of the scanning was elaborated to minimize these disadvantages. It is called the "mode of the constant current" and as we can see from the equation (1.5), it is also the mode of the constant tip-sample distance. As the distance is constant in every point of the scanning, the STM cannot work in such a high speed as in the other mode. The reason is the finite speed of the feedback loop, which has to adjust the tip position in every point of the scanning (usual scanning speed in this mode is one picture in a couple of minutes). Due to this, the interaction between the tip and the surface is more predictable and the crashing of the tip does not occur. In this work, the second mode of scanning was used during the measurements.

1.3 STM limitations

1.3.1 Thermal drift

Since the STM is an apparatus working in nano-scale conditions (the approximate tip-sample distance is in the order of 10^{-9} m) it demands an extreme stability of the position of the sample and the tip. A mechanical stability and a shielding against external disturbances is achieved by an external and internal mechanic and magnetic dumping (see figure 1.1-E,F), which absorbs wide range of frequencies coming from an outside of the apparatus. Nevertheless, movements with the speed in order of 10^{-9} m/s can be caused also by the thermal tensibility

of the material that the STM is made of. In experiments, most difficulties are caused by those parts of the apparatus, which are changing their temperature fast in the time, which is in the most cases the sample.

Usually, after the heating of the sample, it is necessary to wait for stabilization of the sample's temperature. A considerable amount of time (in order of tens of minutes or even hours) is usual delay after the annealing and before the next measuremnt. The other way of dealing with the thermal drift is its automatic correction governed by the software of the STM. The correction is based on the measurement of the surface shift and extrapolation of this shift into the future. The extrapolation is than counted into the movement of the tip, therefore the tip is moving along the direction of the measured drift.

1.3.2 Piezo creep

The piezo creep occurs after the setting of a new value of the voltage on the STM piezo ceramics. It exhibits as a compression and stretching of objects on the surface. Ceramics are used for a precise determination of the tip's position. If experimenter changes the voltage on the ceramics, the ceramics shrink or grow in volume. This changes the position of the tip on the surface (in case of X and Y ceramics (parallel to the surface)) or changes the tip-sample distance (in case of Z ceramic). On STM images, the creep is the most visible after a significant change of the position in X or Y direction, therefore it is also visible at the beginning of every image (right after ceramics shift the tip from the position at the end of a dislpayed area).

The creep appearance can be avoided by a simple stabilization of the ceramics motion by the scanning over the same area for longer time. The creep which occurs at the beginning of every image can be significantly reduced by the execution of the line scanning over the first line of the image for a short period of time (till the line profile stops to change rapidly) and the subsequent changing of the scanning mode from the line scanning to the image scanning.

The calibration of piezo ceramics

Piezo ceramics used for the tip movement are used for the determination of the tip's position as well. In order to read a relative position of the tip on the surface, coupling between the voltage applied to the ceramics and the position is calibrated. The output of the calibration can be seen on the STM images in the experimental part of this work as the scale bars which are present on the images. In the case of our apparatus, the calibration of Z direction (perpendicular to the surface) was not executed, therefore every time the exact vertical distance is needed, it has to be calibrated against the known surface vertical distance (the Si step height is used most commonly). Due to the fact that the vertical calibration was not pre-done, the vertical axes of line profile graphs have the arbitrary length units (the length is either calibrated on the basis of the graph or the relative lengths of objects are important). In the case of the calibration of X and Y ceramics (parallel to the surface) calibration was pre-done. Due to the piezo creep, thermal drift and other influences, calibration can change with the time and therefore it is also necessary to calibrate it directly against

known surface objects in cases which demand exact knowledge of the horizontal distance. Nevertheless, images in this work are stated with original calibration. In the cases of the recalibration used during the processing of measured data, notes which inform reader about the changed calibration are stated in the text.

As an example, we state here one case of the calibration made during the measurements (the calibration of the lateral periodicity of the defect on the figure 5.3). The calibration was possible to made thanks the known lattice constant of $((2n+1) \times (2n+1))$ objects on the surface (defects). The observed periodicity was, thanks to the creep, the thermal drift and the original mis-calibration of piezo ceramics, approximately 3.3 nm for the (11×11) HUC. This gives the value 2.1 nm for (7×7) HUC (2.7 nm was expected). We determined periodicities of $((2n+1) \times (2n+1))$ reconstructions on the surfaces with the similar creep and thermal drift. Comparison showed that the observed periodicities are in the range of (2.1 ± 0.4) nm for the reconstruction (7×7) (this gives us the coefficient of the recalibration and the value of error caused by the piezo creep and the thermal drift). The conversion coefficient was determined to be (0.76 ± 0.15).

1.3.3 STM tip

Blunt tip

Since the STM is based on the principle of the tunneling current and aspire to have an atomic resolution, the breadth of the area through which the current is tunneling is crucial. New STM tips, mostly made by chemical etching in hydroxide and subsequent annealing in vacuum, should be as sharp as possible at the beginning of their usage. Older, long used tips usually suffer from the bluntness gained by an interaction with the surface. Luckily, the exponential dependence of the tunneling current causes that it is possible to use those tips anyway.The current is going almost exclusively through the topmost atoms of the tip, which means that it is sufficient to modify only a small number of atoms on the tip to fully put the STM into the operation again. Different kinds of procedures enabling modificatiion of the tip are ordinarily used during the measurements [**?**]:

- High-voltage I-V spectra
- Z spectra (measurement of the feedback current while narrowing the tip-sample distance)
- Measurement of the autoemission of the tip
- High speed scanning

Such procedures, executed with the tip, usually end up with the modification of the tip's shape by an unpredictable transfer of the tip's atoms and are often used during the measurements.

Multiple tip

The blunter the STM tip, the lower the probability of creation of one sharp, ideally atomic, ending is. In some cases, not one, but two or more sharp endings

could be created on the tip at the same time. This results in the multiple paths for the current flowing; i.e. multiple imaging at the same time. In the real experiment, sharp endings of the tip are almost never the same height. Due to that, surface features with the height bigger than the height difference of the endings is imaged more than once (primarily by the highest ending of the tip and afterwards by the other endings). This results in the creation of the so-called ghost features on the STM images.

Contamined tip

Since the tip-sample separation during the measurement is extremely low (in order of nanometers), the interchange of matter between the tip and the sample can occur. At the beginning of the usage of the new tip, the contamination of the surface by the residual dirt (oxides, organic impurities etc.) from the tip is usually the problem. Later, the biggest issue is the contamination of the tip by the transfer of the material from the sample, since we need the tip ending to be metallic (impurities on the tip can for instace cause the broadening of a potential barrier for the tunneling, change DOS on the tip ending etc.).

1.4 The used experimental apparatus

The whole experimental part of this work was executed by the STM apparatus which is placed in the Department of Surface and Plasma Science of the Faculty of Mathematics and Physics of the Charles University in Prague. The apparatus is in-lab built. The creators of the apparatus and the operative software are doc. RNDr. Ošťádal Ivan, CSc. and doc. RNDr. Sobotík Pavel, CSc..

Defined conditions of sample's preparation and the stable defined conditions are essential for the reproducibility of all experiments. The knowledge of all parameters entering the process of preparation and measurement is the key factor affecting the right judgement and interpretation of gathered data. In order to maintain such conditions and measure its parameters the following sections of the apparatus are necessary:

1.4.1 The UHV(ultra-high vacuum) system

Ultra-high vacuum is the vacuum regime characterised by pressures lower than about 10^{-7} Pa. This pressure, inside the STM chamber, is necessary to be maintained mainly because of the necessity of an ultra clean surface. Any residual atmosphere inside the chamber would create unpredictable conditions caused by the molecules which impact onto the surface. For example, at pressure 10^{-4} Pa, it only takes 1 second to cover a surface with a contaminant. At UHV, it takes hours to contaminate the surface, which is usually enough for longer experiments. In our apparatus, the base pressure, we maintained was even lower, than UHV requires: 5.10^{-9} Pa. Thus, any possible contamination should not affect the experiments.

Vacuum was maintained by multi-level pump system which consisted of a membrane vacuum pump, a two-level turbomolecular high vacuum pump and a titan ion pump. As an additional pumping method, a titan sublimation pump

was used before each experiment. At the beginning of every working cycle of the STM, a degassing of the chamber (baking), and a degassing and an annealing of the sample is employed.

1.4.2 The deposition system

A deposition of material onto the surface was made by evaporation cells. The cells were separated from the STM part of the chamber by the shading plate, as it can be seen on the figure 1.1. The most used cell was the thallium cell, which consisted of the closed Ta tube with the small hole on the side. The tube was heated by a direct current flow. This type of heating was used as the heating method for all of the evaporation cells (the construction of each cell was different though).

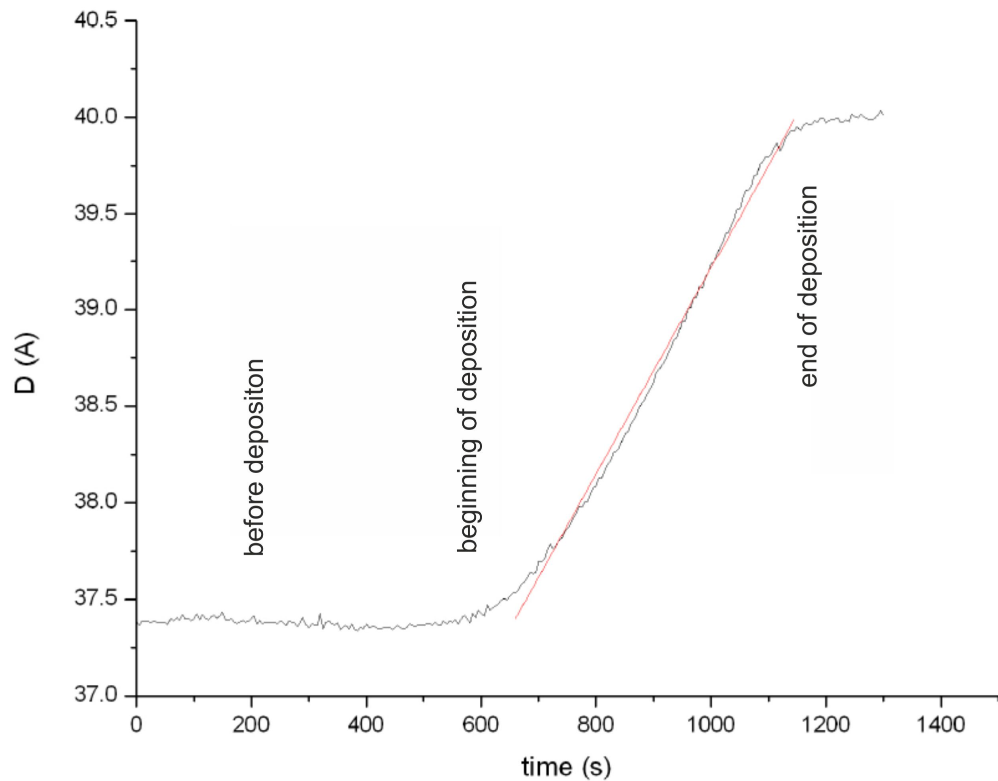

Figure 1.3: Typical record of the crystal: the deposition of one monolayer of thallium; D - the change of the crystal's thickness (in relation to the arbitrary D_0).

The amount of deposited material was determined by the method of oscillating crystal. The method is based on the measurement of the frequency shift caused by the change of mass of the quartz oscillating crystal. The relation between the frequency shift df_0 and the thickness of the oscillating quartz h is [14]:

$$\frac{df_0}{dh} = -\frac{f_0^2}{N} \tag{1.6}$$

where N is the material constant. For the quartz we used, N had the value: $N \doteq 1.67 \times 10^6$ Hz.mm.

The typical record from the crystal can be seen on the figure 1.3. The coverage of the surface (i.e. the amount of deposited material) was counted on the basis of the value which was measured by the crystal and the images of the surface obtained by the STM. An error of a determined value of the coverage was estimated after taking in account the amount of statistical data gathered by the STM and the stability of the crystal during the deposition. The error ranges from the low of 2% for the measurements with the stable crystal and sufficient amount of data to the high of 20% for the measurements with the lack of measured data and the measurements, in which the crystal could not be used (Mn, Al - crystal do not face the evaporation cells during the deposition).

1.4.3 Measurement of temperature

The sample's temperature was not measured directly during the experiment. Heating of the sample was executed by the direct current flow. Since the temperature and the value of input electrical power are proportional to each other, temperature was determined afterwards, thanks to the calibration. Examples of the temperature calibrations for the different samples can be seen on the figure 1.4. In pursuance of the calibration and the measurements of the STM, we estimated the error of the determination of temperature as 5% (the error is not placed in the text and is replaced by the symbol "≈" hereafter).

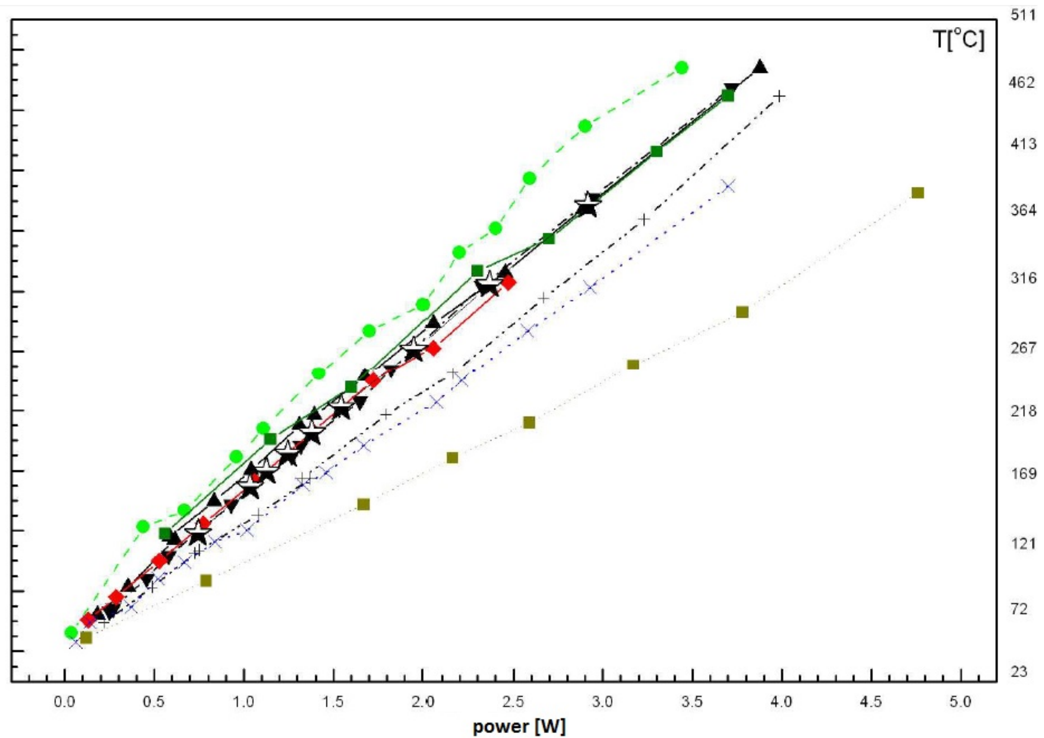

Figure 1.4: Temperature calibration of different samples [15].

1.4.4 Automation of sample preparation

As a part of our work, changes of the STM annealing and data acquisition system were executed. Until the time of this work, preparation of the samples was done manually. Preparation conditions were measured by multimeters. Exact archiving of measured data was not possible same as the automatic control of preparation based on the computer regulated feedback. Therefore, we reacted on the necessity of the automation by the creation of the data acquisition and regulation system which scheme can be seen on the figure 1.5. The system consists of two multimeters intended to measure current and voltage, the ionization gauge and the power supply. It can be connected either to the sample for the control of annealing, degassing etc. or can be used as the regulation of deposition rate if connected to an evaporation cell.

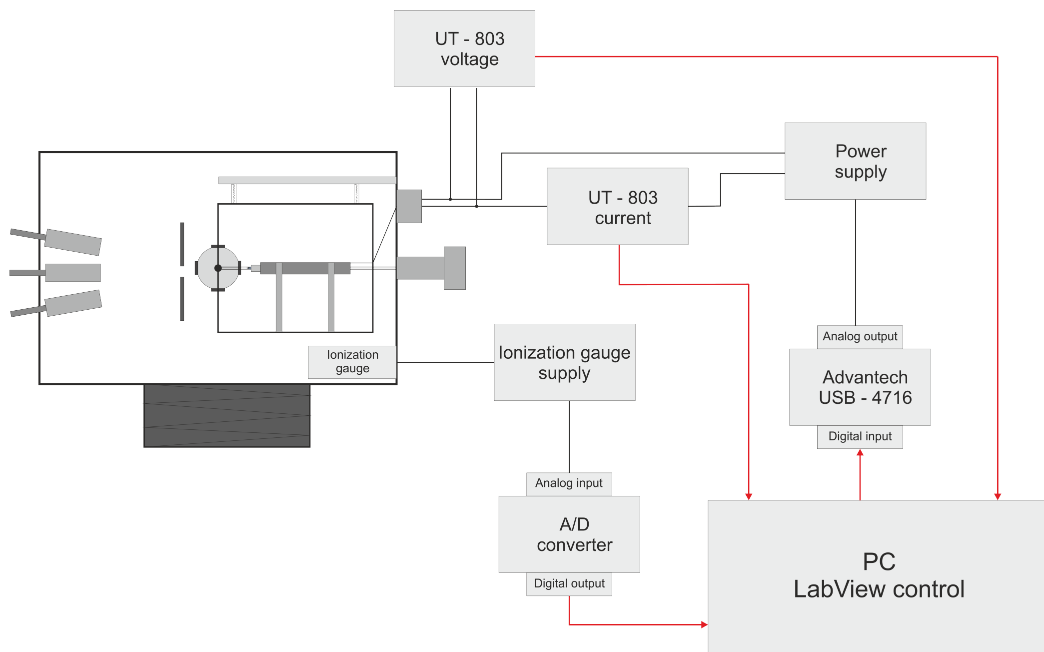

Figure 1.5: The data acquisition and regulation system of sample preparation and deposition.

Electric multimeters are directly connected to a computer by USB ports. Since an input of the power supply unit is the analog value of current, digital-analog convertor was used as an intermediate stage of the regulation. Whole system is governed by the LabView environment program. The front panel of the program can be seen on the figure 1.6.

Two parts of the window can be distinguished. The upper part serves for displaying of the recent values of voltage, current, power (at the sample or evaporation cell) and pressure (in the apparatus). The measured data can be saved in the text file. The automatic high pressure protection can be set as well. The protection shuts down the current generated by the power supply, if the set value of the pressure is reached (this option enables automatic degassing and annealing of the sample). The bottom part of the window serves for the regulation of output current of the power supply. The preset possibility of flashing the sample by an electrical pulse and possibility of the slow ramping down (slow linear

decrease of output power) is also built-in. The program was utilized during the measurements of this work and facilitated substantially easier and more exact sample preparation.

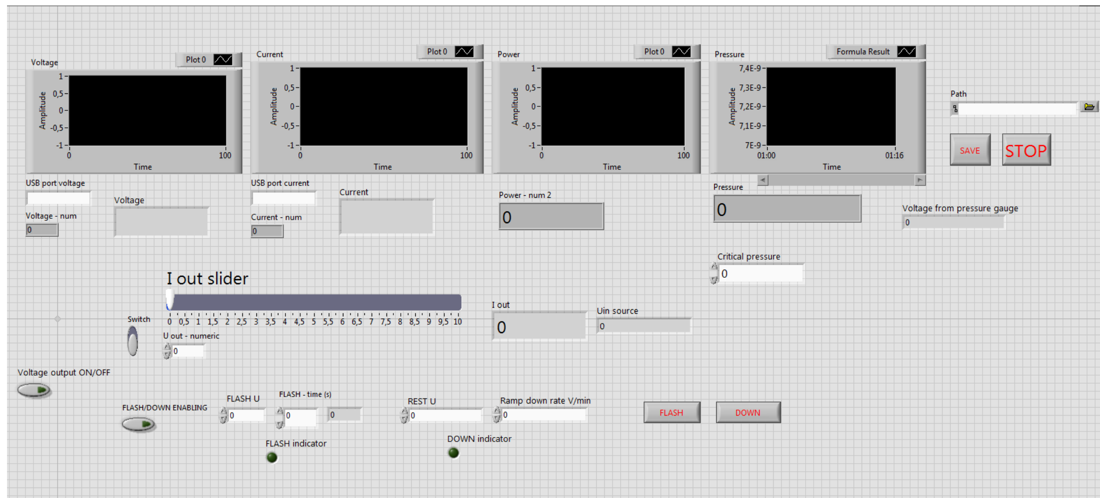

Figure 1.6: The front panel of the LabView program.

Chapter 2

Surface processes

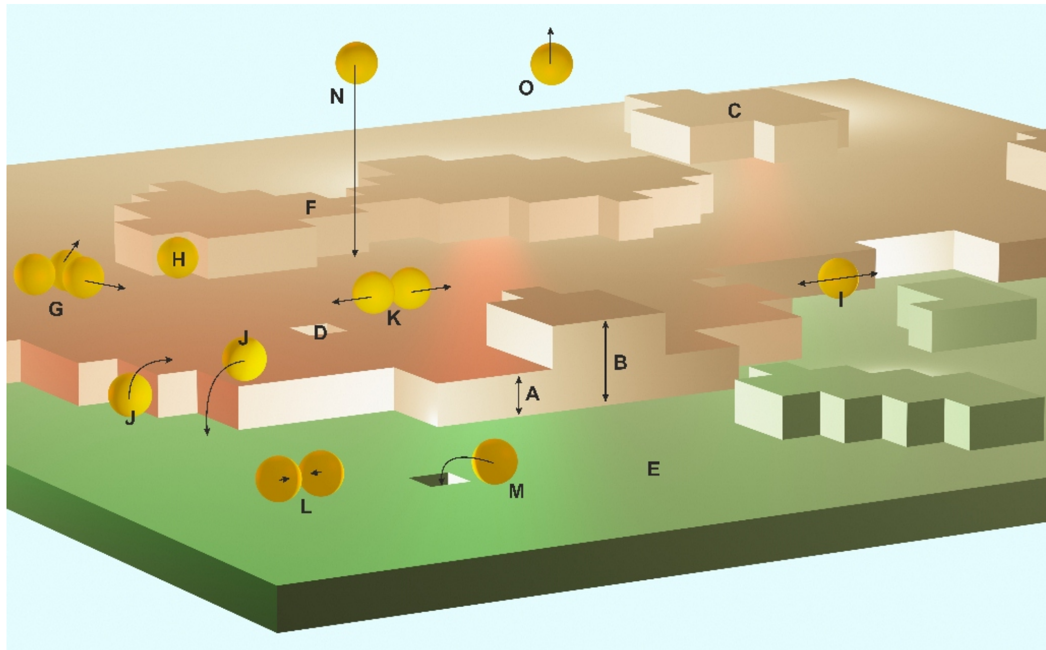

Figure 2.1: Surface morphology and surface processes: A) step edge B) double step edge C) island D) vacancy E) terrace F) coalescence of islands G) island decay H) attachment to an island at kink position I) step edge diffusion (at ledge position) J) up and down step edge crossing K) dimer decay L) island nucleation M) atom filling vacancy N) arrival of deposited atoms O) desorption

2.1 Surface morphology

As can be seen on the figure 2.1, different morphological objects on the surface can be distinguished during the growth of thin films. Ideally, if the surface is cut along one of the low-indices planes (according to the Miller notation of crystal directions and crystal planes) it should consist only of one big terrace. In the reality, terraces are interrupted by step edges, whose density on the surface depends on the accuracy of the preparation of the surface. In other words, it depends on

the fact, how accurate to the low-index plane we can cut our sample. Steps are usually long and linear, but they can also create circular objects: islands. During the growth of the thin film, we can observe the growth of new layers which in most cases is not concentrated evenly on the surface. From the morphological point of view, the local growth speed depends on forces which affect the atom during his diffusion on the surface. The fastest nucleation thus occurs at the places with the biggest attractive adatom-surface force (places with the minimal potential enegy correspond to the biggest attractive force). Based on this fact, surface positions with the significant difference of the attractive force can be distinguished:

- Kink position - the position on the lower side of a step edge with two close neighbor atoms from the side and one from the below (figure 2.1(H))
- Ledge position - the position on the lower side of a step edge with one close neighbor atom from the side and one from the below (figure 2.1(I))
- On terrace position - the position on a terrace with no neighbor atoms from the side (figure 2.1(E))
- Vacancy - the position in a terrace in case of the missing atom (4 neighbors from side, 1 neighbor from below) (figure 2.1(D))

The number of neighbouring atoms is relative to the magnitude of the attractive force. Because of that, we can see cases when the growth is concentrated almost exclusively at the kink sites. An example of the growth, which is localized specifically at one site of the surface is for instance the step-flow mode of growth, which can be observed for example on the surface Si(001) [16].

2.2 Modes of the thin films growth

If we look at the surface growth globally, from the thermodynamic point of view, three qualitatively different equilibrium modes of thin film growth are distinguishable [17]:

- 2D (Frank - van der Merwe) - layer after layer growth: Attractive force between the surface and deposited atoms is stronger than between deposited atoms themselves. Deposited material first creates a complete monolayer on the substrate. After the completion of the first monolayer, the next monolayer is build with a weaker bonding. Layers are created one after another until the bulk arrangement of deposited material is reached. Growth phases in this mode are:
  - Island nucleation
  - 2D island growth
  - Island interconnection and monolayer completion
  - Repetition of points 1 - 3

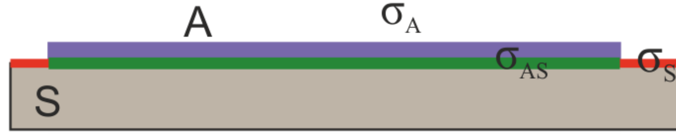

Figure 2.2: Energy balance of surface growth in 2D mode: S - substrate, A - adsorbate, σ_S - density of free surface energy of substrate, σ_A - density of free surface energy of adsorbate, σ_{AS} - density of free energy of interface between substrate and adsorbate

Since every system tends to reach its energetical minimum, it is necesarry to fulfill following condition for 2D growth (figure 2.2) to take a place :

$$\sigma_A + \sigma_{AB} \leq \sigma_S \tag{2.1}$$

- 3D (Volmer - Weber) island mode: Atoms of deposited material are bonded more strongly to each other than to substrate atoms, therefore they prefer to create 3D clusters. Growth of higher layers is possible before completion of the lower layers and the film grows according the following phases of growth:
  - Island nucleation
  - 3D island growth (growth on the top of an incomplete monolayer)
  - Coalescence into bigger islands
  - Secondary nucleation on the top of coalesced islands
  - Completion of a semi-continuous thin film

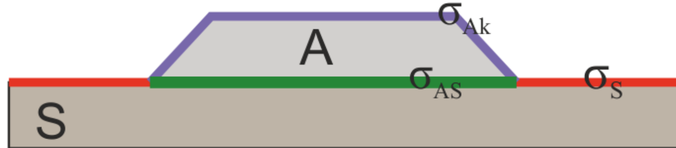

Figure 2.3: Energy balance of the surface growth in the 2D mode: S - substrate, A - adsorbate σ_S - density of the substrate's free surface energy, σ_{Ak} - surface density of the free energy of the kth type of the adsorbate's surface plane, σ_{AS} - density of the free energy of the interface between a substrate and an adsorbate.

Energy balance condition for 3D type of growth (figure 2.3) is:

$$\sum_k S_{Ak}\sigma_{Ak} + \sigma_{AB}X_{AB} > \sigma_B X_{AB} \tag{2.2}$$

where X_{Ak} is the area of adsorbate's crystalline planes of the kth type and X_{AB} is the area of an interface between a substrate and an adsorbate.

- 2D/3D (Stranski - Krastanov) mode: At the beginning, one complete layer of deposited material is created. Thanks to different lattice constants of a

substrate and an adsorbate, the strain between layers occurs. This represents an addition to the surface free energy and after a deposition of the next layers, it results in the changing of the growth mode into the 2D mode.

All modes mentioned above are equilibrium modes, which means that in some cases, system needs the significant amount of time to get to his equilibrium even when all energetic conditions are fullfilled.

2.3 Surface kinetics

If we look closer at individual behaviour of each deposited single atom, we can divide its role in the surface growth (from a point of view of surface kinetics) into these three parts:

- Adsorption
- Diffusion
- Desorption

The diffusion and desorption are thermally activated processes. It means that the frequency of occurrence of a particular process follows the equation:

$$\nu_p = \nu_0 \exp\left(-\frac{E_p}{kT}\right) \tag{2.3}$$

where ν_0 is the frequency prefactor, k is Boltzmann constant, T is absolute temperature and E_p is an activation energy of a particular process. In the case of desorption, an activation energy is the energy which a particle needs to get out of a potential dip. The dip is created by attractive forces of surface atoms. The diffusion activation energy mirrors the strength of a particular potential barrier created by an inhomogenous local distribution of surface forces.

2.3.1 Adsorption

The key factor in the theoretical description of any surface process is the potential energy surface (PES) of the system. It corresponds to the energy hyperplane over the configuration space of the atomic coordinates of the involved atoms [9]. The information about adsorption sites and energies, reaction paths, barriers for adsorption, desorption and diffusion can be directly acquired from the PES. A long used method of describing surface adsorption is characterization by one-dimensional potential curves. One of the oldest and most widely used potential was proposed by John Lennard-Jones in 1924 [18]:

$$V_{LJ} = \varepsilon \left[\left(\frac{r_m}{r}\right)^{12} - 2\left(\frac{r_m}{r}\right)^{6} \right] \tag{2.4}$$

where ε is the depth of the potential well, r is the distance between the particle and the surface, and r_m is the distance at which the potential reaches its minimum. An example of Lennard-Jones potential diagrams for molecular and

dissociated molecule of O_3 can be seen on the figure 2.4. It is apparent, that the potential is created by two parts: attractive and repulsive. Attractive interaction corresponds to the Van der Waals forces while the repulsive component is the result of Pauli repulsion at short ranges due to the overlapping of electron orbitals.

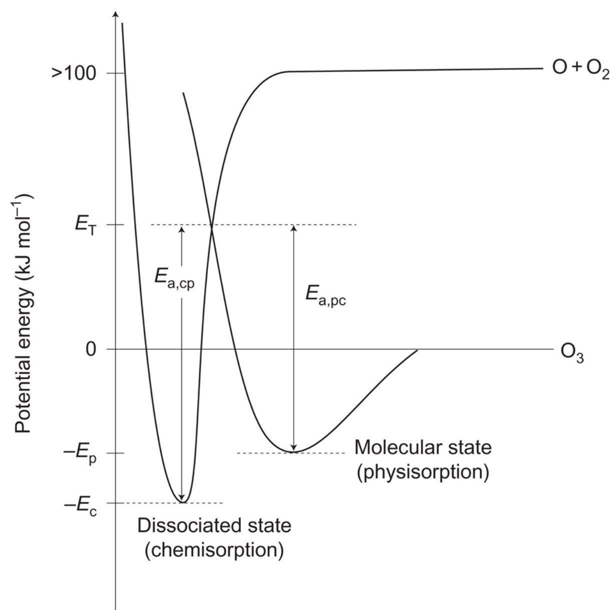

Figure 2.4: An example of Lennard-Jones potential energy diagram for the adsorption of molecular and dissociated O_3 [19]; E_p: energetic minimum of physisorbed molecule, E_c: energetic minimum of the system after the chemisorptions, E_T: transitional energy between chemisorbed and physisorbed state, E_a: activation energies; the horizontal line represents the distance of the molecule from the surface.

Types of adsorption

The figure 2.4 shows that two types of bonding between a particle and a surface exist: physisorption and chemisorptions. They are generally distinguished by the binding energy, which lays in the range of $10 - 100$ meV for physisorption and $1 - 10$ eV for chemisorption. The high binding energy of a chemisorbed particle is caused by the change in its electronic states (true chemical bond is created). Similarly to the case of adsorption of ozone (firuge 2.4), many particle exhibit the chemisorption which involves an activation energy, while the physisorption is generally direct, without any necessary activation energy.

2.3.2 Diffusion

Diffusion is a process which can be described as a lateral jumping along the surface from one stable adsorption site to the next one. It is is a typical process that is driven by thermal fluctuations. Each adsorbate performs thermal vibrations around the equilibrium site in the adsorption well. The rate for a

jump to a next nearest neighbour site k_d is given by the Arrhenius expression 2.3. Generally, the diffusion can be theoretically described by two possible ways. Microscopically, from a one-particle point of view, we can describe diffusion as a sequence of discrete jumps from one site to another. In this case, the probability $P(\mathbf{R}, t)$ that the lattice site $\mathbf{R}$ on the surface is occupied at time t is introduced. If we also consider the special case of a square lattice with the lattice constant a, we can obtain the well-known diffusion equation [9]:

$$\frac{\partial P(\mathbf{R}, t)}{\partial t} = \frac{k_d a^2}{4} \nabla^2 P(\mathbf{R}, t) \tag{2.5}$$

The factor

$$D_s = \frac{k_d a^2}{4} \tag{2.6}$$

is called the self-diffusion coefficient and is typical for each surface-adsorbate combination. The other approach to the problem can be many-particle. We can describe the diffusion as the transport of a large number of atoms due to a gradient in the particle density. Fick's first (2.7) and second (2.8) law of diffusion are valid in this case:

$$\mathbf{j} = -D_c \nabla n(\mathbf{R}, t) \tag{2.7}$$

$$\frac{\partial n(\mathbf{R}, t)}{\partial t} = \nabla \cdot (D_c \nabla n(\mathbf{R}, t)) \tag{2.8}$$

where $\mathbf{j}(\mathbf{R}, t)$ is the particle current.

Since surface kinetics governs the behaviour of each individual atom on a surface, clearly, there has to be a connection between physical quantities describing kinetic processes on the surface and the morphology of the surface. The most apparent is probably the connection between the size of islands and the diffusivity of adsorbate (i.e. diffusion coefficient of adsorbate). Derivation of the relation is based on the idea of an existence of a critical cluster size [9]. Let us assume that the cluster of size i is the biggest unstable cluster (i.e. clusters with the size $j \geq i$ are stable and grow faster than decay). For the simplicity, we consider that only single atoms are mobile, and can attach and detach from clusters. If we introduce the density of islands of the size j as n_j, the density of stable islands n_x will be given as follows:

$$n_x = \sum_{j=i+1}^{\infty} n_j \tag{2.9}$$

By considering all possible processes, we can derive the rate equations for the densities n_j. For instance, the single atoms rate equation is [9]:

$$\frac{dn_1}{dt} = F - \sigma_i D n_i n_1 - \sigma_x D n_x n_1 F\theta \tag{2.10}$$

where F is the flux of deposited particles, $sigma_i$ are capture numbers (describe the average geometry of islands), D is diffusion coefficient and θ is the coverage of the surface. A decrease in number of single atoms can be accounted to the attachment to unstable and stable clusters (the second and the third term of the equation (2.10)). An increase in the number of single atoms due to the flux F is reduced by the factor $(1 - \theta)$, which accounts a direct attachment of deposited particle to a cluster. If we assume that objects on the surface are in the local

thermodynamic equilibrium and consider the coalescence too, we can get the final rate equations, which, after solving, give the relation between the island density n_x, the diffusion coefficient D and the flux F [9]:

$$n_x \propto \left(\frac{D}{F}\right)^{-\frac{i}{i+2}} \tag{2.11}$$

The higher the diffusivity of an adsorbate is, the bigger islands on the surface should be observed.

Chapter 3

Silicon

3.1 Chemical properties and the bulk structure

Silicon is the second most abundant element in Earth's crust (it makes 25.7% of its weight) known since 1787, when it was first identified by Lavoisier [20]. It is the element with the proton number 14 and three stable isotopes: $^{27}_{14}$Si, $^{28}_{14}$Si and $^{29}_{14}$Si with natural occurrence 92%, 5% and 3% respectively. One radioactive isotope with the negligible occurrence ($^{32}_{14}$Si) also exists. In the periodic table, it is placed in the third period and the fourth group. Its full electron configuration is $1s^2 2s^2 2p^6 3s^2 3p^2$ (or [^{10}Ne] $3s^2 3p^2$). After sp2 orbital hybridization it has valence 4 which makes it very similar to carbon in the versatility of usage.

Silicon occurs in a wide variety of compounds: silicides, silanes, oxides... In a clear form, it crystallizes in a cubic face centered system - the crystalline structure of diamond (figure 3.1). In the bulk, every silicon atom creates 4 covalent bonds which fulfill its valence.

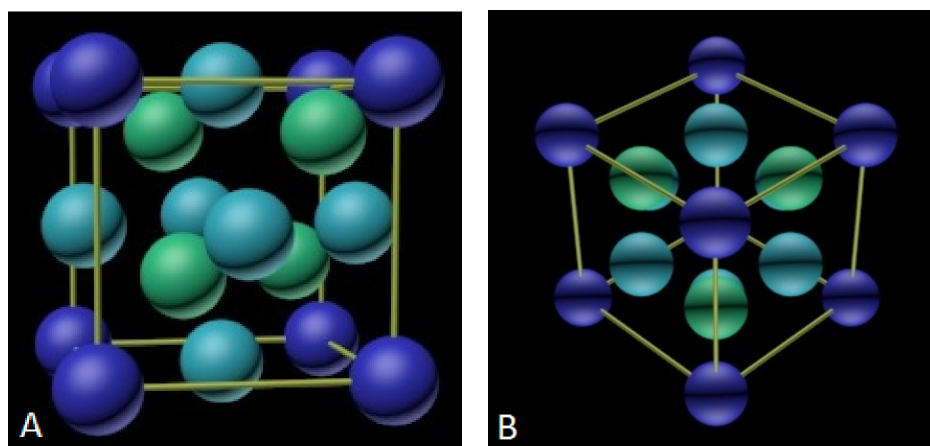

Figure 3.1: Structural model of silicon: A) bulk structure, B) view of the plane (111). All spheres represent silicon atoms (colors are used only to distinguish one atom from another).

3.2 Selected surface reconstructions of silicon

As every other real crystalline material which exists in a finite volume, a real silicon crystal has to have a termination - a surface. Depending on a direction of the normal of the surface in relation to the crystal lattice, we distinguish different surface planes with different physical properties. The termination of the crystal induces an existance of atoms with one or more broken bonds; i.e. surface atoms with so-called dangling bonds. The density of dangling bonds of a surface determines the surface reactivity. Since every physical system tends to get to the state with the minimal energy and atoms with broken bonds represent bigger contribution to the free surface energy than bonded atoms, we can observe the creation of surface reconstructions (reorderings of top layers of a surface atoms in order to minimize number of unsaturated bonds). Generally, one surface can have a wide variety of surface reconstructions. This is a consequence of the necessity of an additional energy, which is used for the change of the arrangement of atoms on the surface. Experimentally, it means that in order to achieve the most stable surface reconstruction, it is necessary to provide a sufficient ammount of energy to the surface atoms, usually by heating the surface. Only after the heating and the slow cooling of the surface, the most stable reconstructions on particular surfaces can be observed (atoms have the sufficient energy to free from their original sites and have the sufficient time to find the energetically most favorable position on the surface).

In this work, we focus our attention on the Si(111) surface. This surface plane has triangular symmetry with the most stable reconstruction (7×7). The most common metastable ones are (5×5), (9×9), (2×2), $c(2 \times 4)$, $c(2 \times 8)$.

3.2.1 Si(111)-(1×1)

The primary reconstruction occurring on the surface Si(111), after deposition of monovalent adatoms, is the reconstruction (1×1). For instance, the surface passivated by one monolayer of hydrogen or thallium acquires this arrangement [21, 22] due to the fact that each surface dangling bond is saturated by one adatom on average. Therefore, adatoms reproduce an ordering of underlying layer (which is automatically (1×1), since the last layer of bulk-arranged silicon is a reference layer used to determine reconstruction of other overlaying layers). Aside from ordering, the reconstruction (1×1) is also used as a reference of amount of deposited material. The customary used unit is called "monolayer", which in the case of Si(111) represents: $1\ \mathrm{ML} = 7.83 \times 10^{14}\ \mathrm{cm}^{-2}$. On the clean Si(111) surface (without a presence of adsorbates), the (1×1) reconstruction is extremely unstable. The only experimental evidence of the ("1×1") reconstruction on the clean Si(111) comes from RHEED and LEED experiments which show the (1×1) pattern at high temperature [23]. Nevertheless, the pattern does not originate in the stable surface arrangement, but it is caused by thermal movements of silicon atoms on the surface. For the structural model of the (1×1) reconstruction of thallium on the Si(111) surface see the figure 3.2-(a).

3.2.2 Si(111)-($\sqrt{3} \times \sqrt{3}$)

Various "root-three" structures arise primarily in connection with metals and semi-metals (Ag, Au, Pb, Sb etc. [17]) on the (111) face of semiconductors. In the case of Si(111), pure reconstructions consisting exclusively of one type of adatoms were observed (Al [24, 25], In [24, 26], Sn [27] etc.) side by side so-called "mosaic" root-three reconstructions (Tl [14, 28], B, Al, Ga, In [29] etc.) where the part of adatoms are substituted by silicon.

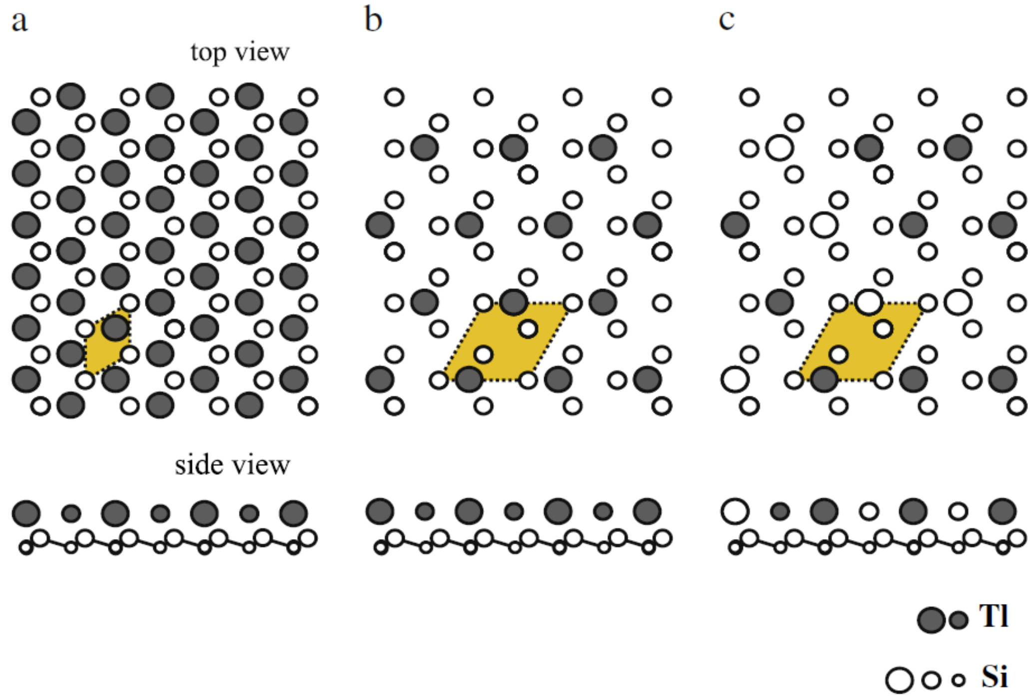

Figure 3.2: [28] Schematic structural models of the Si(111) surface with (a) Tl-(1×1), (b) Tl-($\sqrt{3} \times \sqrt{3}$), (c) mosaic Tl-($\sqrt{3} \times \sqrt{3}$) reconstructions. Filled and empty circles represent Tl and Si atoms. Unit cells of (1×1) and ($\sqrt{3} \times \sqrt{3}$) are outlined by the rhombuses.

An example of the structural model of Tl-($\sqrt{3} \times \sqrt{3}$) reconstruction in the "clean" and the mosaic form is present on the figure 3.2-(b) and 3.2-(c). Ozkaya et al. in their density functional based theoretical studies [30] compared two possible models of Tl-($\sqrt{3} \times \sqrt{3}$) reconstruction with Tl in 3-fold symmetric hollow sites (H_3) and in 4-fold atop sites (T_4). The energy difference between the two model is indeed very small within the energy of 0.03 eV in favour of the T_4 model. The same T_4 sites are occupied by Tl atoms in the case of the reconstruction Si(111)/Tl-(1×1) (figure 3.2-(a)).

3.2.3 Si(111)-(7×7)

Si(111)-(7×7) is energetically the most convenient and the most stable reconstruction from all of reconstructions on the Si(111) surface [2]. It is one of the most complex observed reconstructions and thanks to its complexity it also needs the highest temperature of the preparation from all Si(111) reconstructions. His-

torically, it took more than 25 years to completely resolve the structure of (7×7) ([1, 31]). Nowadays, it is still one of the most studied surfaces.

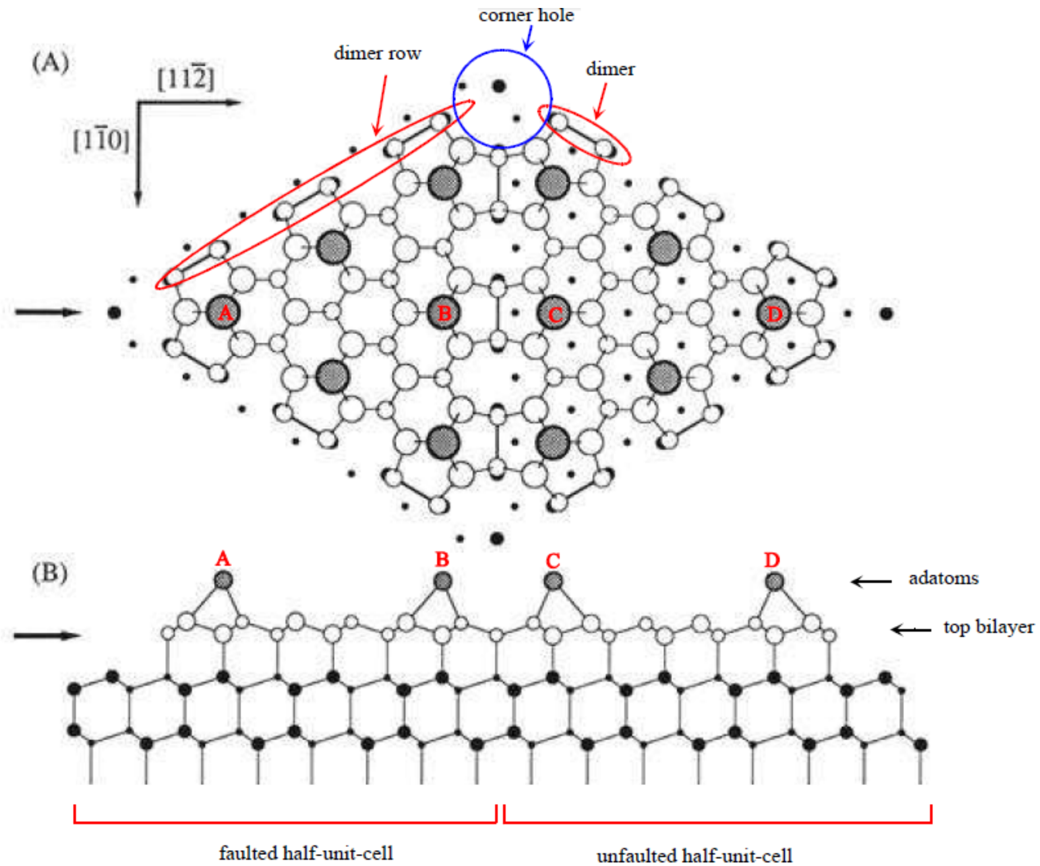

Figure 3.3: Scheme of (7×7) reconstruction: (A) top view, (B) side view [32].

In comparison with other reconstructions of Si(111), the (7×7) is outstanding by the fact that it affects atoms in deeper parts of the bulk (see figure 3.3). The base of the reconstruction is formed by alignments of pairs of adjacent silicon atoms that form covalent bond. Since the surface has the triangular symmetry, there are 3 possible orientations of these dimer rows (60° angle between every two rows). The periodicity of the surface is determined by periodicity of dimer row's crossings, which in case of (7×7) reconstruction is every third dimer (approximately every 2.7 nm [2]). If crossings occurs every second or fourth dimer, we observe (5×5) and (9×9) reconstructions respectively. Generally, we can say that there exist whole group of reconstructions with periodicity $((2n+1) \times (2n+1))$. After dimer rows creation, the surface is divided into triangular areas half unit cells (HUC). Since every individual dimer is created on one side of the hexagonal cell (dissymmetrically) and dimer rows are boundaries between each adjacent HUCs, adjacent HUC does not have the same structure in relation to the bulk. Due to this, we distinguish 2 types of HUCs - unfaulted (UHUC) and faulted (FHUC). The first ones keep bulk structure and the second ones are shifted compared to the bulk, as we can see from the top view on the figure 3.3.

The above mentioned high stability of the surface rises indeed from the low density of dangling bonds. In comparison with recostructions (1×1) with silicon termination with 1 dangling bond for (1×1) cell and reconstruction $(\sqrt{3} \times \sqrt{3})$ with 1/3 of dangling bond for (1×1) cell on average, (7×7) reconstruction has 19

unsaturated bonds for its elementary cell (0.39 of dangling bond on (1×1) area on average), which are divided into three layers of silicon. The deepest unsaturated bond is placed in the last layer of silicon without the stacking fault and lays in the middle of every corner hole. The layer with stacking fault contains 3 unsaturated bonds for every HUC. Atoms which hold these bonds are called "rest atoms" and are placed in the upper of two layers of the billayer. The last layer of silicon atoms consists of adatoms that saturate 3 bonds of underlying atoms. Since silicon is 4-valent, each adatom adds one unsaturated bond (9 dangling bonds for one HUC overall).

Chapter 4

Surface passivation

A growth method, called surfactant-mediated epitaxy (SME), was introduced in late 1980's [3, 33]. Till today, it is one of the most used methods, which enables the growth mode modification of an adsorbate on the given substrate.

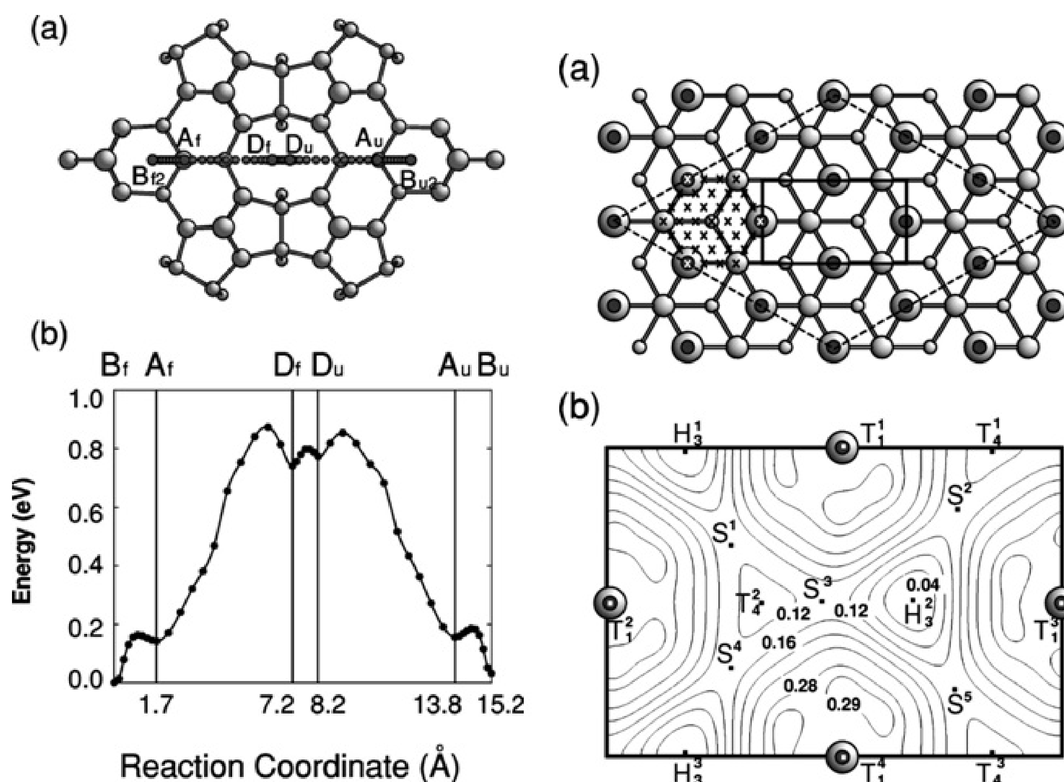

Figure 4.1: [21] An example of unpassivated and passivated surface: left: Si(111) with the reaction coordinate over the boundary of HUC; right: Si(111)/H with PES of the surface.

Passivation is the process in which a surface is covered by a suitable medium, which saturates dangling bonds and therefore lowers the reactivity of the surface. The process is used especially for the passivation of highly reactive surfaces such as surfaces of semiconductors (for instance Si(111)). Aside the lowering of the

reactivity, the passivation has also strong influence at the potential energy surface (PES), which is usually much smoother than the original surface. Figure shows the example of a first-principle study of a non-passivated surface Si(111) and the same surface passivated by 1 ML of hydrogen [21]. The left image shows the reaction coordinate of Ag atom over the boundary of two HUCs, between two dimers of the boundary. The coordinate is the easiest way of diffusion between two HUCs. The computed value of energy barrier is 0.88 eV what is approximately 4 times bigger than for the diffusion inside the HUC. The usual case of the diffusion on this surface therefore looks like this: the diffusing atom hops multiple times through different adsorption sites inside the HUC and make multiple attempts of overcoming the energy barrier between HUCs before jumping to the neighbouring cell. Movement inside the cell is therefore very fast, even for imaging of the STM (if only one Ag atom is present inside the cell, the STM observes the fuzzy image of the cell, which is in fact the averaging of Ag positions inside the cell [34]). On the right of the figure 4.1 the PES of Si(111)/H is shown for comparison. Interestingly, the biggest potential corrugation on the surface is in this case only 0.12 eV. This value is even lower than the diffusion barriers inside the HUC of the (7×7), which means that the adsorbate on the surface diffuses almost freely.

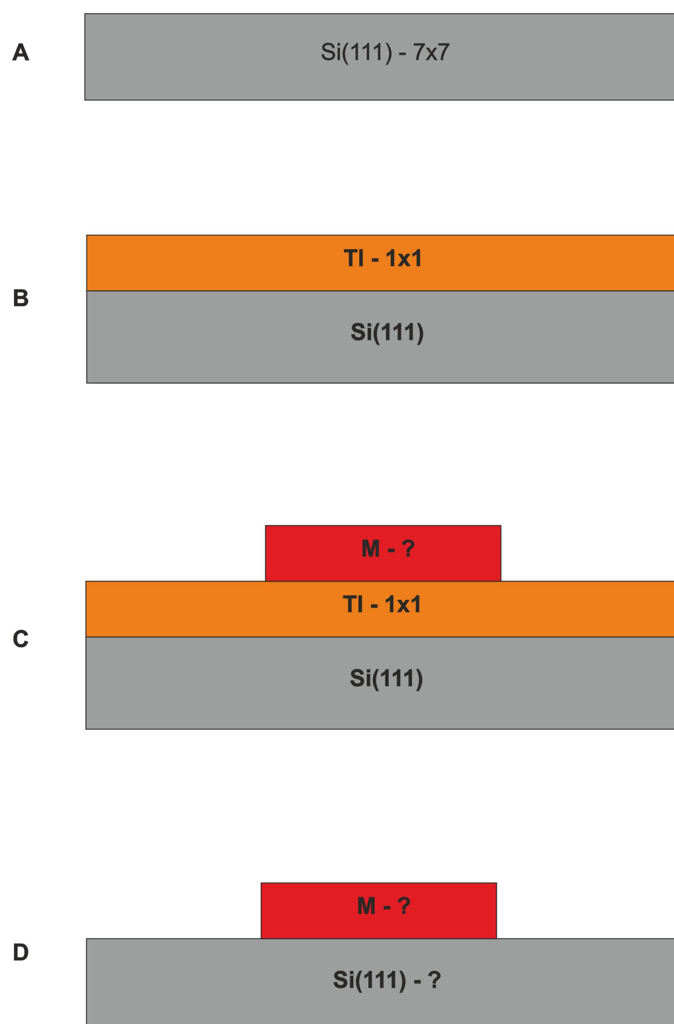

Figure 4.2: Schematic image of the passivation process with thallium in the role of surfactant.

The passivation is only the first step in the SME. As it is shown on the figure 4.2, for a passivant to become a surfactant, it is necessary to remove the passivation medium from the surface. Thus, the passivant has to have suitable properties which enables its removal from the surface (lower desorption temperature then the overlayer deposited on the passivated surface, low solubility in the substrate, etc.). As a result of SME, the change of mode of growth during the epitaxy can be expected (for instance, many SME systems have been reported to suppress 3D island growth [33, 35]).

In the following experimental part of the work, two basic types of the surface preparations are used. The first is the preparation of the Tl-(1×1) layer on the top of Si(111). Annealing at ≈ 300°C for 2 minutes is used for this purpose (2 minutes annealings at different temperatures are used during the desorption experiments described in the following chapter). Preparation of thallium mediated layers is achieved by annealing of Si(111)/Tl layer at ≈ 300°C (preparation of the Tl-(1×1) layer), subsequent deposition of the adsorbate and annealing at ≈ 400°C for 5 minutes (removal of Tl). These layers are compared with the layers prepared by direct deposition of the adsorbate onto the Si(111)-(7×7) and subsequent annealing at ≈ 400°C for 5 minutes.

Chapter 5

Surface Si(111) passivated by thallium

Morphologically, the clean surface Si(111)/Tl-(1×1) (figure 5.1-left, for the structural model see the figure 3.2) has two dominant features, which are not directly expectable from the appearance of the surface before the Tl deposition. The first feature is an emergence of flat islands on the smooth surface covered by one monolayer of thallium in the reconstruction (1×1). The coverage of islands is too high ($\approx 5\%$) to explain it as the second layer of thallium. Moreover, the line profile taken over the island step and the step edge between two terraces (figure 5.1-right) shows that the height of both steps is same. That suggests the same nature of islands and terraces. The explanation of this unexpected emergence of islands (already published in [28]) lays in the surface density of the top bilayer of reconstructions (7×7) and (1×1), which is higher in the case of the (7×7). After the coverage of the surface by thallium, underlying silicon tends to change its arrangement from (7×7) to (1×1). The transformation produces excess

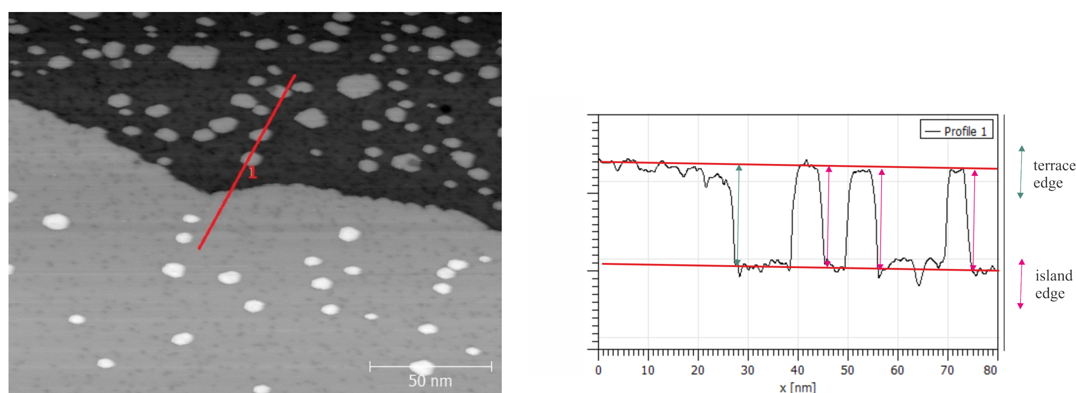

Figure 5.1: Si(111)/Tl-(1×1) (left) with the line profile over the step edges of a terrace and islands (right). The length units on the vertical axis of the graph is arbitrary.

silicon, which is excluded into the next layer and creates the mentioned islands. The counted coverage by islands is $(4 \pm 1)\%$, which is, within an error range, in

agreement with experimental data ($\approx 5\%$).

The second interesting features of the Tl-(1×1) surface are its occasionally observed triangularly shaped defects with the inverse contrast at opposite tip biases, as it is seen on the figure 5.2. Two images of the figure were taken

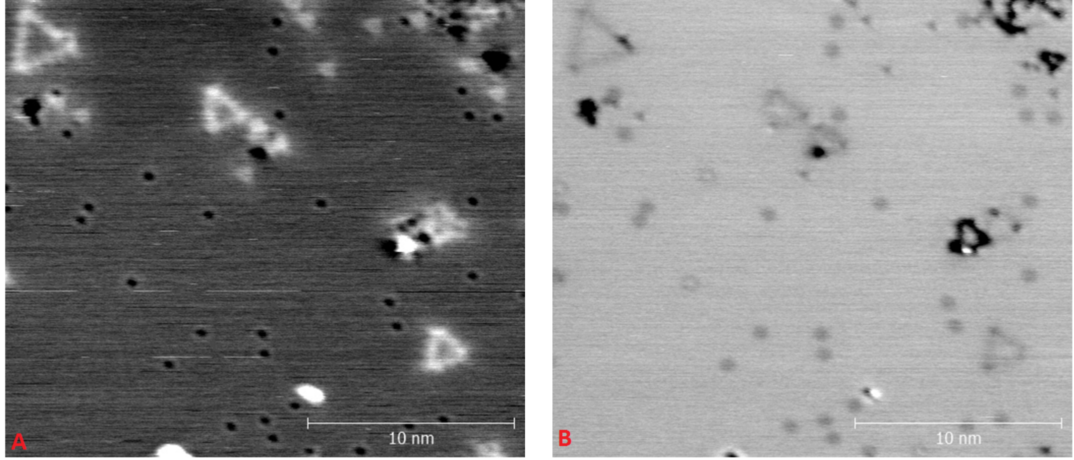

Figure 5.2: The same area of the surface of Si(111)/Tl-(1×1) taken by the STM with the tip bias: A) -2.3 V B) +2.3 V.

simultaneously with the positive tip bias during the forward scanning motion and the negative tip bias during the backward motion. Some surface defects have the same intensity in relation to the rest of the surface at both polarities (mostly single dot defects or bigger randomly shaped defects). On the other hand, some defects arrange itself into triangles which are brighter than the rest of the Tl-(1×1) surface in the empty states imaging and darker in the occupied states imaging. The triangular shape of defects is the most visible at the bias 2.3 V in both polarities. At lower or higher biases only corners of the triangles were visible and appeared the same as the usual dot defects (however, they still could be detected by the inverse contrast at opposite polarities). The triangular defects were not seen on every prepared surface Si(111)/Tl-(1×1). We suggest that the occurence of the triangular defects is caused by the insufficient temperature of annealing during the creation of the Tl-(1×1) reconstruction.

A deeper analysis of triangular defects (figure 5.3) shows that triangles consist of brighter spots with the periodicity wich is roughly same as the periodicity of dimers in dimer rows of $((2n + 1) \times (2n + 1))$ stacking fault reconstructions. On the basis of the number of maxima on one side of the defect, we state the hypothesis that the defect is the remaining of (11×11) HUC. The lattice constant which was counted from line profiles over the defects is (0.382 ± 0.040) nm on the base of the hypothesis (after the calibration of piezo ceramics). The ideal lattice constant (0.384 nm) is the same within the error range. The orientation of triangles is same as the orientation of faulted HUCs, as we can see from the comparison with the (7×7) surface before the deposition of Tl. Similar objects with an inverse contrast have already been observed by Zotov et al. in [36]. On the basis of our measurements and observations of Zotov et al., we conclude that triangular defects can be interpreted as areas of Tl-(1×1) which has the still present stacking fault underneath (e.g. object on the figure 5.3 is area of the

(11 × 11) faulted HUC; the rest of the surface is already without the stacking fault).

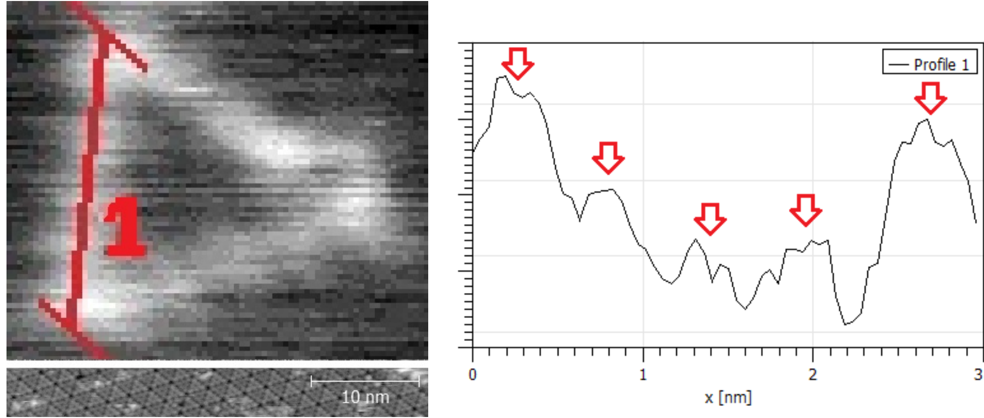

Figure 5.3: The detail of the triangular surface defect observed on Si(111)/Tl-(1 × 1) (top left), the original Si(111)-(7 × 7) reconstruction (bottom left) and line profile over one of the main directions of the triangular defect (right). The scale on the comaparative image of the clean surface Si(111)-(7 × 7) differs from the scale on the detailed image of the defect. The length unit on the vertical axis of the graph is arbitrary.

Since the main goal of this work is to investigate an interaction of adsorbates with passivated Si surfaces, the first step might be to investigate the second monolayer of Tl and find out how thallium passivation affects further deposited overlayers of Tl. Vitali et al. in their work [4] already examined the second monolayer of thallium with interesting results. Unlike the first layer of Tl which creates the reconstruction (1 × 1), Tl in the second layer arranges itself in much looser reconstruction which periodicity is only short-ranged. The periodicity observed by Vitali et al. was interpreted as the Moire patterning induced by an interaction of the first and the second monolayer of Tl. The looseness of the second layer is confirmed by the change in orientation of the reconstruction from one place to another (Vitali et al. observed that one of the main directions of Moire-(6 × 6) elementary cell can change its orientation as much as 8° within a distance less than 20 nm). This observation stands for the extremely small interaction between the two layers in comparison with the intralayer interaction in the second layer (i.e; we can think of the second layer as an almost separate layer floating over the passivated surface).

Our observations of the (6 × 6) reconstruction support results of Vitali et al.. The area of the surface with two terraces and a step edge that separates them can be seen on the figure 5.4). Defects typical for the reconstruction Tl-(1 × 1) (point and triangular defects) are present on the top terrace. On the other hand, the bottom terrace exhibits a pattern with the periodicity (2.4 ± 0.5) nm, which is $((6.2 \pm 1.2) \times (6.2 \pm 1.2))$ reconstruction (see the figure 5.5). Within the error range, it is in the good agreement with the observed value of Viatli et al..

Since some key properties of the Tl-(1 × 1), which are necessary for the usage of Tl as a passivator, were not known until the time of our experiments, it was

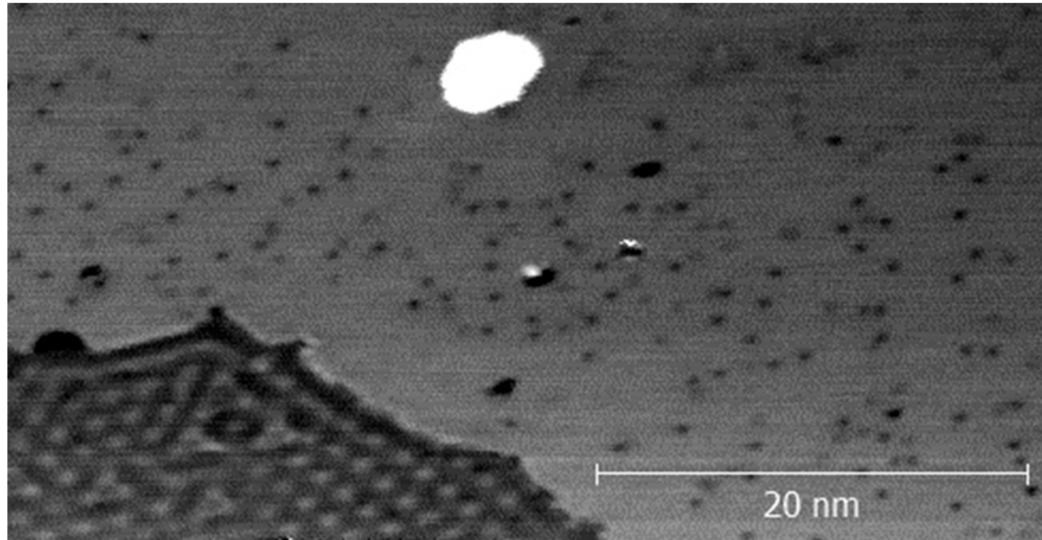

Figure 5.4: The second layer of Tl in the proximity of the step edge of the terrace.

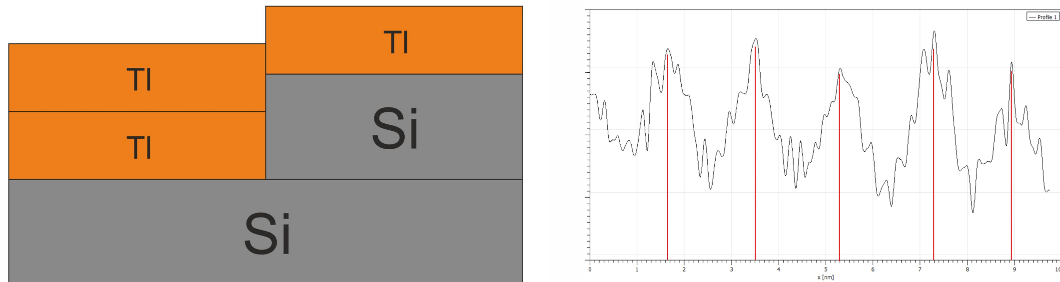

Figure 5.5: The explanational model of the observation from the figure 5.4 (left) and the line profile taken over 5 Moire pattern maxima with approximate positions of maxima marked (right). The length units on the vertical axis of the graph is arbitrary.

necessary to examine the layer more thoroughly. First of all, it was necessary to determine the desorption temperature, which has been used to remove adsorbed thallium from the surface (see figure 4.2- C, D). In order to do so, we executed experiments with the thermal desorption of thallium from the Si(111) surface (see figure 5.6).

After annealing of the surface at temperature $\approx$ 300°C for 2 minutes, the first signs of the desorption begin to appear on the surface (figure 5.6-A). The continuous layer of Tl-(1×1) is locally interrupted by holes which are created by missing desorbed thallium. After further annealing, areas of (1×1) reconstruction begin to shrink and in the range of temperatures between 300°C and 330°C the mosaic reconstruction Tl-$(\sqrt{3} \times \sqrt{3})$R30° arises (figure 5.6-B). After two cycles of annealing at $\approx$ 300°C and $\approx$ 330°C (figure 5.6-C), almost the whole surface is covered by this mosaic reconstruction. With further annealing at higher temperatures, a portion of Tl atoms gradually decreases and the other metastable reconstructions, for example (2×2), $c(2 \times 4)$, $c(2 \times 8)$, (5×5), (9×9) etc., can

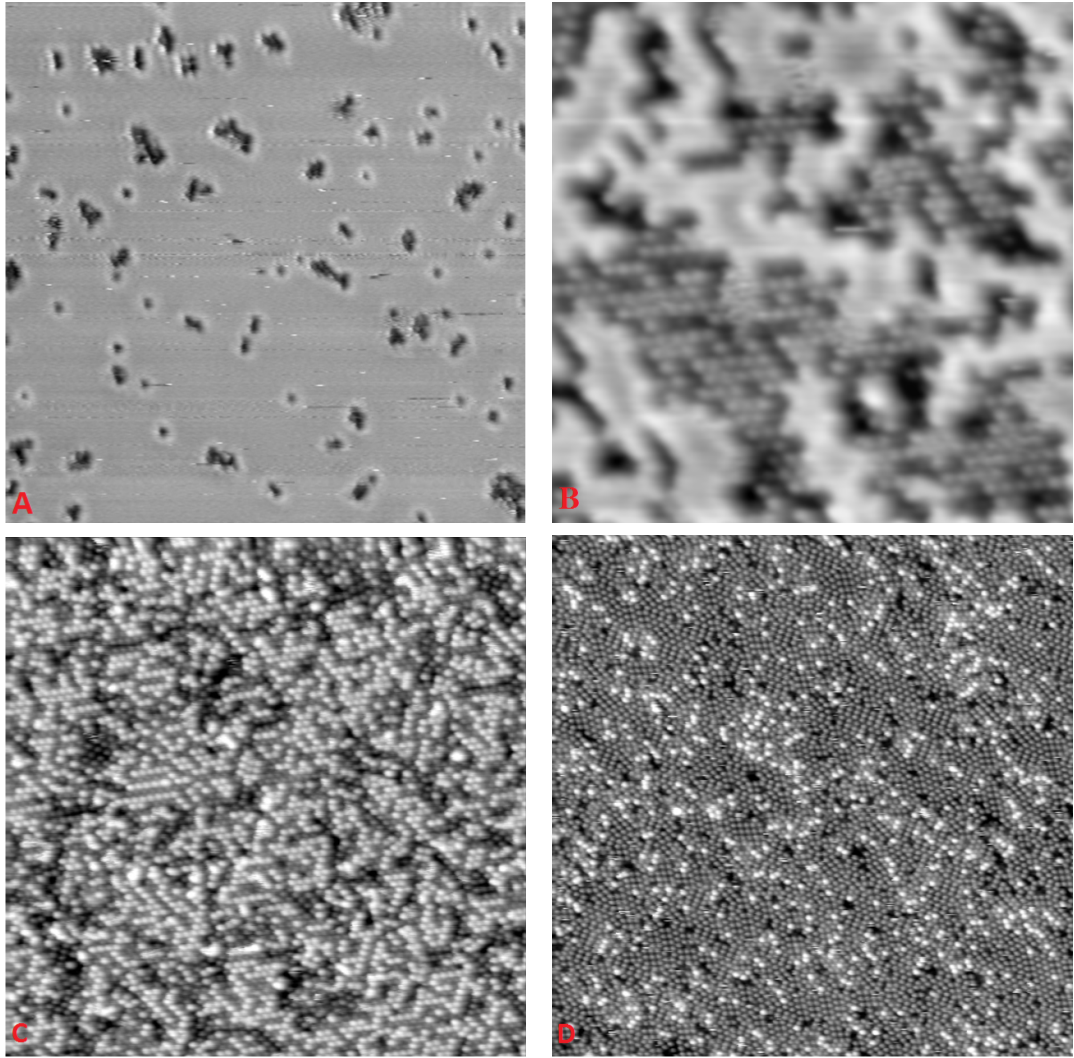

Figure 5.6: Evolution of the surface Si(111)/Tl after annealing (already published in [28]). Surfaces prepared by the adsorption of 1 ML of thallium and further 2 minutes annealing: A) 300°C, area: (40×40) nm^2, tip bias: -0.5 V; B) 330°C, area: (20×20) nm^2, tip bias: -0.3 V; C) two cycles of annealing at 300°C and 330°C, area: (40×40) nm^2, tip bias: +1 V; D) 360°C, area: (50×50) nm^2, tip bias: -1 V.

be observed (figure 5.6-D). The detailed image (figure (5.7)) shows coexistence of different types of stable and metastable reconstructions after the desorption of Tl.

The amount of non-desorbed Tl atoms was extracted from the STM images by usage of the different contrast of Si and Tl atoms. Two extraction methods were applied. The amount of Tl atoms in the (1×1) phase was obtained by the measurement of the covered fraction of the surface. The Tl coverage was subsequently counted on the basis of the knowledge of the density of (1×1) phase. The Tl coverage of the surface covered by the $(\sqrt{3} \times \sqrt{3})$ reconstruction was counted atom-by-atom. The accuracy of applied methods was tested by the determination of the Tl coverage of the surface with the known coverage. The Tl

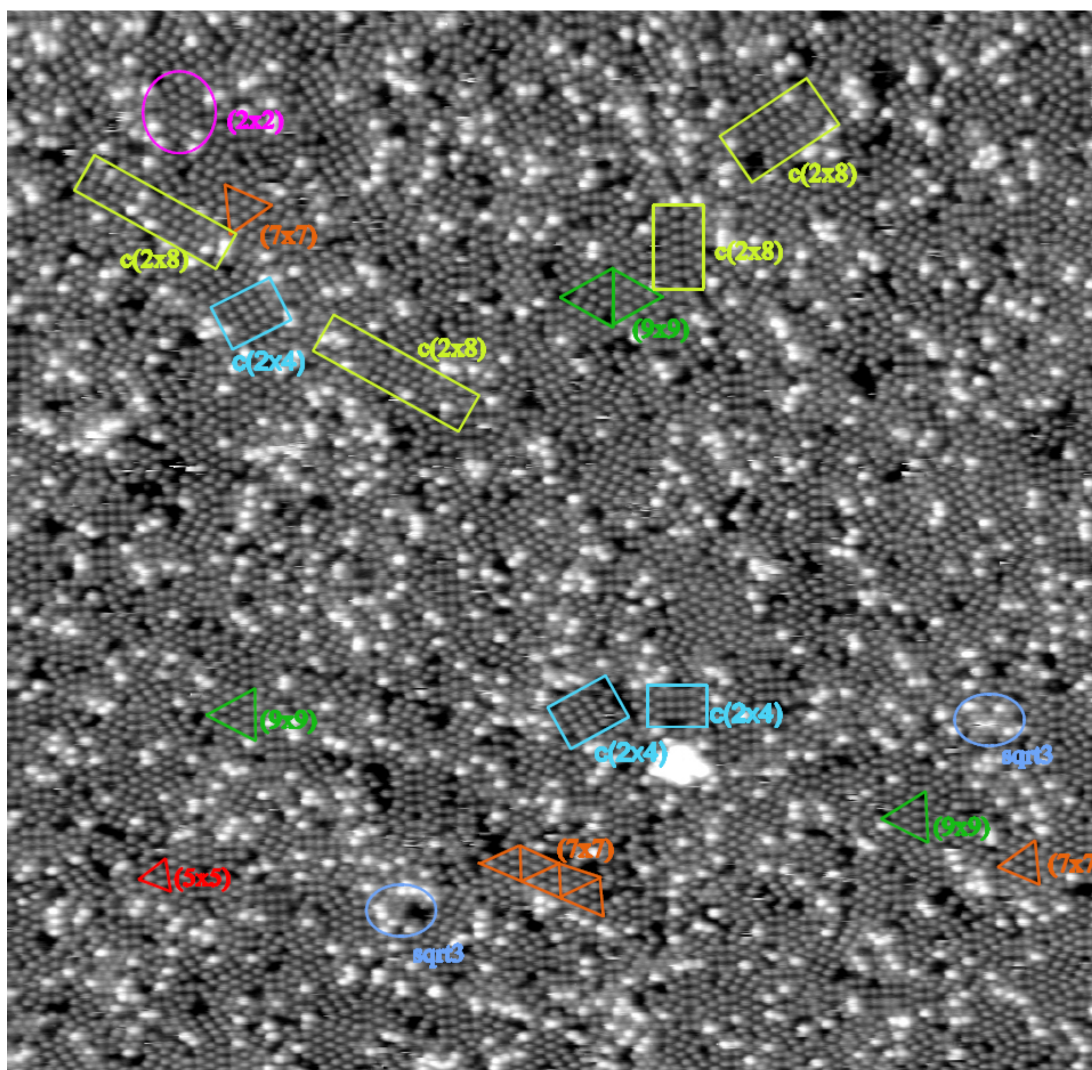

Figure 5.7: The area of the surface Si(111)-Tl after desorption of most of thallium after annealing at 360°C (different types of stable and metastable reconstructions are marked, area: (60×60) nm^2, tip bias: -1 V).

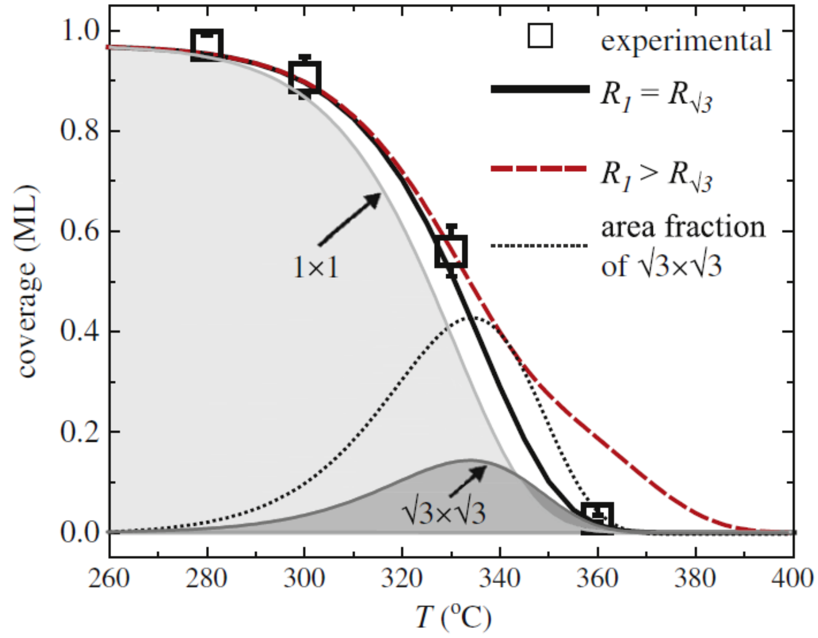

Figure 5.8: Experimental dependence of Tl coverage (squares) on annealing temperature, fitted by first order desorption model with single desorption rate $R_1 = R_{\sqrt{3}}$ (solid line) and with two desorption rates $R_1 > R_{\sqrt{3}}$ (dashed line). The curves distinguished by light gray-shaded and dark gray-shaded areas underneath are (1×1) and $(\sqrt{3}\times\sqrt{3})$ components of Tl coverage with the same desorption energy. The dotted line corresponds to the area fraction of the $(\sqrt{3}\times\sqrt{3})$ structure (already published in [28]).

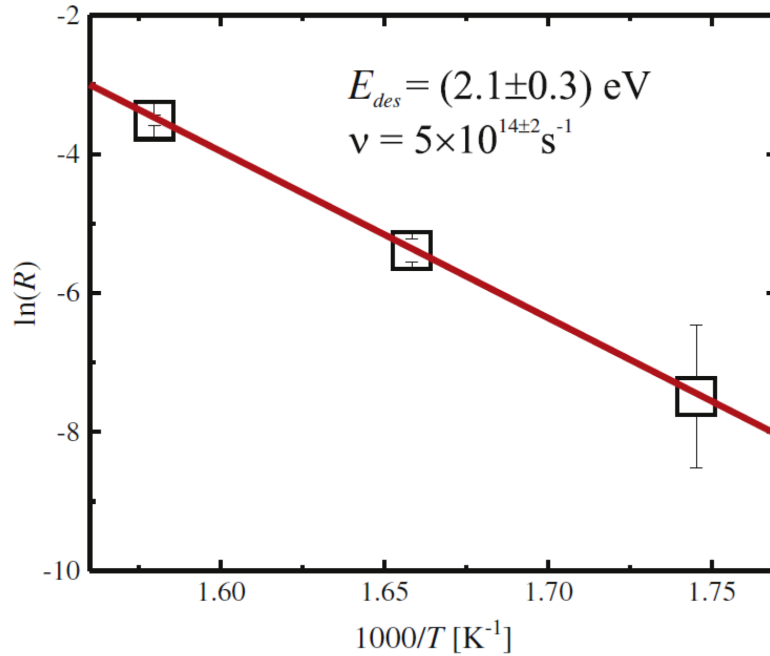

Figure 5.9: Arrhenius plot of desorption rate (squares) obtained from Tl coverage θ using equation 5.2 (already published in [28]).

coverage measured from STM images was in good agreement with the deposited amount within the range of thickness monitoring error (±5%).

The experimental dependence of the coverage on the annealing temperature was obtained by the measurement of the coverage for every set of gathered data (see figure 5.8). The theoretical dependence was subsequently fitted onto the experimental data. Fitting was made with two key assumptions: first of all, the observed desorption is thermally induced; i.e. the equation (2.3) governs the desorption rate R.

$$R = \nu \exp\left(\frac{-E_{des}}{k_B T}\right) \tag{5.1}$$

Here, ν is the frequency prefactor, T is the absolute temperature of annealing, k_B is Boltzmann constant and E_{des} is the desorption energy. Secondly, we assumed that E_{des} is the same for Tl atoms in all structures formed during the desorption. A decrease of the coverage after annealing of the sample for time t can be expressed as:

$$\theta = \theta_0 \exp(-Rt) \tag{5.2}$$

where θ_0 is the initial Tl coverage and t is the length of annealing (in our case $t = 120$ s and $\theta_0 = 0.97$ ML thanks to the intrinsic defects on the surface). The frequency prefactor ν and the desorption energy E_{des} were determined from the linear fit of Arrhenius dependence of $\ln(R)$ vs. $1/T$ (see the figure 5.9). Values of R were calculated from experimentally obtained values of θ using (5.2). The parameters obtained by fitting are: $E_{des} = (2.1 \pm 0.3)$ eV and $\nu = 5 \times 10^{(14\pm2)}$ s^{-1}. After consideration of rate equations and taking in account the coverage of each phase during the desorption, the fitting lines for the case of constant E_{des} and different E_{des} can be plotted (see figure 5.8). Apparently, fitting with the constant E_{des} corresponds to the experimental data better than fitting with $E_{des(1\times1)} < E_{des(\sqrt{3}\times\sqrt{3})}$. The fitting suggests that the E_{des} is constant, therefore binding energy and the valence of Tl in all phases should be same. Since the valence of Tl in the (1×1) structure is one, the experiments suggest that thallium is monovalent in $(\sqrt{3} \times \sqrt{3})$ as well.

The second main result of the fitting is determination of the desorption temperature of thallium. This temperature has been used for removal of thallium from the passivated surface. The lowest annealing temperature of samples which were needed to be thaliumless was determined to be ≈ 400°C. Tl coverage, after annealing at this temperature, should be less than fractions of a percent; i.e., experimentally, the coverage should be immeasurably low (essentially zero).

Chapter 6

Adsorbates on the passivated Si(111)

So far, a wide variety of surface arrangements of metal layers on the Si(111)-(7×7) has been observed. If we restrict our view to the epitaxial growth of the first monolayer, there are still many reconstructions found on Si(111)-(7×7) after deposition of a metal: (1×1), $(\sqrt{3} \times \sqrt{3})$, $(\sqrt{31} \times \sqrt{31})$, (2×1), (4×1) etc..

This work is devoted to the research of surfaces prepared by the thallium passivation and to the comparison of those surfaces with surfaces prepared without the passivation. For this purpose, we chose to observe aluminium and indium as adsorbates. The reason was the richness of their reconstructions observed on the surface Si(111), which should help us in the easier identification of passivation effects. Due to an electronic similarity with silicon and a size similarity with indium, we also chose to observe tin. An important property of the passivated surface is its stability in hostile conditions and inertness against other chemicals. Since manganese is known for its high chemical reactivity with silicon even at room temperature [37], it is the right element to test the stability of the passivating layer.

6.1 Manganese

6.1.1 Mn on Si(111)-(7×7)

Manganese on Si(111)-(7×7) is known for growing epitaxially and is reported to result in the ("1×1") and $(\sqrt{3} \times \sqrt{3})R30^\circ$ surface reconstructions depending on the deposition rate, the annealing temperature and the thickness of the film [37, 38, 39, 40]. Reconstruction ("1×1") is a quasi-reconstruction since it is identified only by an observation of a (1×1) pattern in LEED experiments. The structure of this phase is non-crystaline and the observed pattern comes from the underlying substrate.

As Kumar et al. [37] observed, manganese forms the quasi-reconstruction ("1×1") at room temperature up to 1 ML coverage. In these conditions, a diffuse pattern from underlying and almost completely disordered silicon is observed in LEED [40]. STM images (figure 6.1) show manganese islands: the largest

clusters are surrounded by a crater in the substrate. This can be explained as the beginning of a silicide formation and an incorporation of silicon atoms from the substrate into the deposited layer [40].

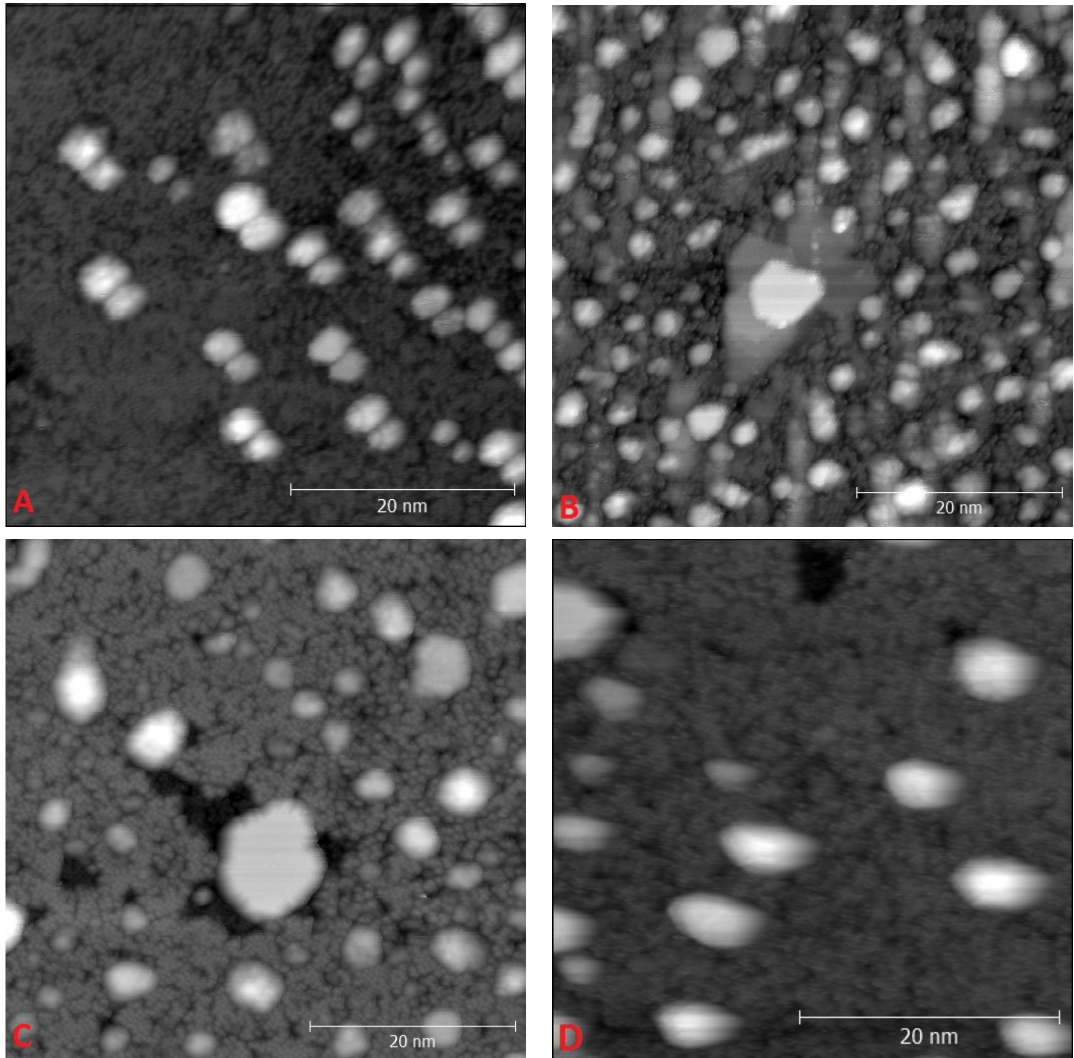

Figure 6.1: Surface Si(111)-(7 × 7) after deposition of submonolayer amount of Mn and subsequent annealing at: A) ≈ 250°C (notice the apparent multiple tip effect) B) after further annealing at ≈ 300°C C) after further annealing at ≈ 350°C D) after further annealing at ≈ 400°C.

At the coverage 1-2 ML, $(\sqrt{3} \times \sqrt{3})R30°$ is present on the surface. Islands are positioned on the top of silicon terraces. Silicon atoms were taken from there and they were incorporated into silicide. Residual areas with the (7 × 7) and the (5 × 5) reconstructions are still visible. At coverage 5 ML, after annealing at 400°, almost the whole surface is covered by the continuous layer of MnSi with an exception of deep holes and ditches, which are necessary as a mean of relieve of the surface strain [37]. This is caused by the lattice constant mismatch of silicon and manganese silicide. Unreacted silicon is on the very bottom of the holes (according to Kumar et al., this can be the possible source of silicon for the silicide creation after further deposition of Mn). Relief of the surface strain also

induces creation of strain relief networks on the flat platforms of the surface [37].

Basic electrochemical properties of the Mn layer can be deduced from valence band spectra and core level photoemission spectra shown in [37]. It can be concluded that the ("1×1") surface phase has a semiconducting character, while the ($\sqrt{3} \times \sqrt{3}$) phase has a metallic character caused by the presence of electron states at the Fermi level. On the other hand, strong chemical reactivity between Mn and Si can be concluded from Si 2p peaks from the core level photoemission spectrum [37]. The peaks are shifting to the lower binding energies with the change of phases; i.e. with the change of the preparation temperature. The shift of the peaks is caused by the charge transfer between silicon and manganese after a creation of the bond. Since the shift of the peaks is already visible between the clean surface Si(111)-(7×7) and the same surface after the deposition of Mn at room temperature without a further heating, it can be concluded that the reaction between Mn and Si occurs even at temperatures as low as ≈ 300 K.

In order to describe an effect of thallium as a surfactant, we executed experiments with manganese on the clean surface Si(111)-(7×7) prepared by a deposition and further heating at different temperatures. Than we compared those surfaces with surfaces prepared by the thallium mediated growth as it is shown on the figure 4.2.

Figure 6.1 shows pictures of the clean silicon surface Si(111)-(7×7) after deposition of submonolayer amount of manganese and further annealing at $\approx 250°$C, $\approx 300°$C,$\approx 350°$C and $\approx 400°$C. If we neglect the image 6.1-A (multiple tip), it is apparent that the average surface of single island is rising with rising temperature of annealing. Consequently, the surface density of islands is changing from the high of $[(65 \pm 16)/1000]$ nm^{-2}, through $[(20 \pm 5)/1000]$ nm^{-2}, to the low of $[(7 \pm 2)/1000]$ nm^{-2}.

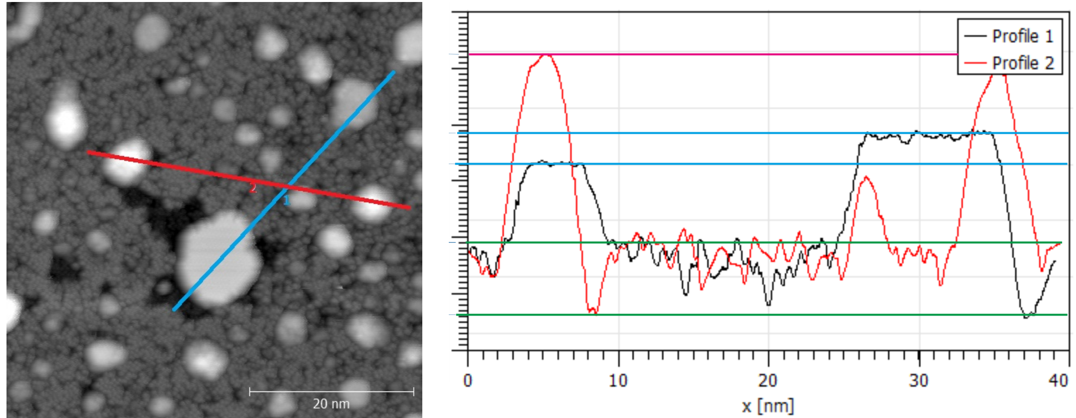

Figure 6.2: Two line profiles taken over two tabular islands (profile 1 - the blue line on the left image) and over two irregular islands (profile 2 - red line on the left image).

Measurements on each temperature exhibit 2 types of islands. As can be seen on the line profiles taken from the surface prepared at temperature 350°C (see the figure 6.2), we can distinguish that one type of islands is tabular. The height of these islands is at least 1.2 times bigger than the step height of the silicon bilayer (measured with respect to the top silicon layer). The same type of islands

was observed by other groups [37, 38, 41] which established that main compound of the islands is MnSi (based on I-V curves and measuremets executed at other temperatures). The second type of islands is usually higher (we observed heights at least 2 times the step height of the silicon bilayer). The shape of islands of this type, in comparison with the first type, is not tabular, but irregular (mostly conic), as can be seen on the line profile. We do not mention the upper limit of the height of islands because of the fact that according to Zou et al. [42], there is a dependence of the height of islands on the temperature of annealing and other growth parameters.

6.1.2 Mn on Si(111)/Tl-(1×1)

After experiments with manganese on the clean silicon surface, we prepared the surface of silicon passivated by one layer of thallium in the reconstruction (1×1). As was described before in the section dedicated to thallium overlayers on silicon, islands with the Si step height are present on the surface (see the figure 6.3). A big diffusivity of an adsorbate on the surface is also expected (see the chapter 5).

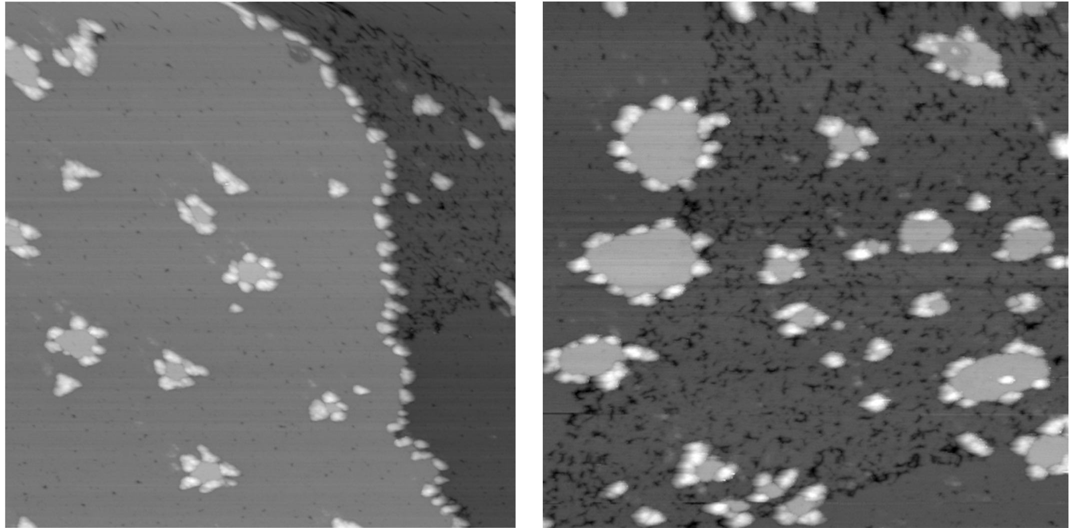

Figure 6.3: The passivated surface Si(111) after deposition of Mn (defected areas of Tl-(1×1) are caused by the deposition of Tl onto the incompletely reconstructed surface Si(111)-(7×7)), displayed areas: left: (150×150) nm^2, right: (100×100) nm^2.

The surface observed after the deposition of Mn onto the Si(111)/Tl-(1×1) can be seen on figures 6.3 and 6.5. From a comparison with the clean surface Si(111)/Tl-(1×1) we concluded that the brightest features of the surface consist of manganese (see the explanation figure 6.4). Mn surrounds islands and step edges and grows in mode that we named "stick and stay" (the name was originally the name of the Monte Carlo simulation model which describes the final state of the surface on the figures). Consistently with expectations, we observed a surface that bares a sings of a high diffusivity of Mn. For instance, a decoration effect on the step edges is apparent on every picture of the surface. Interestingly, if manganese

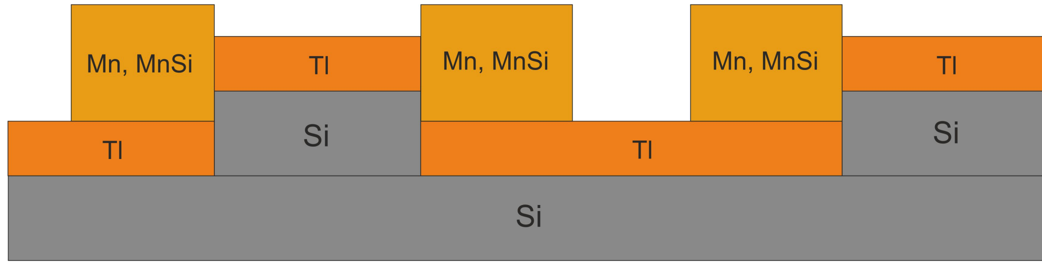

Figure 6.4: The explanational model of manganese islands growing on the step edges of Si(111)/Tl-(1×1)

sticks to some point of an island or some point of already stuck manganese, it does not diffuse along the step anymore. This results in a dendritic character of the Mn covered areas. In other words, measurements suggest that the energy barrier for the diffusion on the clean surface E_d is much smaller than the energy barrier for the diffusion along the step edges E_{ds}.

After deposition of bigger amounts of manganese, the model stick and stay is even more apparent, as the dendritic mode of growth sustains (see figure 6.5). Monte Carlo simulations with an extreme case of initial and boundary conditions

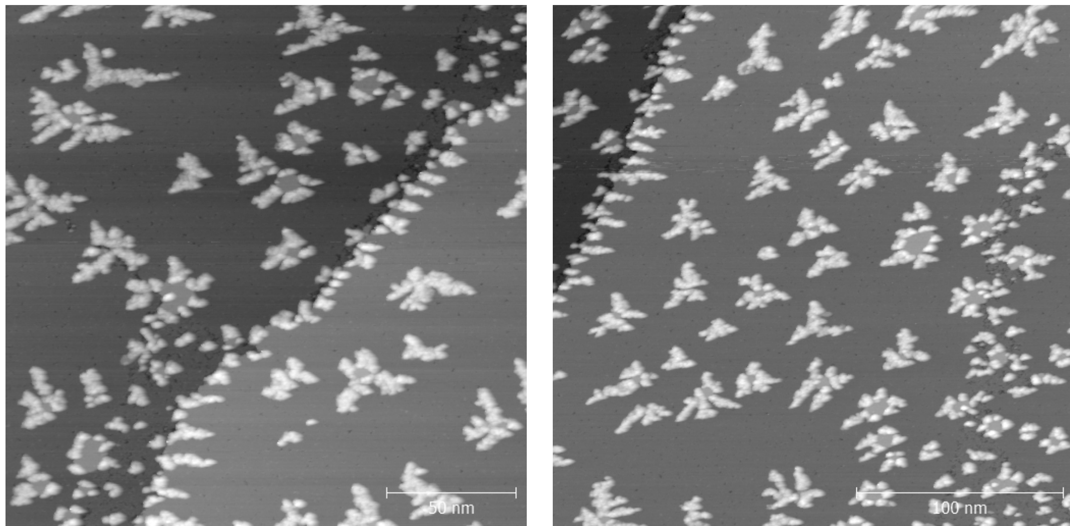

Figure 6.5: Passivated surface Si(111) after a deposition of a bigger amount of Mn.

typical for this surface were also executed. The simulation itself was computed on an array of 100×100 points where each point represented one adsorption position. Each point held value 0 or 1 which denoted whether the particular position is occupied by adsorbate or not. At the beginning of the simulation, some stable points (not changing its value) were marked as occupied ones. This stood for the stable silicon-step islands that occur on the Si(111)/Tl surface. After the initialization, adsorption was simulated by the one-by-one marking of the preset number of positions as occupied. In one cycle of calculation, only one adatom position was changed. The calculating cycle for one particle was ended

when the particle reached a stable position, which is a position with at least one neighbouring adsorption site already occupied (from this: stick and stay model). As a parallel to the experiment, the movement of a particle until reaching of a stable position, corresponds to the infinite diffusivity of an adsorbate. On the other hand, sticking to the first stable position stands for the non-diffusing along the step edges or within the Mn islands. The final result of the calculations can be seen on the figure 6.6. The overall similarity between appearances of the calculated surface and the experimentally measured surface is obvious (the dendritic character of islands which are located primarily on initial stable points; i.e. initial Si-step islands). Therefore, we can conclude that the growth conditions of experiments were similar to those used in the calculations (an extremely high diffusivity of an adsorbate on the clean surface and a low diffusivity along the step edges and within the islands).

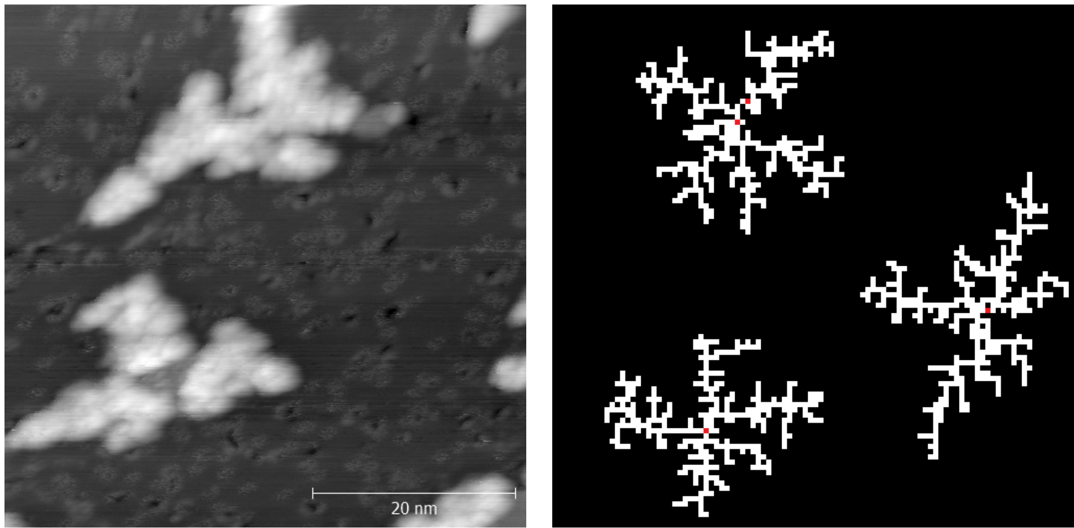

Figure 6.6: The comparison between the obtained image of the Si(111)/Tl-(1×1)/Mn surface (left) and the Monte Carlo simulation of the surface in the "stick and stay" mode of growth (right).

6.1.3 Mn on Si(111) after desorption of Tl

The final step in a thorough investigation of thallium as a passivator of Si(111) for manganese is an observation of the surface after the thermal desorption of thallium. The thermal desorption was obtained by annealing of the sample at temperature $\approx 400°$C, since it was established as the lowest temperature enabling the secure removal of adsorbed thallium (chapter 6). An appearance of the surface after the annealing is shown in the figure 6.7. Note the significantly bigger area of the displayed surface in comparison with areas on the figure 6.1 (measurements with manganese deposited directly to Si). The most striking feature of the surface is its drastic change of density of islands. While in the case of direct deposition of Mn, the minimal density of islands after annealing at temperature $\approx 400°$C was observed to be $[(7 \pm 2)/1000]$ nm^{-2}, after the thallium mediated growth the average density decreased substantially to $[(0.23 \pm 0.05)/1000]$ nm^{-2}. The

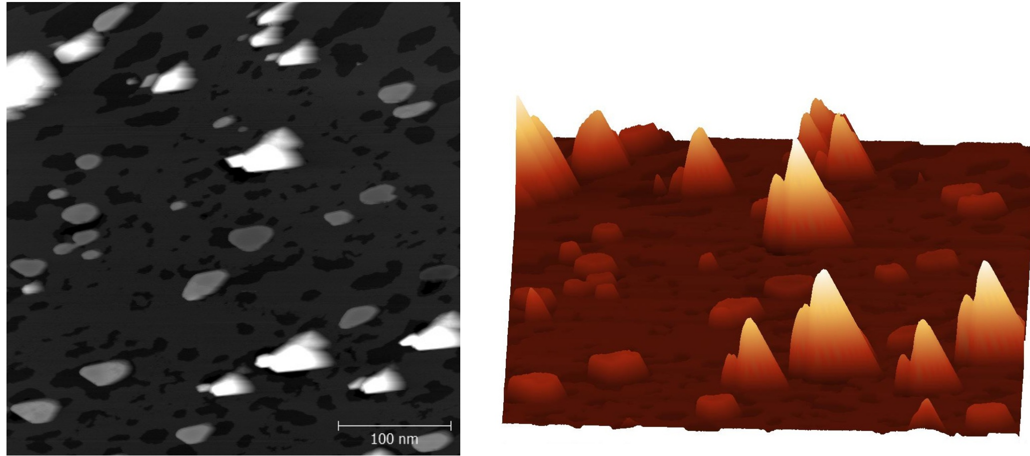

Figure 6.7: The Si(111)/Mn surface after the thermal desorption of Tl. 2D image (left) and 3D image (right) of the same area are shown in order to highlight the big height difference of one type of islands in comparison to the other type.

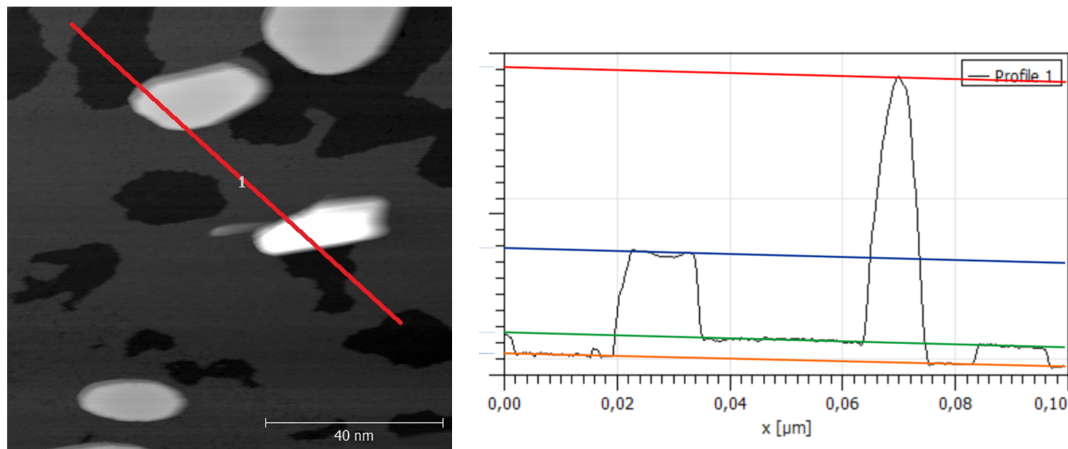

Figure 6.8: The height calibration of observed Mn islands. The length units on the vertical axis of the graph is arbitrary.

common feature of these two measurements is an appearance of holes in the top silicon bilayer. Almost uniform distribution of the holes over the whole surface was observed. A juxtaposition of measurements with and without thallium shows that not only islands, but also holes enlarged its average individual size. We suggest that enlarging of both features is caused by the higher mobility of the adsorbate and silicon.

Besides the change of the average size of islands and holes, the shape of the islands is different too. Two types of islands are observed: round tabular lower islands and rather elongated sharp-edged and significantly higher ones. On the basis of the comparison of our experiments with directly deposited Mn with the observations of other groups [37, 41, 42], we conclude that tabular islands have the same nature as the tabular islands on the figure 6.1. Hence, the main compound of this type of islands is MnSi in the $(\sqrt{3} \times \sqrt{3})$ reconstruction.

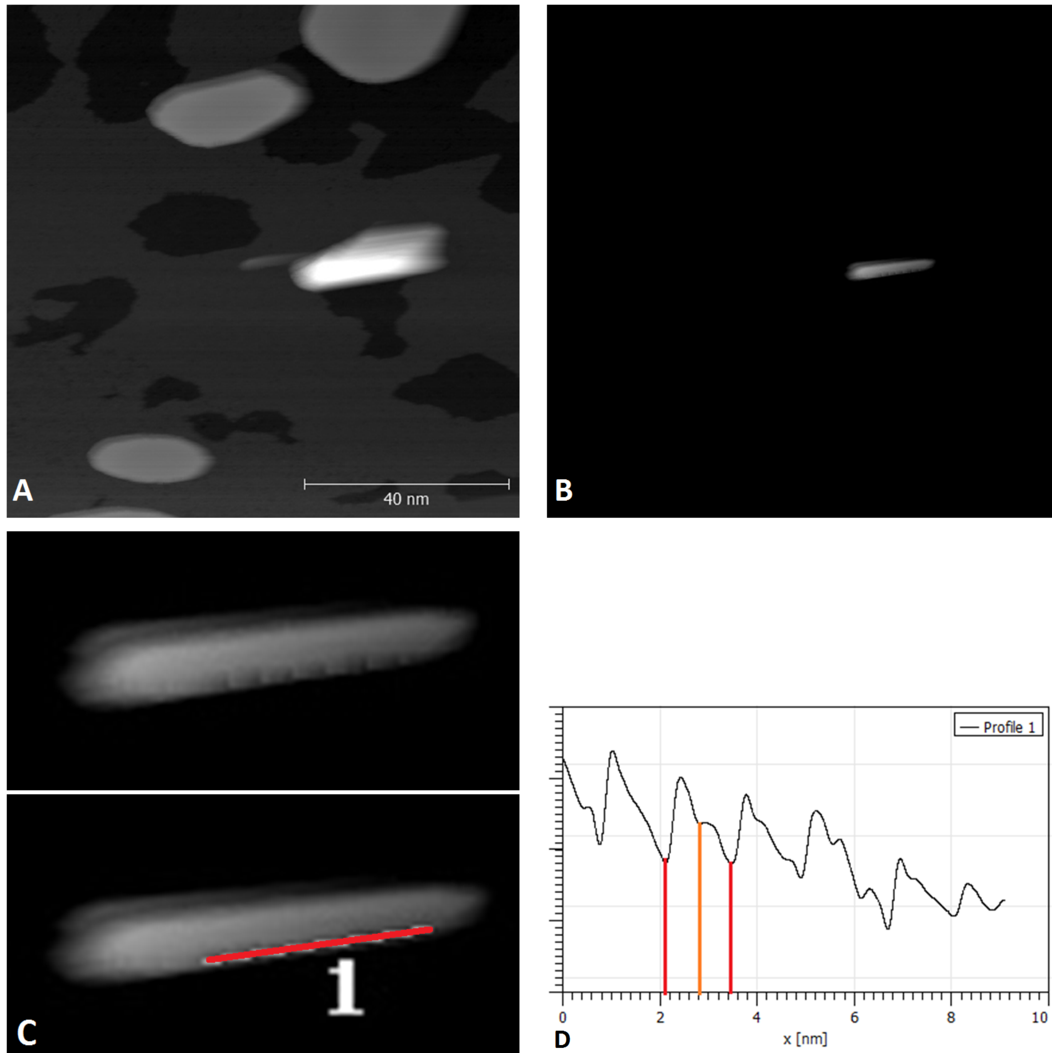

Figure 6.9: The determination of periodicity of manganese nanowires: A) the originally obtained image of the typicall area of the surface B) same image with the brightness discrimination for highlighting the shape of nanowire C) the detailed image of nanowire with the marking of line used for the line-profiling D) the line profile showing the periodicity of the nanowire (two lower minimas and one higher minimum marked; the length unit on the vertical axis is arbitrary).

The recognition of the second type of islands is not so straightforward. An atomic resolution of this type of islands is not obtained. The reason is following. STM images are in fact convolutions of the morphology of the sample and the tip. In order to gather the signal from the smallest possible area of the surface, the ideal STM tip should have the shape of a delta function. In real STM measurements, it is necessary to have the tip which has the taperness that is higher than the taperness of the most tapering object on the surface. In a case of unfulfilling of this condition, objects displayed by the STM are unresolved and exhibit shady features as ones that are present on the figures 6.7 and 6.8. In spite of the fact that an atomic resolution of the whole structure of islands was not achieved, we were able to utilize the elongated shape of islands in order to resolve the periodicity

of its structure at least in one direction (the taperness of islands is higher in the direction perpendicular to the direction of island's elongation). On the figure 6.9 we can see series of pictures leading to the explanation of the procedure which enabled us to extract the line profile. First of all, the color discrimination of lower parts of the surface was necessary to highlight areas on the tops of islands. The discrimination shows that elongated islands are in fact linear objects with periodicity (0.7 ± 0.1) nm shown on the figure 6.9-C. The periodicity is roughly twice the silicon lattice constant 0.384 nm.

We consider the extraordinary height of the linear islands to be an important property. Therefore, we measured it by the calibration against the step height of the silicon billayer (0.314 nm [43]); see figure 6.8. Since the ratio between the step height and the island height was measured, the height of linear islands was determined to be (3.9 ± 0.6) nm with respect to the top layer of Si and (4.3 ± 0.6) nm with respect to the bottom layer of Si. Similarly, the calibrated height of tabular islands was found out to be (1.6 ± 0.3) nm with respect to the top layer of Si. The calibrated height of linear islands suffer from the bigg error due to the finite speed of the STM feedback loop (we estimated the real error up to 25%).

The specification of islands shape, height and periodicity in one direction brought us to conclusion that observed objects are manganese silicide nanowires, which have already been observed by Zou et al. [41, 42]. Nevertheless, our preparation method differs from the one used by Zou et al. since they prepared the surface by direct deposition of Mn on the surface which was preheated to $\approx 530°$C. In our case, the highest temperature that was used for preparation of the sample was, due to the usage of thallium, only $\approx 400°$C.

6.1.4 Manganese: summary

The growth of manganese overlayers in the submonolayer regime on Si(111)-(7×7), Si(111)/Tl-(1×1) and Si(111) after the desorption of Tl was studied. In agreement with the previous observations of other groups, we observed growth of two types of islands on the clean Si(111)-(7×7): tabular islands created by MnSi in $(\sqrt{3} \times \sqrt{3})$ phase and irregular 3D islands which consist of Mn and MnSi in disordered ("1×1") phase. At $\approx 400°$C, the majority of adsorbed Mn was observed to be incorporated in epitaxial tabular islands. The density of islands on the surface rises with the rising temperature of annealing. At $\approx 400°$C, it was measured to be $[(7 \pm 2)/1000]$ nm^{-2}.

In comparison with the direct deposition of manganese onto Si(111)-(7×7), the final appearance of the surface which was prepared by the thallium mediated growth is different in a number of aspects. No irregular 3D islands were observed on the surface. Surface density of tabular islands is significantly lower: $[(0.23 \pm 0.05)/1000]$ nm^{-2} (i.e. the average size of tabular islands is significantly higher). In comparison with direct deposition, a new type of islands emerged after the thallium mediated growth (high, elongated ones). Islands of this type were identified to be MnSi nanowires, whose growth was observed before on the clean Si(111) surface at temperature $\approx 530°$C, which is higher than our annealing temperature ($\approx 400°$C).

At intermediate stages of growth (Mn on Tl-(1×1)), manganese exhibits a

decorating effect on slicon steps. The effect is the more apparent, the bigger the coverage is. Monte Carlo simulations reveal that obtained data correspond very well to the model "stick and stay". The model works with two essential assumptions: infinite diffusivity of adsorbate on the terraces and almost no diffusivity of the adsorbate after attachement to the step edge or an already existing island.

6.2 Aluminium

6.2.1 Al on Si(111)-(7×7)

Aluminium, the element which lays in the group III.A and the period 3 of the periodic table of elements, belongs to the group of post-transition metals [44] (same as indium, thallium and tin). It has the valence 3 and the atomic radius 143 pm. It is well known for its high chemical reactivity and abundance in earth crust [45]. In a pure form, it crystallizes in the face-centered cubic structure.

From the point of view of the surface science of Al on Si(111), the epitaxial growth of aluminium in the submonolayer mode of growth in 3 different reconstructions was reported: the (7×7) ((7×7), α-(7×7), γ-(7×7)), the $(\sqrt{3} \times \sqrt{3})$ and the quasi-reconstruction ("1×1") [46] (see figure 6.10).

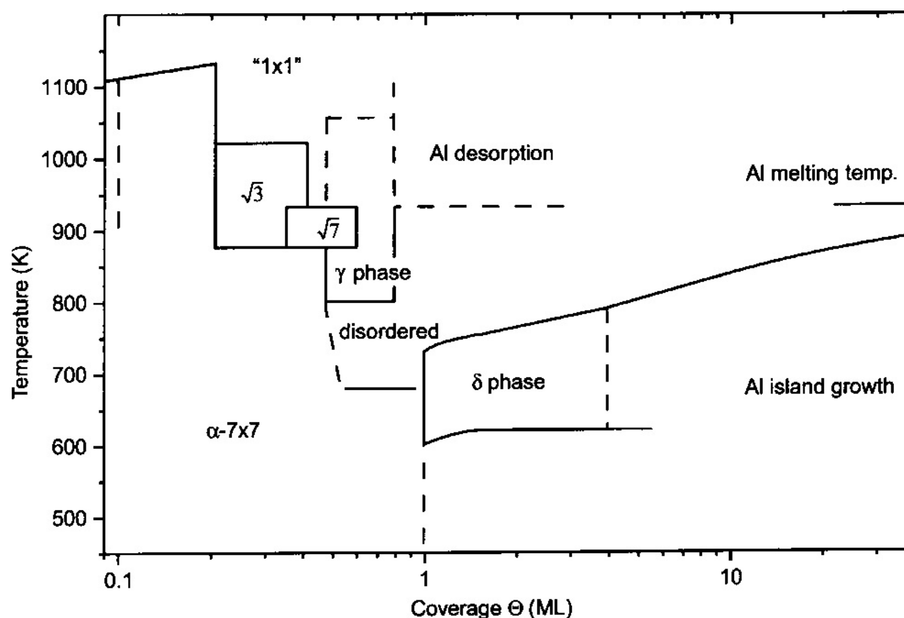

Figure 6.10: Phase formation diagram of the Al/Si(111) system [46].

At low coverage (lower than 0.2 ML) and low preparation temperature (lower than 700°C) exclusive growth of the α-(7×7) reconstruction was observed. Different models which describe the structure of the phase at different coverage, were published [47, 48]. It was proposed that Al adatoms in this arrangement occupy the rest adatom and dimer sites of the DAS structure. Two remaining reconstructions with the (7×7) symmetry emerge at significantly higher temperature and coverage (from 0.25 ML and 800°C).

The Si(111)-$(\sqrt{3} \times \sqrt{3})$-Al phase is the most investigated structure of the Al/Si(111) system and thanks to the fact that it is so well known, it is even used for evaluation and calibration of measuring methods [49]. From theoretical studies [50], photoemission spectroscopy [24], electron diffraction and spectroscopy [51], and STM experiments [52], it was concluded that Al atoms of the $(\sqrt{3} \times \sqrt{3})$ structure saturate all dangling bonds of the Si substrate and reside in the fourfold top T_4 positions rather than in the threefold hollow H_3 sites [25].

Since the experimental method in this work is the STM, the crucial point is distinguishing of different types of atoms on STM images. In earlier STM

experiments with $(\sqrt{3} \times \sqrt{3})$-Al [52], selective imaging of Al and Si adatoms at different voltages was observed. Hamers et al. [52] in their work observed bright imaging of Al adatoms in the root-three reconstruction at negative tip biases, while the imaging was inverse and Si adatoms were observed to appear brighter at positive tip biases.

In the work of Uchida et al. [53] the inverse imaging even at the same polarity of voltage was documented in a case of low coverage of Al (less than 0.01 ML) on Si(111)-(7×7). At tip voltage below -1 V and above +1.2 V Al atoms appear as bright spots adsorbed preferably at three center adatom sites. At voltage between -1 V and +1.2 V, the same bright spots begin to appear dark. This indicates the lack of electronic states on adsorbed Al atoms in a wider vicinity of the Fermi level.

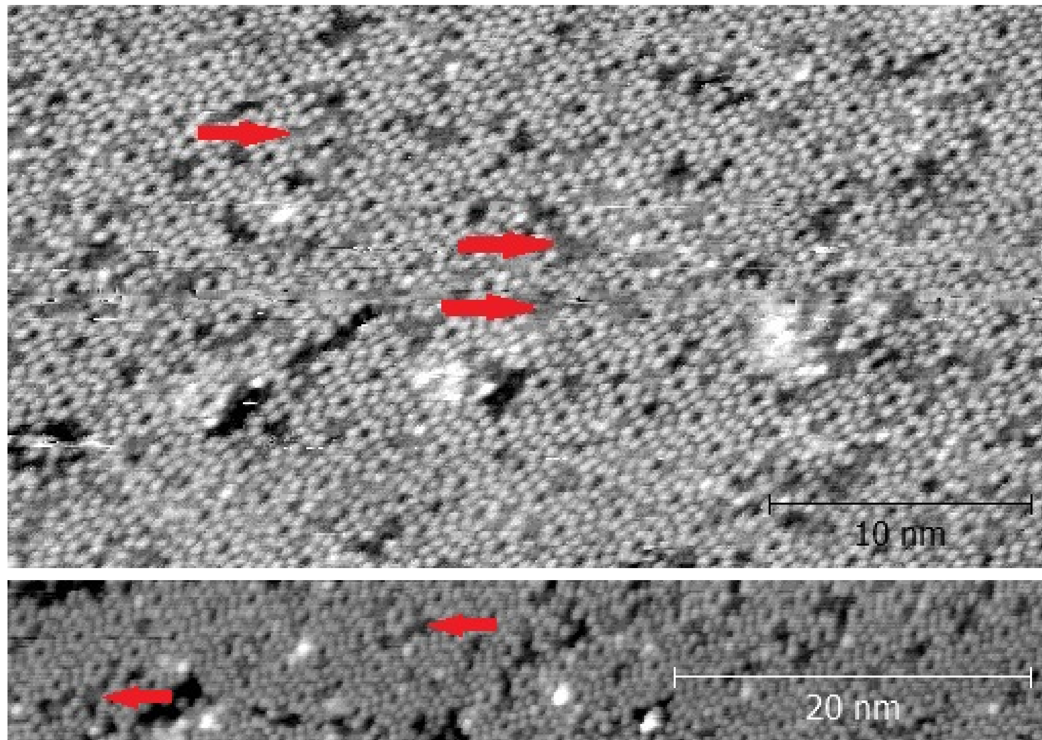

Figure 6.11: Surface of Si(111)-(7×7) after deposition of 0.06 ML of Al and subsequent annealing at $\approx 400°$C ; top: tip bias: -1 V, tunneling current: 0.3 nA; bottom: tip bias: -1 V, tunneling current: 0.2 nA; red arrows show the positions of Al adatoms.

Experimentally, aluminium is the tricky metal to deposit onto the surface. Thanks to its material and surface properties it tends to cover walls of evaporation cells, which limits the temperature of a cell during deposition. In the case of our apparatus, the evaporation cell has an extremely low deposition rate (even at the highest possible temperature of the cell). The coverage we used in the experiment was therefore limited by the apparatus to 0.1 ML. Due to this fact, we chose to employ the recognition of Al and Si atoms based on the significantly different coverages of each component (Si and Al).

After deposition of Al, we annealed the surface at $\approx 400°$C, so we could

compare the surface with the surface which was prepared by the surfactant mediated growth. It is apparent (fig. 6.11) that the whole surface keeps the (7×7) symmetry. We have not observed any bigger area with a different periodicity, except unreconstructed areas created by the quick cooling of the sample during the preparation of the surface Si(111)-(7×7). The mentioned unreconstructed areas were present on the surface before an adsorption of Al. Deposited Al atoms appear as flatter fields on adatom positions in the (7×7) reconstruction, which brightness is roughly in the middle of the brightness of bright adatoms and dark missing adatoms . This is in agreement with an expectation based on experiments of Uchida et al., since the voltage -1 V at which our images were taken is the threshold voltage for Al adatoms to appear bright or dark.

6.2.2 Al on Si(111)/Tl-(1×1)

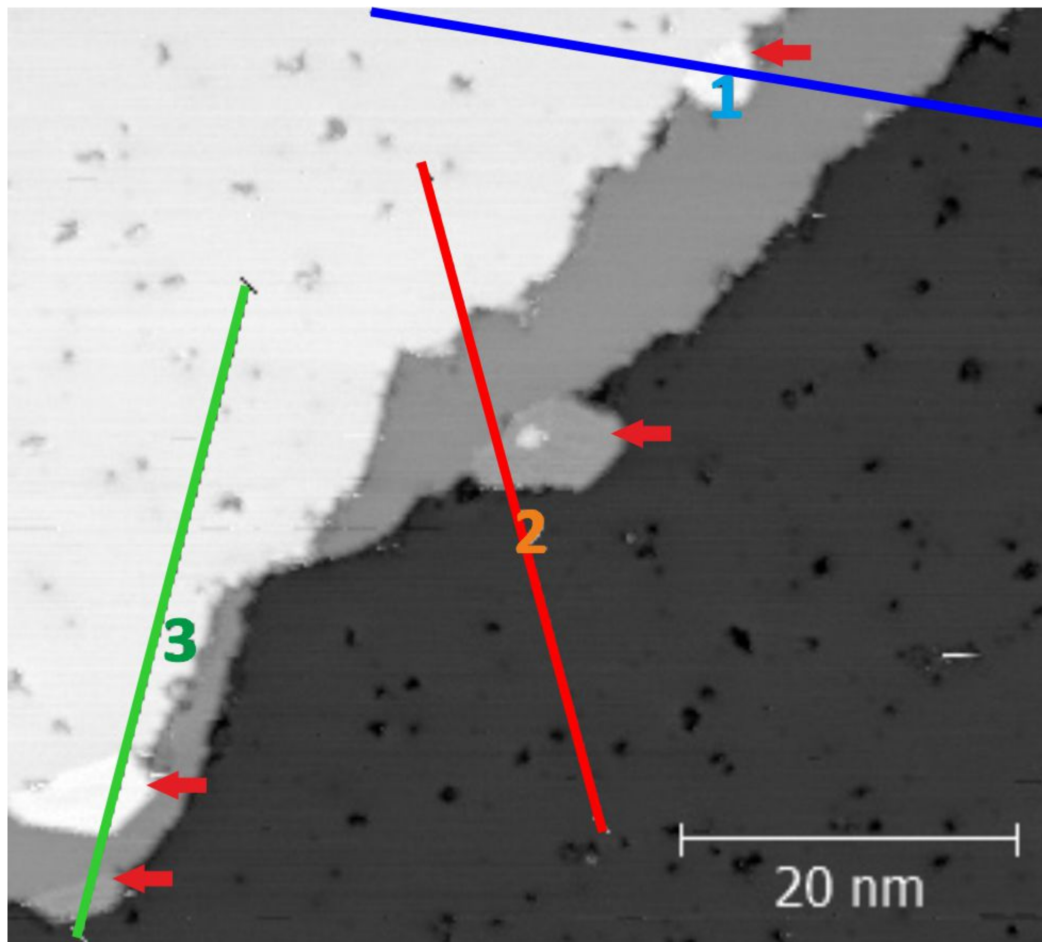

Figure 6.12: Si(111)/Tl-(1×1); tip bias: +1 V, tunneling current: 0.2 nA; red arrows show areas covered by Al. Color lines are used for the line profiling (see the figure 6.13).

An experiment with the passivated surface with the same coverage of Al followed the experiment on the clean Si(111)-(7×7) surface. The sample was annealed only before Al deposition; the first annealing was at $\approx 1200°$C in order

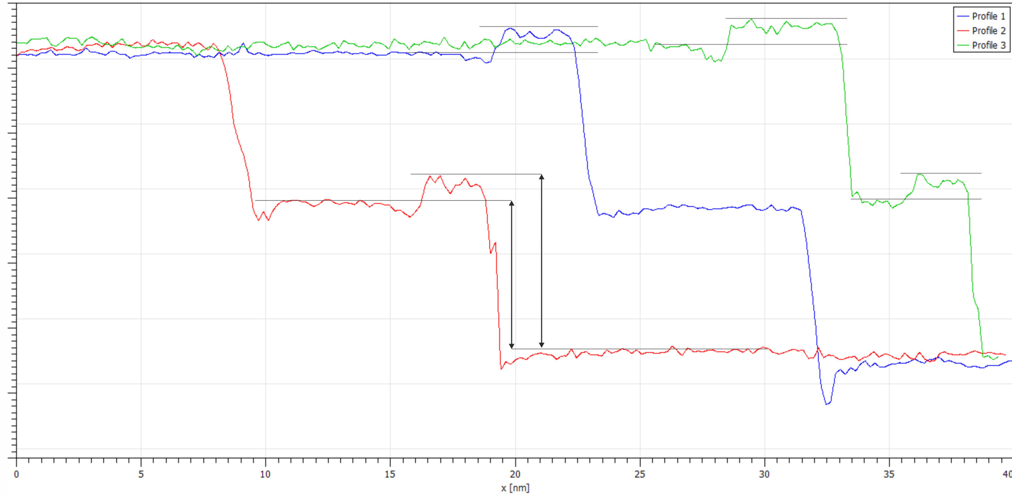

Figure 6.13: Line profiles taken over the area of the surface on the figure 6.12; arrows indicate the height of island and terrace againts the lower terrace; horizontal lines indicate the determined vertical positions of the terraces and islands. The length unit on the vertical axis of the graph is arbitrary.

to prepare Si(111)-(7×7) and the second one was at $\approx 300°$C in order to prepare Tl-(1×1) on top of the surface.

After this preparation, we obtained the surface (see figure 6.12) very similar to the surface of the clean Si(111)/Tl-(1×1) (since the amount of deposited Al was very low). The flat surface with a few Si-step islands and defects described in the chapter 6 was present on our images. Similarly to experiments with manganese, aluminium on the Tl layer was also observed almost exclusively in vicinity of Si steps (or Si-step islands, as they have the same nature). Big diffusivity of Al on Tl-(1×1) is therefore concluded (same as for the case of Mn). Conversely to Mn islands on Tl-(1×1), observed Al islands display much more compact character with smooth edges. This is an indication that an Al diffusion is also possible after an attachment to an island (i.e. mode "stick and stay" is not the case of the growth of Al on Tl-(1×1)). The height of islands was calibrated, as it can be seen on the figure 6.13. The calibrated height is (0.37 ± 0.04) nm with respect to the lower vicinal terrace (the error was estimated as the error of the determination of island's and terrace's vertical positions). Whithin the error range, the height of observed islands is same, which suggests the same nature of the islands.

At room temperature, high diffusivity of aluminium on Tl makes measurements harder. At the low coverage which we had, a substantial part of Al atoms diffuses on the surface at high speed, which makes them undetectable for the STM. Chang et al. state that the threshold deposition coverage for nucleation of islands exists on the passivated systems [3]. Amount of atoms that are present on the surface but are not imaged by the STM was estimated (by Chang et al.) to be as high as 0.09 ML in the case of Ge deposition on Si surface passivated by Pb.

The observed coverage of Al on the surface is approximately 0.01ML. The expected coverage based on observations of the clean Si(111)-(7×7)/Al, the

observations of the passivated surface after desorption of Tl and the knowledge of the deposition rate of the evaporation cell at given conditions is (0.060 ± 0.015) ML. Since we observed much lower coverage of Al than the expected value, we suggest that the rest of Al is diffusing on the surface. The estimated value of Al atoms that are diffusing on the surface is approximately 0.05 ML.

6.2.3 Al on Si(111) after desorption of Tl

After desorption of Tl (annealing at $\approx 400°$C), Al-Si reconstructions emerged on the surface (see figure 6.14). At the given conditions, without an employment of Tl, surface was covered by the reconstruction (7×7) with substituted Al adatoms; as was described above and as it is apparent from the phase diagram (figure 6.10) for Al on Si(111). After the thallium mediated growth, it is obvious

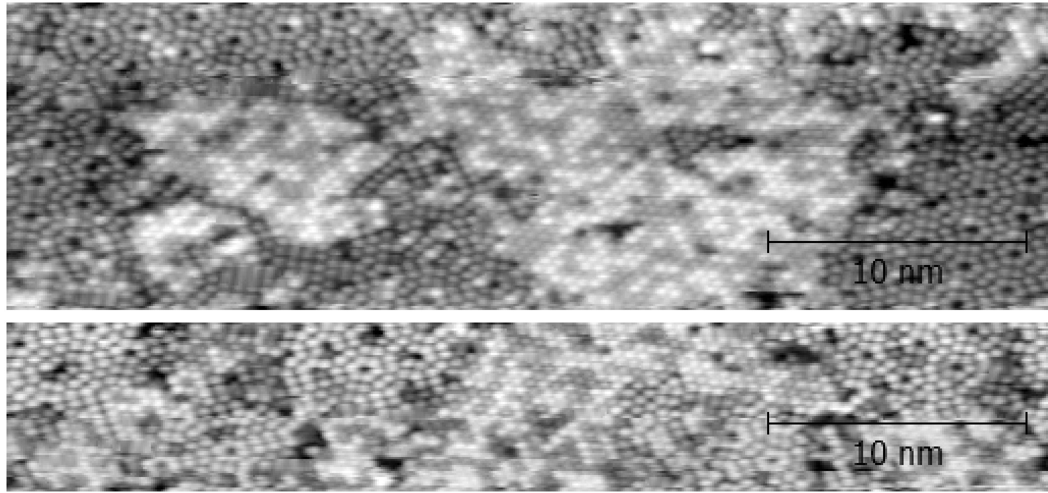

Figure 6.14: Si(111)/Al after desorption of Tl; tip bias: -1.8 V, tunneling current: 0.24 nA.

(figure 6.14) that not only (7×7) periodicity is present on the surface. Large areas are covered by the mosaic reconstruction $(\sqrt{3} \times \sqrt{3})$ which has Al substituted by Si atoms. The size of the area which is covered by the root-three arrangement was measured to be (38 ± 4)%. The fraction of Al versus Si adatoms present in the lattice was estimated to be 1:1 (i.e. 50% of adatoms in the lattice are Al). Identification of Al atoms in the structure was based upon 3 independent facts. First of all, the coverage of Al on the surface should be significantly lower than the coverage of Si. Secondly, intensities of Al adatoms on STM images are in agreement with expectations based on measurements of the other groups [52, 53]. For example, Al adatoms appear brighter in comparison with the rest of adatoms in the lattice at the tip bias -1.8 V (see the figure 6.14). Thirdly, we can identify Si and Al adatoms in (7×7) structure since only few Si adatoms are substituted by Al (we assume, that Al and Si have at least the same contrast in the root-three arrangement as in the (7×7) reconstruction).

We explain the fact that the root-three arrangement emerges at such a low temperature and coverage as follows. The key factor of the root-three reconstruction creation at lower temperature is the cancelling of the (7×7) reconstruction

by the thallium overlayer. After the desorption of Tl, Al can bond directly to the unreconstructed surface, therefore no additional energy is necessary for cancelling the (7×7). Moreover, Al on the Tl-(1×1) creates areas (islands) with much higher concentration of Al as it would be during direct deposition onto the silicon surface. Thus, there are areas on the surface with a much higher local coverage of Al adatoms. These Al atoms can interact with the silicon substrate after desorption of Tl. An extremely high mobility of Al on the Tl-(1×1) compared to the clean Si surface can also act same as an increasing of temperature. Higher mobility causes higher availability of Al atoms; i.e. more attempts of overcoming of energetic barriers. This phenomenon effectively causes an increase in probability of happening of such a process (same as increase in temperature would do).

6.2.4 Aluminium: summary

Data obtained from the Si(111)-(7×7) after a deposition of approximately 0.06 ML of Al are in good agreement with the expected arrangement of the surface based on the previous experiments of other groups. At such low coverage and annealing temperature ($\approx 400°$C), the Si(111)-(7×7) reconstruction is still present on the surface with Al atoms substituting Si adatoms in the topmost layer. Thanks to the low temperature and coverage, the (7×7) reconstruction is not cancelled from the surface and no other reconstruction is observed.

In contrast with the surface created by direct deposition of Al, the mosaic reconstruction $(\sqrt{3} \times \sqrt{3})$ with 50% of Si substitutional atoms is observed on (38 ± 4)% of the surface after the thallium mediated growth. The rest of the surface is still covered by the (7×7) reconstruction with occasional substitutional Al atoms.

Al on Si(111)/Tl-(1×1) creates small islands with smooth edges at low coverage (0.06 ML). Islands are preferably located in vicinity of Si step edges and Si-step islands. The coverage of Al observed by the STM was approximately 0.01 ML. The deposited amount of Al was 0.06 ML, therefore the amount of Al atoms diffusing on the surface was determined to be approximately 0.05 ML. The height of islands was measured to be (0.37 ± 0.04) nm with respect to the bottom terrace.

6.3 Indium

6.3.1 In on Si(111)-(7×7)

Indium is an element placed in the group III.A and the fifth period of the periodic table of elements. It has the same number of electrons on the last layer as aluminium and the atomic radius 167 pm [44] (around the middle of Al and Tl). Since the placement of In in the periodic table is very similar to Al and Tl, some of their properties should be similar and therefore it should be possible to compare the behaviour of each element.

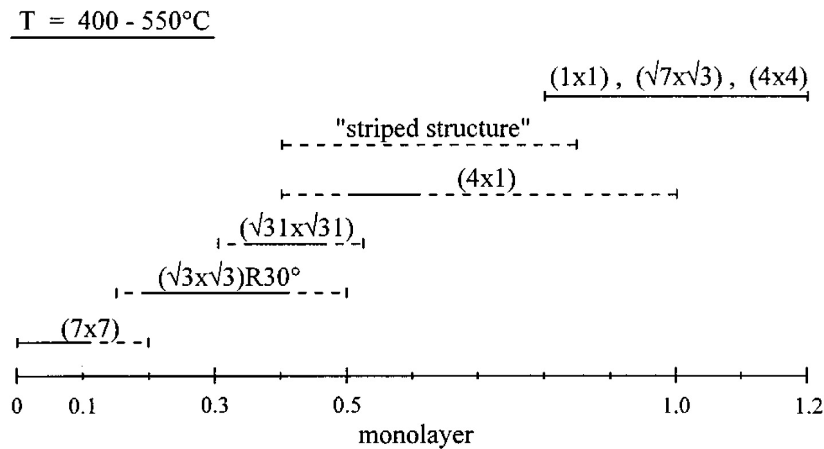

Figure 6.15: Surface phase diagram of In on Si(111) for temperatures of 400 – 550°C based on the STM observations [26].

The reasoning about the similarity of the elements seems to be right, since experimental data gathered on the Si(111)/In until nowadays show many similarities in the surface arrangements that the elements display. For instance, if we choose the area of the phase diagram between 400°C and 550°C (see figure 6.15), we can notice occurrence of the same reconstructions as in the case of Al for coverage under one half of the monolayer ((7×7), $(\sqrt{3} \times \sqrt{3})$). Remarkably, the mentioned reconstructions emerge at much lower temperature than Al reconstructions do. Nevertheless, the atomic structure of these common phases is the same as in case of Al [29].

Selective imaging of In and Si atoms on STM images of Si(111)/In is observed as well. Conversely to the surface Si(111)/Al, imaging of In is reported to depend on the polarity of applied voltage [54] (indium atoms should appear brighter at negative tip biases and darker at postive tip biases). For the case of aluminium, Al atoms appear dark under a given absolute value of imaging voltage (thanks the low density of states near the Fermi level) and appear bright at higher voltage.

We obtained the same results after deposition of approximately 0.23 ML of In on Si(111)-(7×7) and subsequent annealing at 400°C. Contrast in the imaging is the most apparent on figures, where the same area is scanned simultaneously by two opposite voltages. Single atoms can be than identified and their appear-

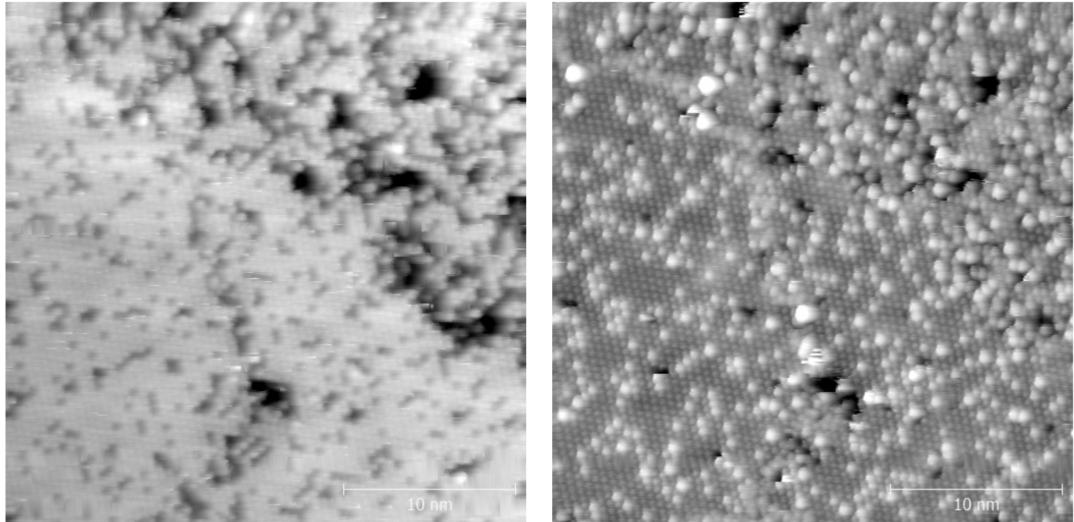

Figure 6.16: Two images of the same area of Si(111)/In taken simultaneously at opposite tip biases (left: -1 V, right: +1 V); the partially unreconstructed area is present on the top right corners of the images aside the rest of the surface covered by the $(\sqrt{3} \times \sqrt{3})$ reconstruction.

ances can be compared (figure 6.16). At higher tip bias (+1.4 V), brightness of substituted Si atoms in indium lattice is even more apparent (figure 6.17).

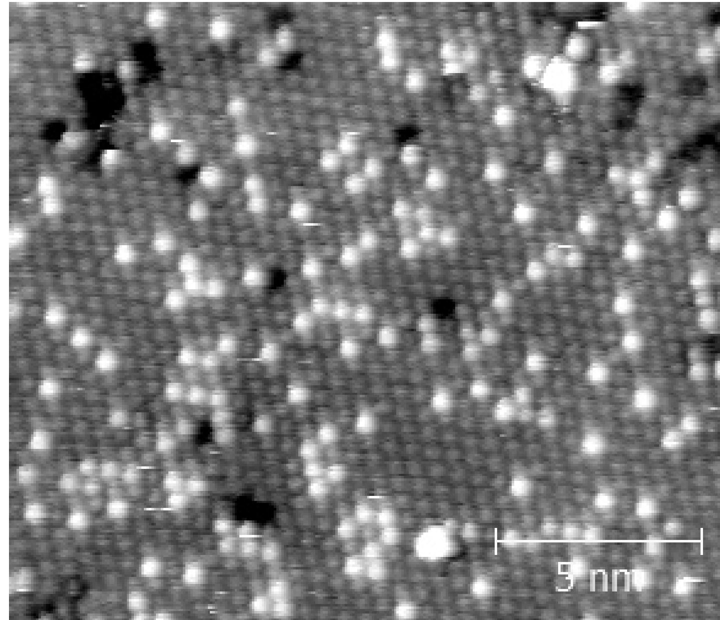

Figure 6.17: The detail of the reconstruction Si(111)-$(\sqrt{3} \times \sqrt{3})$ with Si substituting atoms brightly imaged; tip bias: 1.4 V, tunneling current: 0.2 nA.

Overall, it can be said, that almost the whole surface we prepared was covered by the reconstruction Si(111)-$(\sqrt{3} \times \sqrt{3})$. This is also documented by the above referred figures. Nevertheless, areas with the reconstruction (7×7) with partially substituted Si adatoms were locally present on the surface as well (figure 6.18).

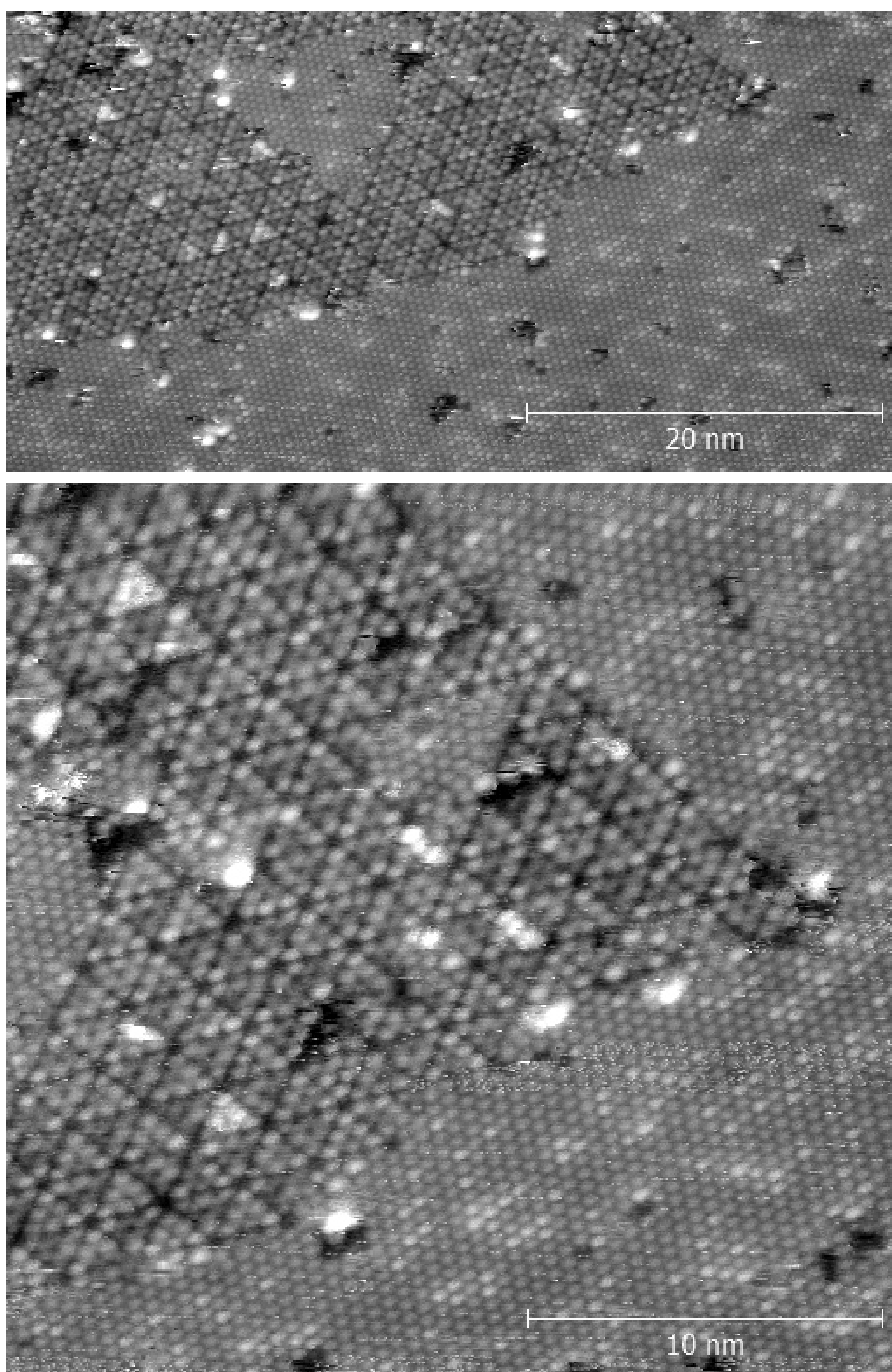

Figure 6.18: Two images of the surface Si(111)/In with the (7×7) reconstruction (tip bias:+1.6 V, tunneling current: 0.2 nA); bottom image is the detailed look at the part of the surface from the image on the top.

6.3.2 In on Si(111)/Tl-(1×1)

Thanks to the experience from experiments with manganese and aluminium on Tl-(1×1), we expected indium atoms to have extremely high mobility on this surface as well. Unlike in the case of aluminium, we chose the higher coverage of indium (approximately 0.23 ML) because higher coverage of indium is much easier to observe.

STM images of the observed suface can be seen on the figure 6.19. Features typical for the Tl-(1×1) surface are present on the images (defects, Si-step islands, areas of the surface which were unreconstructed before Tl deposition etc.). We suggest that new objects found on the surface are In islands. Their characteristic features are a preference of their location in vicinity of Si-step islands or step edges and a very ragged edge.

We propose two possible reasons for the creation of such an edge. Mobility of In atoms can be sufficiently high even in the island structures. The high mobility of individual atoms can result in the fast transformation of island's edges (large clusters of In can change their position fast enough to be imaged at different possitions on the surface while the STM tip is scanning two neighboring lines). Other explanation is based on the fact that the STM tip could interact with the topmost atoms and thus it can push or pull indium atoms on the Tl-(1×1) layer. This explanation is supported by the fact that ragged edges of islands are preferably located on one side of islands (the side which is further in the direction of scanning).

The observed coverage of In was determined to be approximately 0.18 ML. In comparison with the expected value 0.23 ML, it is 0.05 ML decrease of the coverage, which is roughly the same ammount of In unseen by the STM as in the case of aluminium.

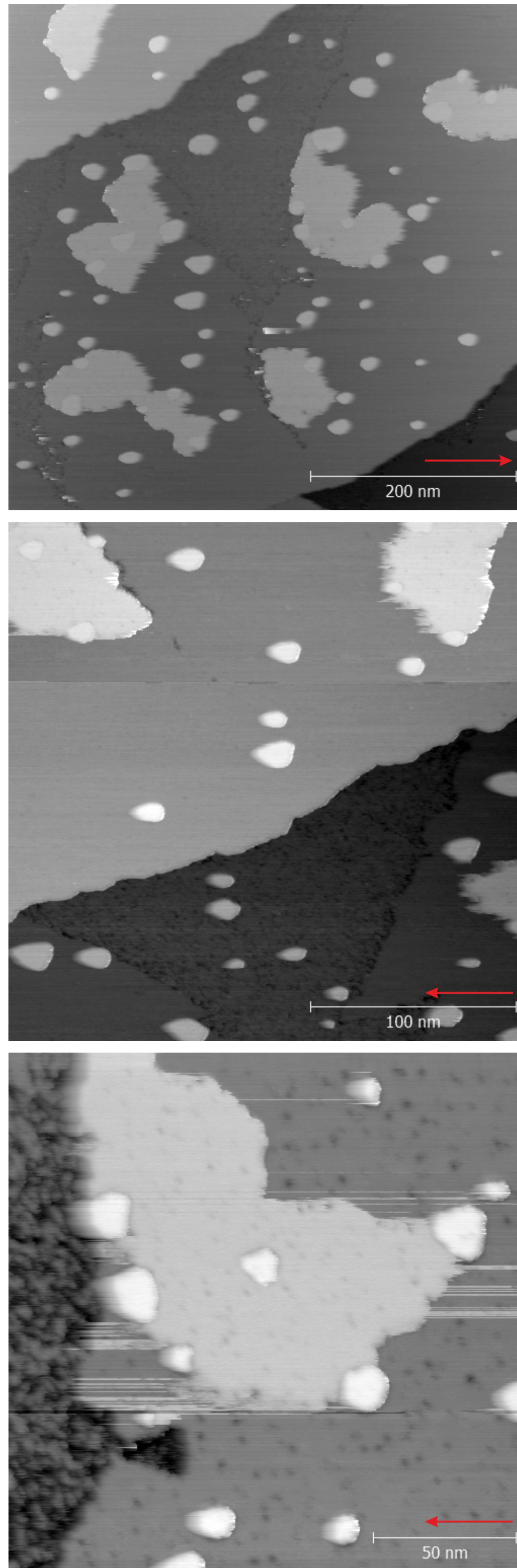

Figure 6.19: Si(111)/Tl-(1×1)/In: two images on the top were taken at tip bias +2 V and tunneling current 0.3 nA, the image on the bottom was taken at tip bias 0.2 V and tunneling current 0.2 nA; red arrows show the scanning direction.

6.3.3 In on Si(111) after the desorption of Tl

After the Si(111)/Tl-(1×1)/In observation, we executed desorption of Tl by annealing of the sample at temperature $\approx 400°C$ for 5 minutes. The figure 6.20 shows a big area of the surface from which can be concluded that the surface was reconstructed very homogeneously.

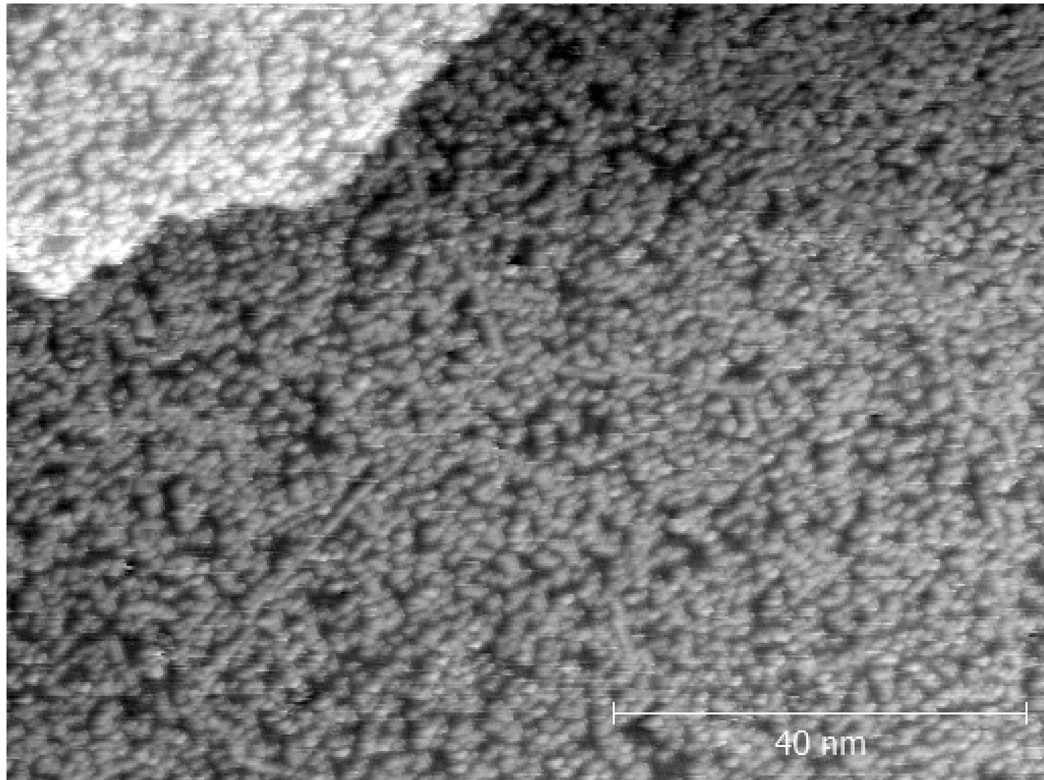

Figure 6.20: The large area of Si(111)/In after desorption of thallium.

A detailed look at the surface (figures 6.21 6.22) reveals that the periodicity of reconstruction on the surface is $(\sqrt{3} \times \sqrt{3})$. In and Si atoms occupy possitions in the lattice. A recognition of atoms was achieved the same way as in the case of Si(111)-In. It led us to a conclusion that In atoms on the figure 6.22 appear brighter, while Si atoms appear darker. The $(\sqrt{3} \times \sqrt{3})$ reconstruction was present on all observed parts of the surface except small unreconstructed areas and domain boundaries. In comparison with the surface prepared by direct deposition of In, no areas with the reconstruction (7×7) were observed.

Figure 6.21: Si(111)/In-$(\sqrt{3} \times \sqrt{3})$; tip bias: -0.5 V, tunneling current: 0.3 nA.

The figure 6.21 reveals an interesting feature of the surface Si(111)/In-$(\sqrt{3} \times \sqrt{3})$. While on the figure 6.22 only two easily distinguishable shades of grey are present

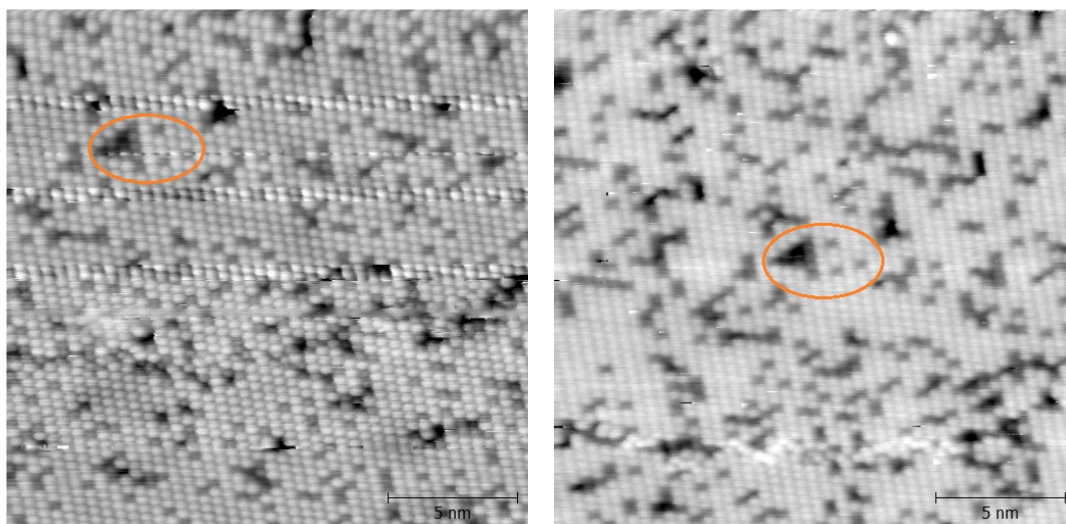

Figure 6.22: Si(111)/In-($\sqrt{3} \times \sqrt{3}$): the same area of the surface taken at two tip biases; left: tip bias -1 V, tunneling current 0.3 nA , right: tip bias -1.5 V, tunneling current 0.3 nA; the orange elipse marks the same configuration of the surface substituted atoms and defects, which indicates the same area of the surface.

on the images at both polarities, many shades are visible at the tip bias -0.5 V. We suggest that the phenomenon is caused by the charge redistribution between Si and In surface atoms. The hypothesis is supported by the fact, that the brightness (darkness) of atoms is stronger in the cases of atoms which have more neighbours of the same type (the redistribution is smaller).

6.3.4 Indium: summary

As was expected on the basis of the the phase diagram and other results of previous researchers, we observed surface almost completely covered by the root-three reconstruction of In with substitutional Si atoms after direct deposition of In. Small areas covered by the (7×7) reconstruction with substitutional In atoms were observed too.

After desorption of Tl from underneath deposited In, the root-three mosaic phase covers the whole surface homogeneously. No other reconstruction was observed, which suggests that Tl passivation successfully cancels the underlying (7×7) reconstruction and thus enables growth of energetically favourable reconstructions at lower temperature (similarly to the case of Al).

An interesting feature of the obtained images of Si(111)/Tl-(1×1)/In is the apparent interaction of the STM tip with the adsorbate. The interaction is visible as a ragged edge of islands in direction of scanning of the STM. The feature is the evidence of extremely high mobility of adsorbate on the surface, which results in the change of the shape of islands at the speed which is comparable to the scanning speed of the STM. Amount of In which is unseen by the STM thanks to high diffusivity of In was estimated to be approximately 0.05 ML.

6.4 Tin

6.4.1 Sn on Si(111)-(7×7)

The last element which was studied in this work is tin. Thanks to its placement in the periodic table of elements, it should have properties similar to the silicon (same group: IV.A) and indium (same period: 5 and similar atomic radius: 145 pm). These facts drove our interest toward the closer examination of the tin interaction with the passivated surface and its comparison with other adsorbates.

The phase diagram of Sn on Si(111) can be seen on the figure 6.23, which is the result of experiments of Ichikawa et al. [55]. The area of the diagram is predominantly occupied by the $(\sqrt{3} \times \sqrt{3})$ reconstruction, which is present on the surface at coverage above 0.1 ML and temperature below ≈ 860°C. At coverage below 0.2 ML, the (7×7) phase can be also found on the surface. Under ≈ 190°C and above 0.3 ML, the $(2\sqrt{3} \times 2\sqrt{3})$ reconstruction covers the surface as well. Many works that study individual phases observed on Si(111)/Sn can be found [56, 27, 57, 58] (mostly studies of $(\sqrt{3} \times \sqrt{3})$ and $(2\sqrt{3} \times 2\sqrt{3})$ reconstructions).

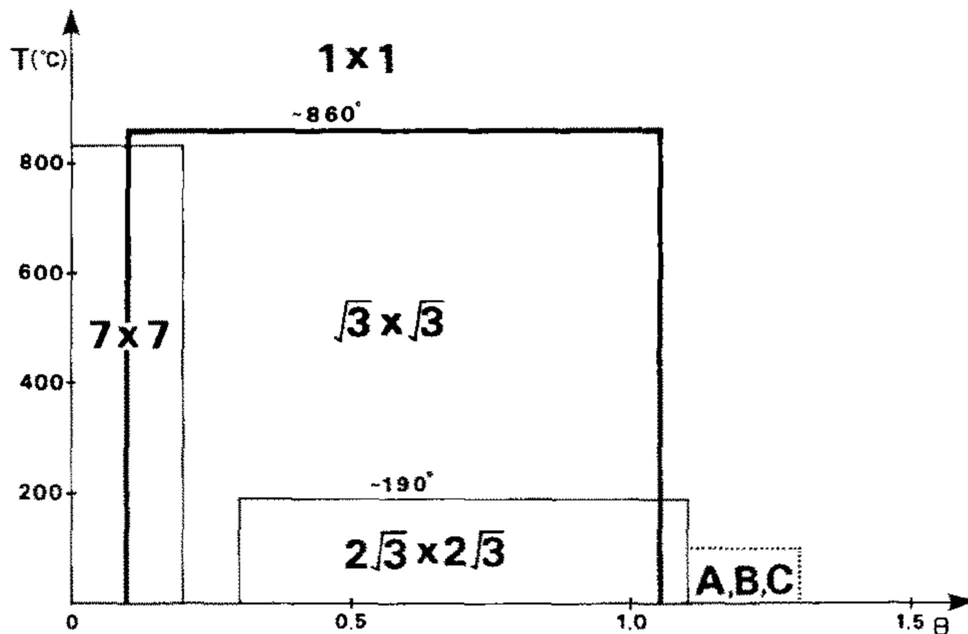

Figure 6.23: Phase diagram of Si(111)/Sn [55]; A,B,C - three types of superstructures observed on the surface according to [55].

According to the voltage dependent images obtained by Tornevik et al. [27], Sn atoms appear as bright protrusions at positive tip bias. For negative tip bias, the STM images vary considerably. In the range of voltage between -1 V to -1.5 V, Si and Sn adatoms appear to be almost identical and are hard to distinguish. At higher negative biases, Sn adatoms begin to appear brighter again.

Our experiments on Si(111) with directly deposited Sn show analogous results as above mentioned results of other groups. After deposition of approximately 0.2 ML of Sn and subsequent annealing at ≈ 400°C, we observed large areas covered by the (7×7) reconstruction, beside areas which transformed into the

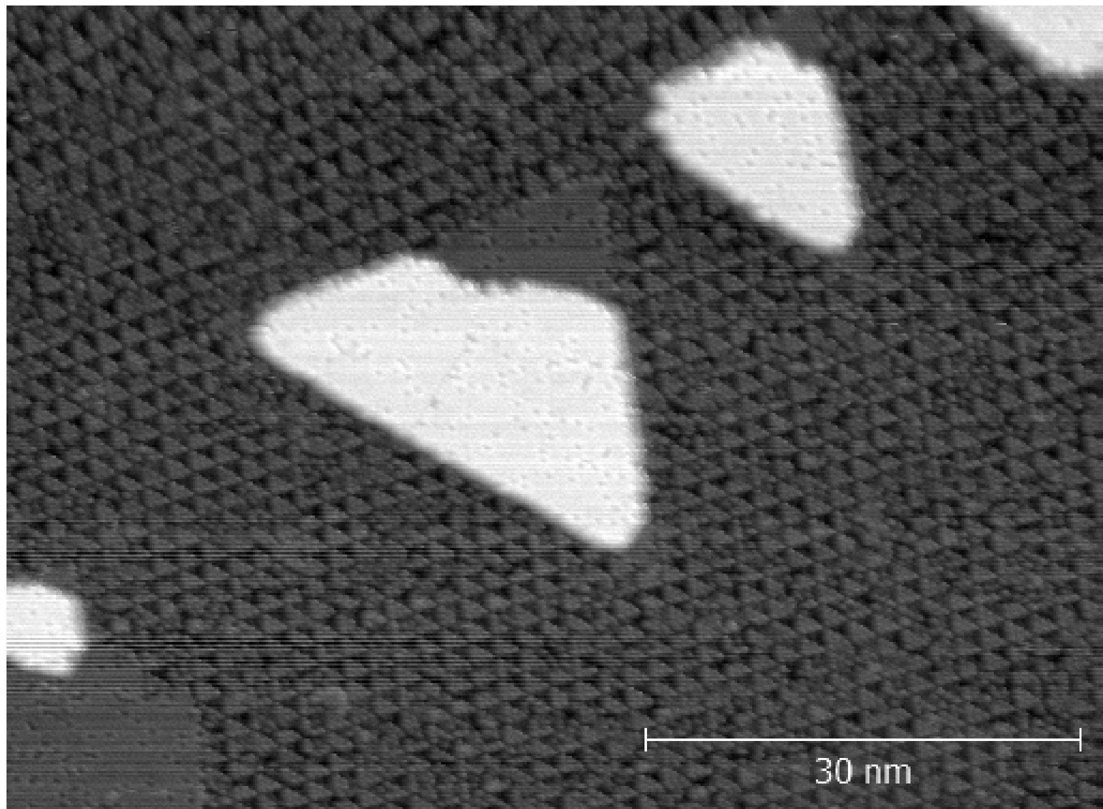

Figure 6.24: Image of the surface Si(111)/Sn taken at high positive tip bias: +1.5 V, tunneling current: 0.25 nA.

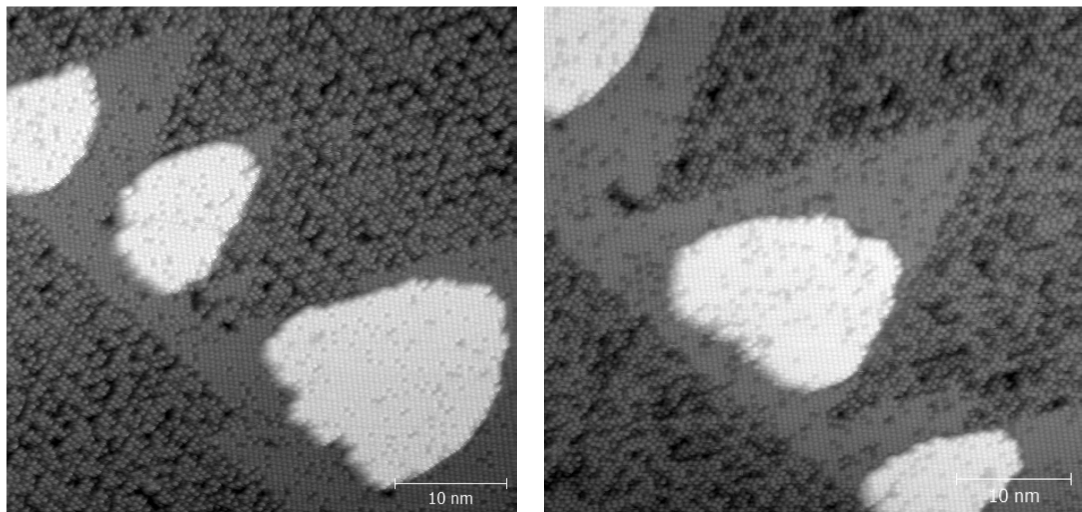

Figure 6.25: The image of a similar area of the surface taken at low positive (0.4 V - left) and low negative (-0.25 V - right) tip bias; tunneling current: 0.4 nA.

root-three phase (see the figure 6.24). Both areas exhibit a tendency to acquire triangular shape. The triangular (7×7) areas have preferably same orientation as faulted HUCs, while root-three areas prefer to have orientation of unfaulted HUC. As a reader can see from the figures 6.24 and 6.25 (left), Sn adatoms (appear brighter on the figures) occupy almost exclusively only one type of HUC. On the basis of the comparison with the clean surface, we determined that preferably occupied HUC is faulted one.

The root-three structure occupies areas with the opposite (unfaulted) orientation. The reconstruction consists predominantly of Sn atoms. A portion of Si atoms that substitute Sn in the lattice was determined to be $(8 \pm 2)\%$. Very interesting fact about the root-three structure on the surface is that it creates the second layer of the root-three reconstruction on the top of already reconstructed triangular areas even before the completion of the first layer. The reconstruction on islands has the same percentage of Si substitutional atoms and the same orientation of main lattice directions as the surrounding $(\sqrt{3} \times \sqrt{3})$ (the growth is epitaxial). The height of islands was calibrated according to the Si step height as can be seen on the figure 6.26. The figure shows that the heigth of islands and Si billayer steps are matching.

The coverage by different phases was measured as follows: $\Theta_{(7\times7)} = (0.70 \pm 0.07)$, $\Theta_{(\sqrt{3}\times\sqrt{3})} = (0.25 \pm 0.03)$; $\Theta_{\mathrm{I}}(0.05 \pm 0.01)$. Unreconstructed parts of the surface were present also. They covered approximately 10% of the surface. Since we did not know how exactly the unreconstructed areas behave in relation to adsorbed Sn atoms, we assumed that approximately same ammount of Sn is bonded on these areas as on average of the rest of the surface after deposition of Sn. We also assumed that approximately same amount of Si is bounded and released from this area as from the rest of the surface. This asumption enables us to exclude the unreconstructed areas from the statictics. The mass analysis for the top layer of silicon was calculated as follows.

$$R_{(7\times7)} = S_{(7\times7)}\Theta_{(7\times7)} \tag{6.1}$$

$$R_{(\sqrt{3}\times\sqrt{3})} = \Theta_{(\sqrt{3}\times\sqrt{3})}\left(\Omega_{(7\times7)} - \Omega_B - \frac{49}{3}S_{(\sqrt{3}\times\sqrt{3})}\right) \tag{6.2}$$

$$R_{island} = \Theta_{island}\left(\Omega_{(7\times7)} - 2\Omega_B - \frac{49}{3}S_{(\sqrt{3}\times\sqrt{3})}\right) \tag{6.3}$$

where R_X is the number of released silicon atoms from the fraction of (7×7) unit cell area which corresponds to the phase "X", Θ_X is the coverage of the surface by the phase "X", $S_{(7\times7)}$ is the number of Si adatoms which are substituted by Sn per one (7×7) unit cell, $S_{(\sqrt{3}\times\sqrt{3})}$ is the ratio of substitution of Sn atoms by Si in the $(\sqrt{3} \times \sqrt{3})$ phase, $\Omega_{(7\times7)}$ is the number of Si atoms in one (7×7) unit cell of the top silicon layer with the non-bulk arragement and Ω_B is number of Si in one (7×7) unit cell of the silicon billiayer with the bulk arrangement. On the basis of our observations we calculated with the values: $S_{(\sqrt{3}\times\sqrt{3})} = (0.08 \pm 0.02)$ and $S_{(7\times7)} = 6$. After the substitution:

$$R_{Si-(7\times7)} = 6 \times 0.7 = 4.2 \tag{6.4}$$

$$R_{Si-(\sqrt{3}\times\sqrt{3})} = 0.25 \times (102 - 98 - \frac{49}{3} \times 0.08) \doteq 0.67 \tag{6.5}$$

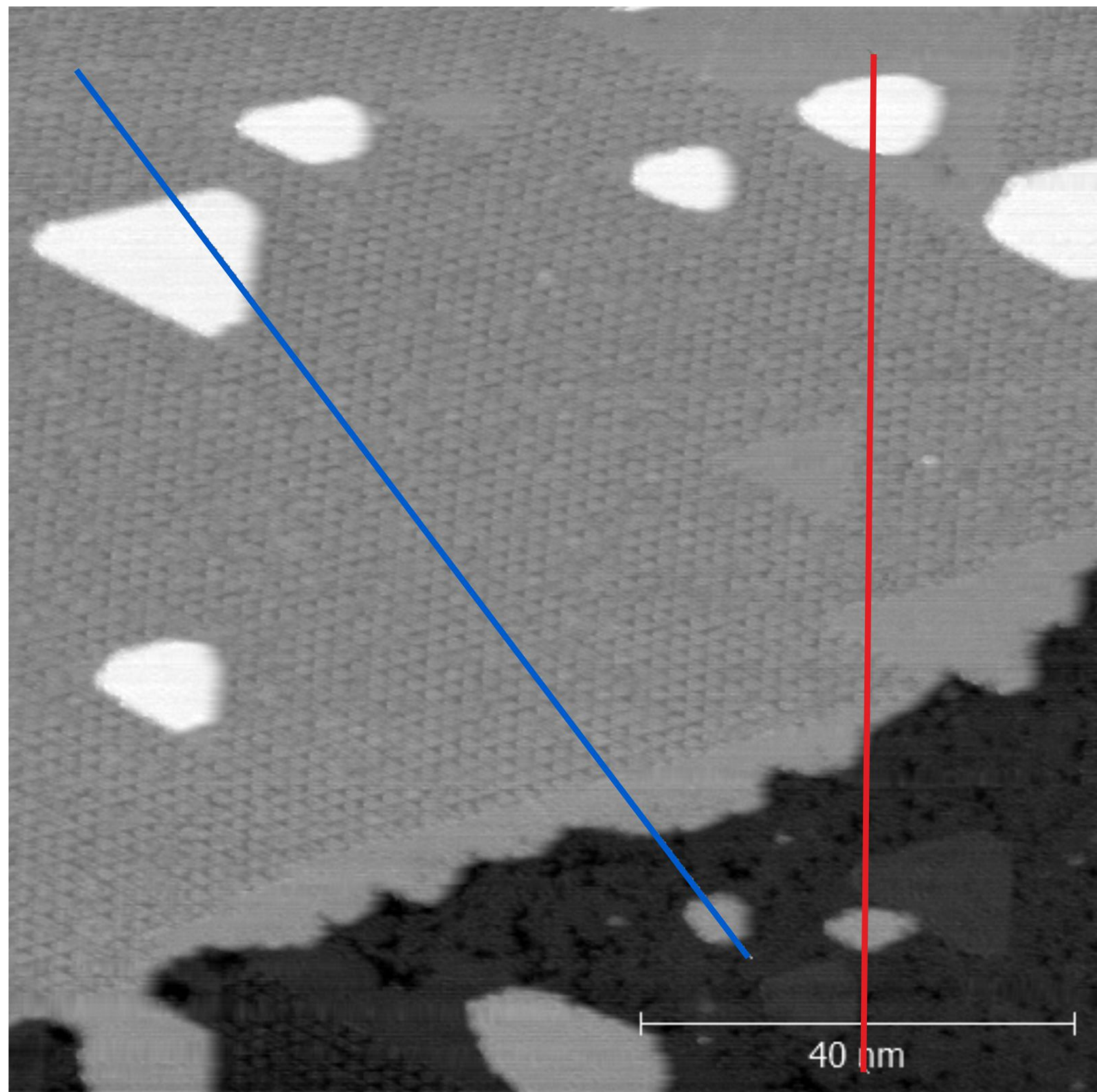

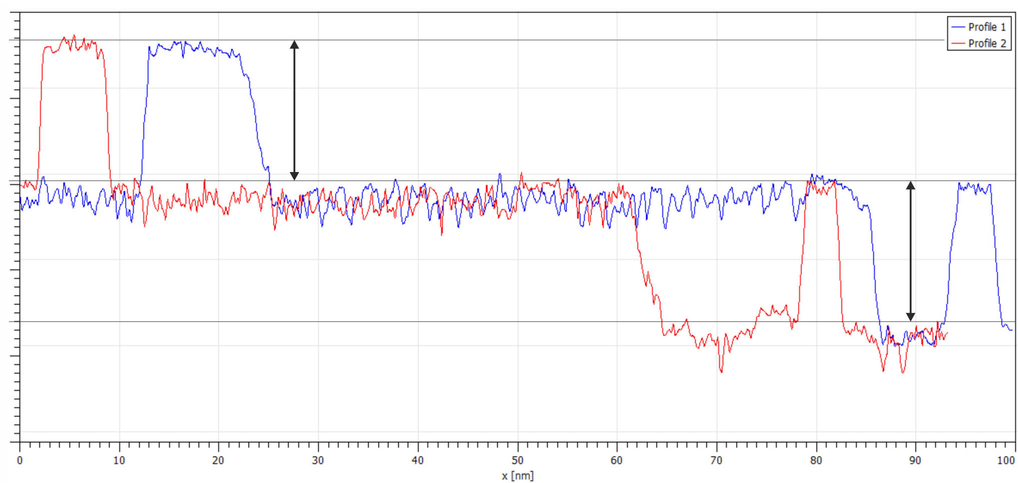

Figure 6.26: The calibration of Sn islands height according to the Si step height: double-arrows indicate the height of Si step and triangular islands. The blue line and the red line on the top image indicate lines used for the profiles one and two from the graph below. The length unit on the vertical axis of the graph is arbitrary.

$$R_{island} = 0.05 \times (102 - 2 \times 98 - \frac{49}{3} \times 0.08) \doteq -4.77 \quad (6.6)$$

Therefore, overall on an averege (7×7) unit cell, (4.87 ± 0.49) Si atoms are released and (4.77 ± 0.48) Si atoms are consumed by the creation of islands. The mass analysis for Sn was calculated as follows:

$$\theta_{Sn} = \frac{\Theta_{(7\times7)} S_{(7\times7)}}{49} + \frac{(1 - S_{(\sqrt{3}\times\sqrt{3})})(\Theta_{(\sqrt{3}\times\sqrt{3})} + \Theta_{island})}{3} \quad (6.7)$$

where θ_{Sn} is the coverage of Sn atoms in ML. After the substitution:

$$\theta_{Sn} = \frac{0.7 \times 6}{49} + \frac{(1 - 0.08)(0.25 + 0.05)}{3} \doteq 0.18ML \quad (6.8)$$

The calculated value of the Sn coverage ((0.18 ± 0.02) ML) is within the error range in accordance with expected value 0.2 ML based on the deposited amount of Sn. The error of the measurement was estimated on the basis of the unknown errors of assumptions at the beginning of the calculations (the estimation of $S_{(7\times7)}$, unknown effect of unreconstructed areas).The mass analyses of Si and Sn support the theory of the bilayer nature of islands.

Detailed images of the island structure (see figure 6.27) reveal that in comparison with the first layer of the root-three reconstruction, the structure of the second layer is single domain. Figure 6.27-bottom shows two areas on the first layer where the domain boundary is located (marked by orange ellipses). No domain boundaries were observed on the second layer. A direct implication is that there are areas of islands whose lattices match the underlying lattices, next to areas where lattices are shifted. An example can be found on the figure 6.27-bottom, where the black lines indicate the lattice match of the first and the second layer. Green and red lines indicate the local lattices of the first and the second layer respectively. It is apparent that two lattices are shifted and do not match each other at boundaries of domains.

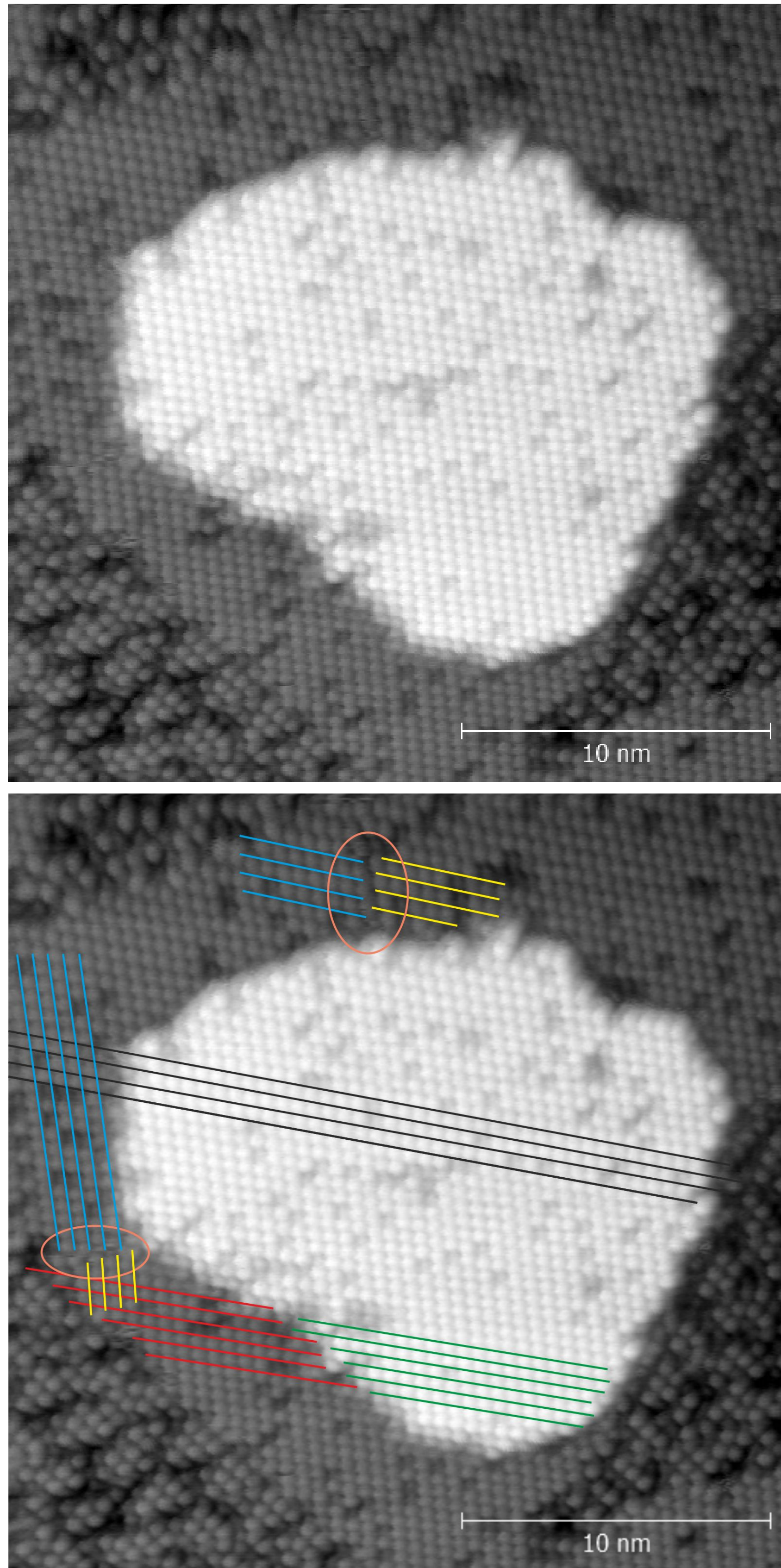

Figure 6.27: The atomically resolved detailed image of the Sn island at low positive tip bias +0.2 V; tunneling current: 0.4 nA (top); the same image with highlighting of local lattices of the root-three phase (bottom).

6.4.2 Sn on Si(111)/ Tl-(1×1)

Tin has fundamentally different behaviour on the passivated surface Si(111)/Tl in comparison with the above described elements (Mn, Al, In). All three elements exhibited high diffusivity on the surface and have an extremely weak bond with underlying silicon. Therefore, islands observed at surfaces with those three elements had more or less unpredictable shape in relation to the substrate. In the case of Sn, the opposite is true. We observed the evenly spread array of triangularly shaped islands as it can be seen on the figure 6.28. Triangular islands cover $(23 \pm 3)\%$ of the surface. Since the amount of deposited material was same within the error range (0.2 ML), we concluded that the concentration of Sn in these islands is 1 ML. Islands tend to inclose Si-step islands and step edges of terraces, otherwise there was no preference of positioning of islands observed.

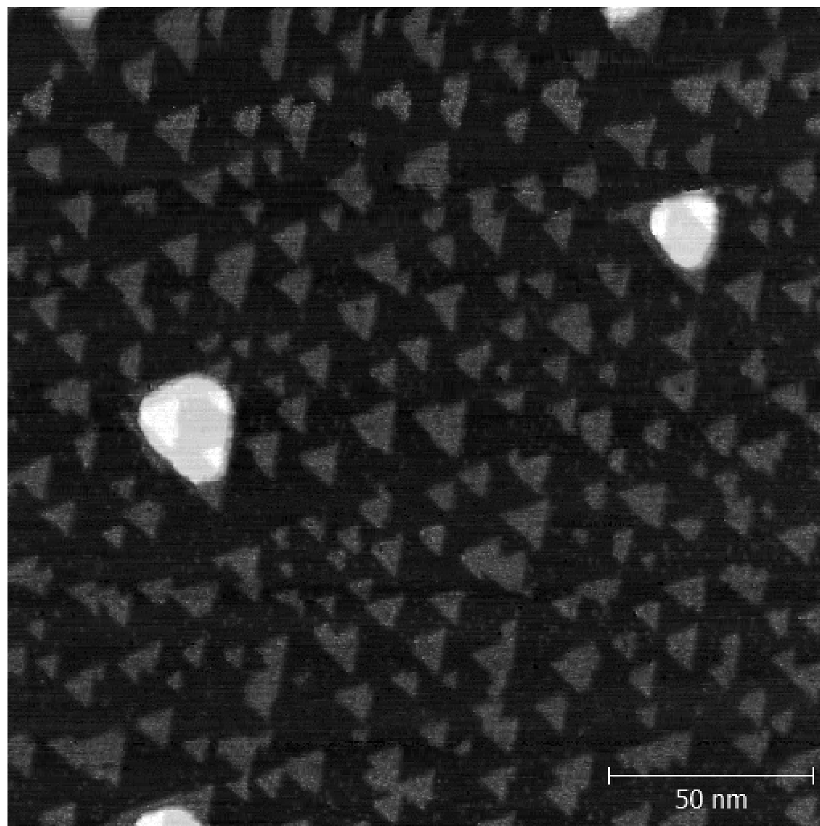

Figure 6.28: Overall look at the surface Si(111)/Tl-(1×1)/Sn; tip bias: -1.87 V, tunneling current: 0.3 nA.

Figure 6.29 shows imaging of islands in both polarities. Inverse contrast is apparent. Closer look at the structure of islands is shown on the figure 6.30. Islands were stable during the whole measurement and no change in their shape or structure was observed. Orientation of triangles is almost exclusively same as the orientation of unfaulted HUCs of underlying silicon. On the basis of gathered data, we were not able to resolve an atomic structure of islands, therefore we can not describe the exact way of bonding to silicon substrate. Based on the similar appearance of the structure and Moire patterns, which are often observed

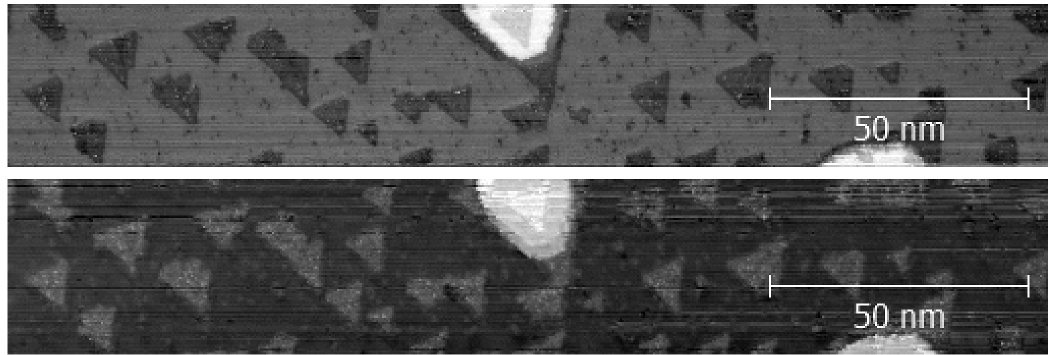

Figure 6.29: The same area of the surface Tl-(1 × 1)/Sn taken at opposite tip biases (top: +1 V, bottom: -1 V); tunneling current: 0.3 nA.

on thallium-passivated surfaces, we propose that islands could be Moire patterns created by an interaction between Sn and Tl-(1 × 1) layer (but we have no sufficient experimental data to support or disprove this theory). To the best of our knowledge, there were no similar objects observed on the Si(111)/Tl-(1 × 1) surface so far, therefore the resolution of the structure will be one of the topics of our future research.

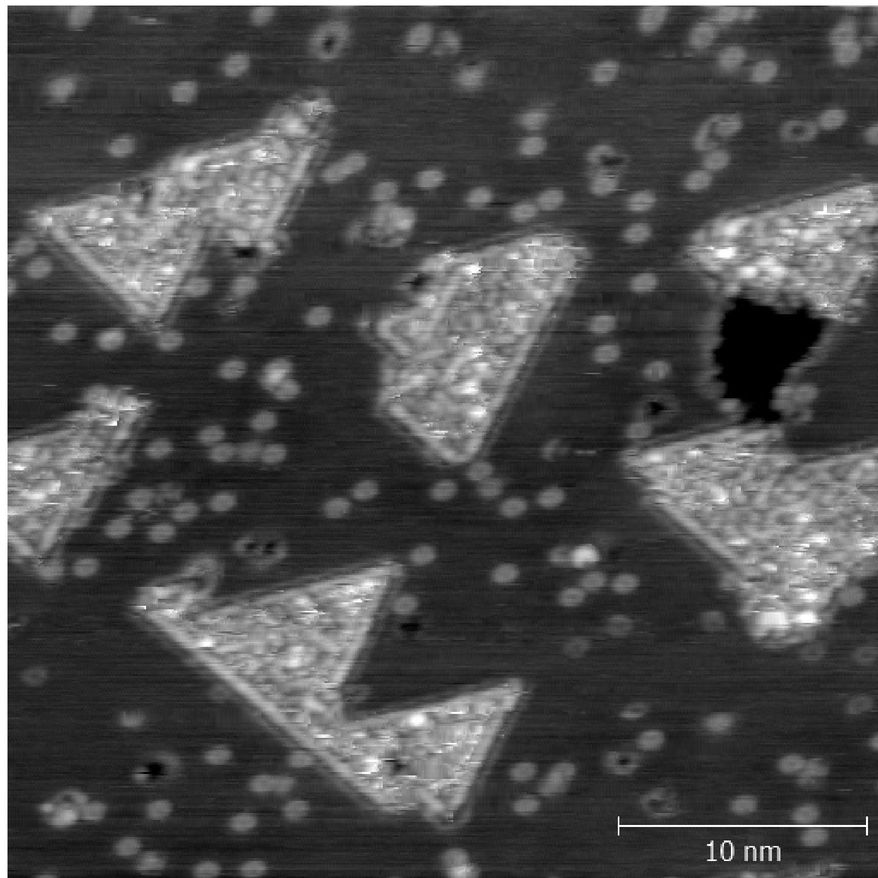

Figure 6.30: The detail of the surface Si(111)/Tl-(1 × 1)/Sn; tip bias: -2.3 V, tunneling current: 0.17 nA.

6.4.3 Sn on Si(111) after desorption of Tl

After annealing of the sample at $\approx$ 400°C for 5 minutes and desorption of thallium, surface changed its character drastically in comparison with the direct deposition of Sn. First of all, we did not observe any areas covered by the residual (7×7) reconstruction. The whole surface was stabilized in the root-three mosaic reconstruction with $(66 \pm 4)\%$ of Sn atoms (see figures 6.31 and 6.32). The passivating Tl layer cancelled the original (7×7) reconstruction and after annealing at $\approx 400°C$, Sn created its own surface arrangement without the necessity of cancellation of the (7×7). Therefore, almost a homogeneous arrangement was created over the whole surface. Occasional domain boundaries and other defects can be found on the topmost layer (see figure 6.32).

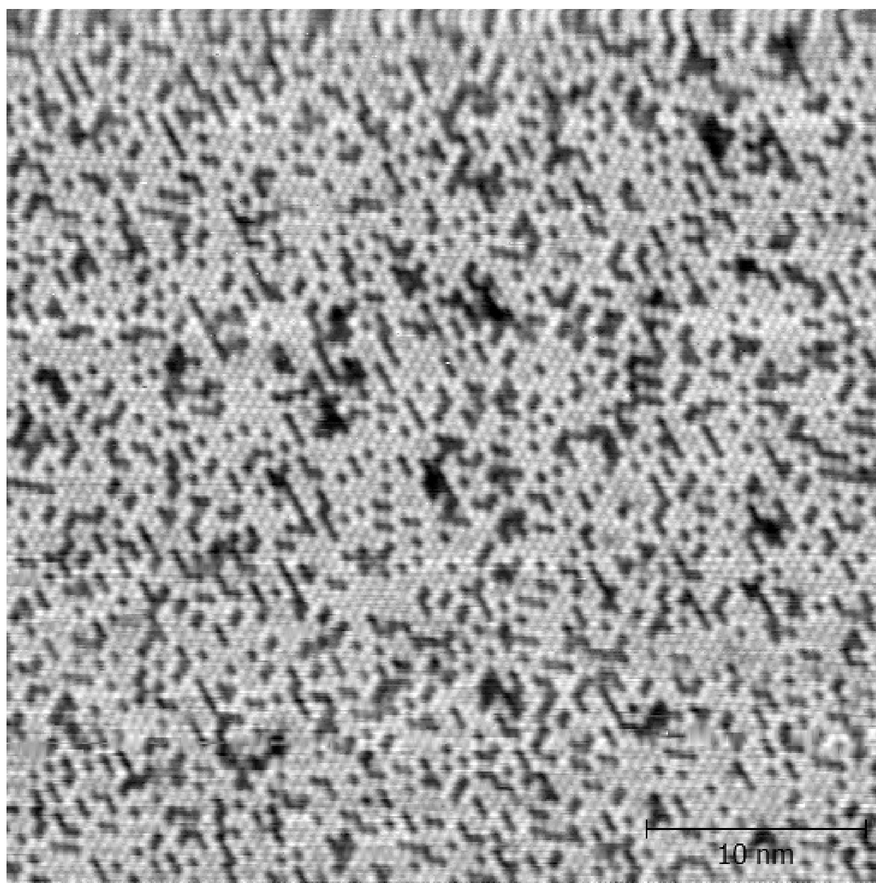

Figure 6.31: Typical image of the surface Si(111)/Tl-(1×1)/Sn after desorption of Tl; tip bias: +0.6 V, tunelling current: 0.4 nA; Sn: bright, Si: dark.

Similarly to indium and aluminium, the charge transfer between Sn and substitutional Si atoms was observed. The effect is the most apparent at negative tip biases, especially at -1.5 V tip bias (see figure 6.32). Different shades of gray, corresponding to the number of neighbors of the same kind are clearly visible (images taken at different polarities can be compared since the displayed area is the same for the whole series of pictures on the figure 6.32).

The statistical processing of measured data was also executed. Ottaviano et al. in their work published Monte Carlo simulations of Si mosaic $(\sqrt{3} \times \sqrt{3})$

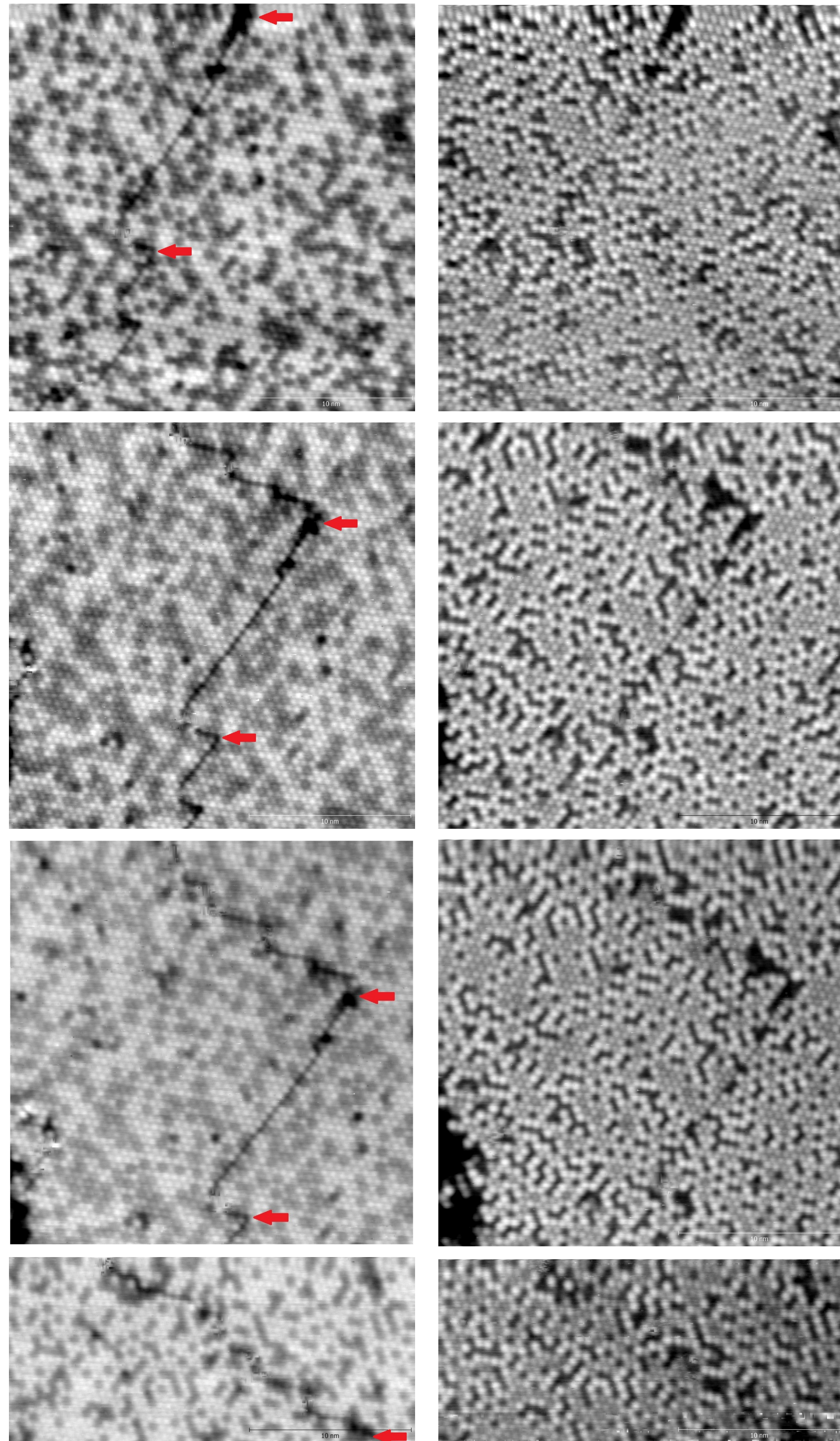

Figure 6.32: The same area of the surface taken at muplitple voltages in both polarities: left collumn - negative tip biases; right collumn - positive tip biases (±0.9 V, ±1.5 V, ±1.8 V, ±2.3 V), tunneling current: 0.35 nA; the horizontal size of images is 25 nm; two outstanding features are marked on the images for the better orientation between images taken at different voltage.

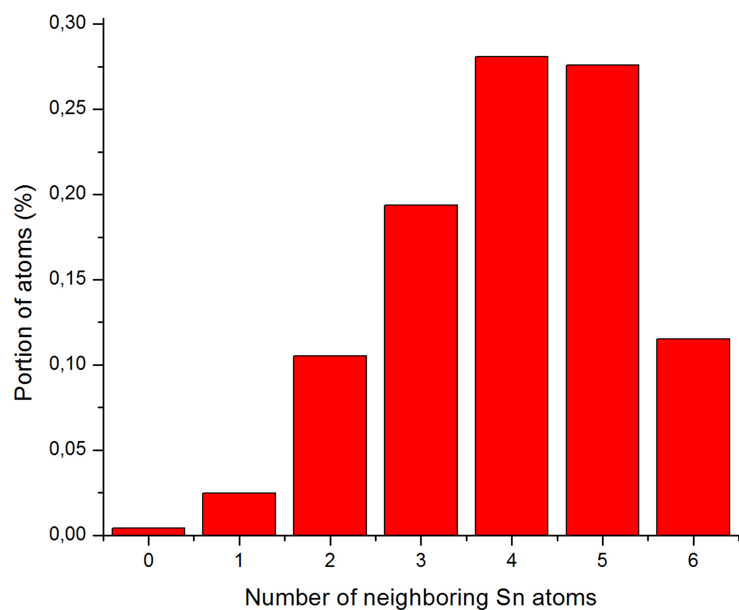

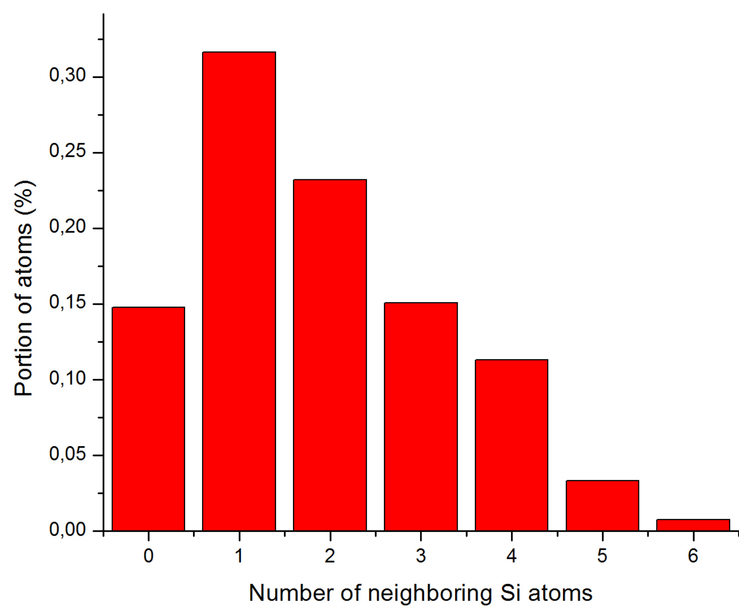

Figure 6.33: The distributions of surface atoms according to the number of neighboring atoms of the same type.

reconstructions with various ratios of Sn and Si substitutional atoms [59]. Their results show that in the completely relaxed state of the phase at the ratio of substitution 1:2 (33% of Sn substituted by Si), silicon atoms almost do not have other Si atoms as neighbours. The vast majority of Si is therefore surrounded only by Sn atoms. This behaviour is caused by the repulsive interaction of Si substituted atoms. In oreder to find out how relaxed our root-three mosaic was, we executed the statistic processing which results can be seen on the figure 6.33. In our case the majority of Si atoms has one neighbouring Si atom. The surface is therefore not in its fully relaxed state. The comparison with the case of directly deposited Sn was not done since the mosaic root-three phase with a different ratio between Si and Sn was observed.

6.4.4 Tin: summary

After a direct deposition of approximately 0.2 ML of Sn onto the clear Si(111)-(7×7) surface, two phases were observed. The (7×7) phase covered (70±7)%. On average, it has approximately 6 Si adatoms substituted by Sn mostly in faulted HUCs. The $(\sqrt{3} \times \sqrt{3})$ reconstruction with $(8 \pm 2)\%$ of Sn substituted by Si covered $(25 \pm 3)\%$ of the surface. Root-three Si-step islands covered $(5 \pm 1)\%$ of the surface. The nature of islands was confirmed by the height profiles of islands, which show that their height is same as the height of the Si step. The mass analysis of the surface showed that (4.87 ± 0.49) Si atoms are released due to the phase transformation from the area of a (7×7) unit cell. The formation of Si-step islands at the observed coverage would need (4.77 ± 0.48) Si atoms. The two numbers are within the error range in good agreement, which supports our theory that the island's root-three reconstruction lays on the top of the bilayer of Si.

On the other hand, the surface after the thallium mediated growth is more homogeneous. Only the mosaic reconstruction $(\sqrt{3} \times \sqrt{3})$ with $(66 \pm 4)\%$ of Sn was present on the surface. The charge transfer between Si and Sn atoms was observed. On the basis of the statistical processing of acquired data, we concluded that the mosaic structure is not completely relaxed.

Sn on the Tl passivated Si(111) surface arranges into an array of triangular islands evenly spread across the surface. The orientation of islands is same as the orientation of unfaulted HUCs of the clean Si(111)-(7×7) surface. Coverage by islands was measured to be $(23 \pm 3)\%$ therefore the density of Sn within islands was determined to be the same as the density of (1×1) structure. The resolution of the island's structure is the goal of following research.

Chapter 7

Conclusions

Since the motivation of our work was the investigation of Si(111) passivation by thallium, we executed experiments and statistical processing of measured data leading to the better understanding of the passivation process.

We studied the morphology of the Tl-(1×1) passivation layer by means of the STM. The main observed feature of the layer was the presence of Si-bilayer islands, which acted as nucleation centers after deposition of adsorbate. At room temperature, the layer was stable even after deposition of highly reactive adsorbates (Mn). Thermal desorption experiments showed that desorption begins at $\approx 300°$C (2 minutes annealing). The desorption of Tl continues until reaching $\approx 400°$C, when thallium is completely removed from the surface. Throughout the desorption, thallium induces the surface transformation from the (1×1) phase through the mosaic reconstruction $(\sqrt{3} \times \sqrt{3})$ to the metastable reconstructions of Si(111) with Si substituted by Tl. Fitting of the measured dependence of Tl coverage on temperature showed that the valence of Tl in the (1×1) reconstruction is same as in the $(\sqrt{3} \times \sqrt{3})$ reconstruction.

Behaviour of manganese, aluminium, indium and tin on the Tl passivation layer was studied closely in order to investigate the possibility of thallium acting as a passivator of the Si(111) surface. The most pronounced attribute of adsorbate's behaviour was its extreme diffusivity, which caused an existence of most observed surface features such as dendritic Mn islands, floating In islands with ragged edges, missing deposited Al atoms etc. As an exception of mentioned examples, the array of stable epitaxial triangular islands with unknown structure and way of bonding to the silicon substrate was present on the surface Si(111)/Tl/Sn.

The possibility of usage of Tl in the thallium mediated growth for each studied element was examined as well. Adsorbates were directly deposited onto the Si(111)-(7×7) and were compared with the layers prepared by deposition of adsorbate onto the passivating layer after the subsequent thermal desorption of Tl (after annealing at $\approx 400°$C for 5 minutes). Comparison showed that in all observed cases thermally induced structures grow at lower temperatures and lower coverages than in the case of direct deposition. For instance, we were able to grow Mn nanowires at temperature $\approx 130°$C lower than the temperature of preparation reported in earlier studies and grow reconstructions of studied adsorbates at temperature and coverage lower than it was expected on the basis of the phase diagrams of directly deposited adsorbates.

As it has been shown in this work, the surfactant mediated growth of thin films is a powerful tool of surface science, which brings new possibilities of the modification of films growth. Overall, it can be said that the possibility of the usage of thallium as a surfactant was confirmed for various adsorbates. Thallium on Si(111) is therefore a promising element for the further future research.

Bibliography

[1] BINNING, G., et al. (7×7) reconstruction on Si(111) resolved in real space. Physical Review Letters. 1983, 50, p. 2.

[2] YE-LIANG, W., et al. Toward a Detailed Understanding of Si(111)-(7×7) Surface and Adsorbed Ge Nanostructures: Fabrications, Structures and Calculations. Journal of Nanomaterials. 2008, doi:10.1155/2008/874213

[3] CHANG, T.-CH., et al. Nucleation and growth of Si on Pb monolayer covered Si(111) surfaces. Surface Science. 2011, 605, 1249-1256

[4] VITALI, L., et al. Rotational epitaxy of a 'soft' metal overlayer on Si(111). Surface Science. 2000, 452, p.281-286

[5] VITALI, L., et al. Thallium overlayers on Si(111): Structures of a "new" group III element. Journal of Vacuum Science and Technology A. 1999, 17, p.1676-1682

[6] SAKAMOTO, K., et al. Abrupt rotation of the Rashba spin to the direction perpendicular to the surface. Physical Review Letters. 2009, 102, 096805

[7] BINNIG, G., et al. Surface studies by scanning tunneling microscopy. Physical Review Letters. 1982, 49, p. 57-61.

[8] BINNING, G., et al. Atomic Force Microscope. Physical Review Letters. 56, p. 930-934

[9] GROSS, A. Theoretical Surface Science: A Microscopic Perspective. Springer. 2009

[10] TERSOFF, J., HARMANN, D.R., Theory and application for the scanning tunneling microscope. Physical Review Letters. 1983, 50, n.1998

[11] Http://hoffman.physics.harvard.edu [online]. 2010 [cit. 2013-03-02]. STM: more technical details. availiable at www: http://hoffman.physics.harvard.edu/research/STMtechnical.php

[12] BARDEEN, J. Tunnelling from a many-particle point of view. Physical Review Letters. 1961, 6, p.57

[13] HOFER, W.A., et al. Theories of scanning probe microscopes at the atomic scale. Rev. Mod. Phys. 2003, 75, p.1287

[14] MATVIJA, P., Studium interakce atomu kovu s metastabilními rekonstrukcemi povrchu Si(111) pomocí STM. Prague, 2011. 53p., Thesis. Charles University in Prague

[15] KOCÁN, Pavel. Study of Heteroepitaxial Growth on Reconstructed Si Surfaces. Univerzita Karlova v Praze, Praha, 2004. 112 p.

[16] WINGERDEN, J., et al. Atomic details of step flow growth on Si(001). Physical Review B. 1997, 55, p.9352-9355

[17] VENABLES, J.A. Introduction to Surface and Thin Film Processes. Cambridge University Press. 2000

[18] LENNARD-JONES, J.E. On the Determination of Molecular Fields. Proc. R. Soc. Lond. 1924, 106, p. 463-477

[19] SHIRAIWA, M., et al. The role of long-lived reactive oxygen intermediates in the reaction of ozone with aerosol particles. Nature Chemistry. 2011, 3, p.291-295

[20] http://www.chemicool.com [online]. 2013 [cit. 2013-03-28]. Silicon Element Facts. availiable at www: http://www.chemicool.com/elements/silicon.html

[21] JEONG, H., JEONG, S., Diffusion of Ag on the H-terminated and clean Si(111) surface: A first-principle study. Physical Review B. 2005, 71, 0353101

[22] AZPIROZ-I., J. Relativistic effects and fully spin-polarized Fermi surface at the Tl/Si(111) surface. Physical Review B. 84, 2011, p. 125435:1-6

[23] SAKAMOTO, Y., et al. The (1×1) high temperature phase of Ge(111) and Si(111). Surface Science. 1991, 242, p.119-123

[24] NICHOLLS, JM., et al. Unoccupied surface states revealing the Si(111)-$(\sqrt{3} \times \sqrt{3})$-Al, Si(111)-$(\sqrt{3} \times \sqrt{3})$-Ga and Si(111)-$(\sqrt{3} \times \sqrt{3})$-In adatom geometries. Physical Review B. 1987, 35, p.4137-4140

[25] TAKAOKA, K., et al. Al-$(\sqrt{3} \times \sqrt{3})$ domain structure on Si(111)-(7×7) observed by scanning tunneling microscopy. Physical Review B. 1993, 48, p.5657-5660

[26] KRAFT, J., et al. Surface reconstructions of In on Si(111). Physical Review B. 1996, 55, p.5384-5393

[27] TORNEVIK, C., et al. Adsorption of Sn on Si(111)-(7×7) reconstructions on the monolayer regime. Surface Science. 1994, 314, p.179-187

[28] KOCAN, P., et al. An STM study of desorption-induced thallium structures on the Si(111) surface. Surface Science. 2012, 606, p.991-995

[29] HIBINO, H., et al. Exchanges between group-III (B, Al, Ga, In) and Si atoms on Si(111)-$\sqrt{3} \times \sqrt{3}$ surfaces. Physical Review B. 1996, 54, p.5763-5768

[30] OZKAYA, M., et al. Atomic and electronic structures of Tl/Si(111)-$(\sqrt{3} \times \sqrt{3})$. Surface Science. 2008, 602, 1376

[31] BECKER, R.S., et al. Real-space observation of surface states on Si(111)-(7×7) with tunneling microscope. Physical Review Letters. 1985, 55, p.9

[32] Http://geocities.yahoo.co.jp/ [online]. 1996 [cit. 2011-03-21]. Makoto Itoh's homepage. availiable at www: http://www.geocities.jp/mitoh6/index.html.

[33] STEIGERWALD, I.J., et al. Structural study of the epitaxial-growth of FCC-FE films, sandwiches, and superlattices on Cu(100). Surface Science, 1988, 202, p.472

[34] SOBOTIK, P., et al. Reconstruction-determined diffusion of Ag adatoms on the Si(111)-(7×7) surface. Czechoslovak Journal of Physics. 2003, 53, p.69-74

[35] VOIGTLANDER, B., et al. Influence of surfactants on the growth-kinetics of Si on Si(111). Surface Science. 1993, 292, p.L775-L780

[36] ZOTOV, A.V., et al. Diverse magic nanoclustering in submonolayer Tl/Si(111) system. Surface Science. 2006, 600, p.1936-1941

[37] KUMAR, A., et al. Thin manganese films on Si(111)-(7×7): electronic structure and strain in silicide formation. Journal of Physics D: Applied physics. 2004, 37, p.1083-1090

[38] SIVAPRASAD, S. M., et al. The formation of Mn/Si(111) interface at room and high temperatures. Surface Science. 1997, 382, p.258-265

[39] EVANS, M.M.R., et al. Epitaxial growth of manganese on silicon: Volmer-Weber growth on the Si(111) surface. Physical Review B. 1996, 53, p.4000

[40] NAGAO, T., et al. Morphology of ultrathin manganese silicide on Si(111). Surface Science. 1999, 419, p.134

[41] ZOU, Z.-Q., et al. Epitaxial growth of manganese silicide nanowires on Si(111)-(7×7) surfaces. Applied Physics Letters. 2007, 90, 133111: p.1-3

[42] ZOU, Z.-Q. et al. Self-organized growth of higher manganese silicide nanowires on Si(111), (110) and (001) surfaces. Acta Materialia. 2011, 59, p. 7473-7479

[43] Http://www.tedpella.com/ [online]. 2013 [cit.2013-02-05]. Si-STEP Calibration Sample Product No. 629-89. availiable at www: http://www.tedpella.com/technote_html/629-89%20TN.pdf

[44] Http://www.ptable.com [online]. 2012 cit. 2013-03-05. Dynamic periodic table. availiable at: www: http://www.ptable.com

[45] SHAKHASHIRI, B.Z. Chemical of the week: aluminum. Scifun.org [online]. University of Wisconsin. [2008-03-17], available at: http://scifun.chem.wisc.edu/chemweek/PDF/aluminum.pdf [cit. 2013-03-05]

[46] GROGER, R.M., BARCZEWSKI M.R. Ultrathin Al layers on Si(111) and Si(100): structures and phase transitions. Surface and Interface Analysis. 2001, 32, p.154-160

[47] YOSHIMURA, M., et al. Scanning tunneling microscopy observation of Al-induced reconstructions of the Si(111) surface: Growth Dynamics J. Vac. Sci. Technol. B. 1994, 12, p.2434

[48] Uemura, A., et al. Effects of Si reconstruction on growth mode in Al/Si(111) studied by scanning tunneling microscopy. Surface Science. 1996, 357-358, p.825-829

[49] SUMITANI, S., et al. Photoelectron diffraction study of the surfaces of Si(111)-($\sqrt{3} \times \sqrt{3}$)-Al and -In with Mo M-zeta and Cr L-alpha lines. Journal of electron spectroscopy and related phenomena. 1999, 101, p.245-250

[50] TSUGE, H., et al. Atomic structure of Si(111)-($\sqrt{3} \times \sqrt{3})R30^1\circ$-Al studied by 1st principle molecular dynamics. Japanese Journal of Applied Physics part 2-letters. 1991, 30, p.L1583-L1585

[51] LI, ST., et al. Si(111)-($\sqrt{3} \times \sqrt{3}$)-Al surface studied by angle resolved electron energy loss spectroscopy. Japanese Journal of Applied Physics part 2-letters. 1991, 30, p.L1671-1673

[52] HAMERS, RJ. Effects of coverage on the geometry and electronic structure of Al overlayers on Si(111). Physical Review B. 1989, 40, p.1657-1671

[53] UCHIDA, H., et al. Study of adsorption of Al atom on Si(111)-(7×7) surface. Surface Science. 2004, 566-568, p.197-202

[54] ZHENG, W., et al. Scanning Tunneling Microscopy Studies of the in Desorption Process on the In/Si(111) Surface. Journal of the Korean Physical Society. 2008, 52, p. 536540

[55] ICHIKAWA, T., et al. Structural study of ultrathin Sn layers deposited onto Ge(111) and Si(111) surfaces by RHEED. Surface Science. 1984, 140, p.37-63

[56] YOSHIMURA, M., et al. STM observation of Sn overlayers on Si(111). Applied Physics A. 1998, 66, p.S1047-S1049

[57] JEMANDER, S.T., et al. An STM study of the surface defects of the ($\sqrt{3} \times \sqrt{3}$)-Sn/Si(111) surface. Surface Science. 2001, 475, p.181-193

[58] WORTHINGTON, M.S., et al. Surface reconstructions of the Sn/Si(111) system investigated by ion-scattering spectrometry and scanning tunneling microscopy. Nuclear Instruments and Methods in Physics Research. 1992, B64, p.566-571

[59] OTTAVIANO, L., et al. Short-range order in two-dimensional binary alloys. Physical Review B. 2003, 67, p.045401